

TABLE OF CONTENTS

CERTIFICATION	i
DECLARATION	ii
ACKNOWLEDGEMENT	iii
ABSTRACT.....	iv
LIST OF TABLES.....	v
LIST OF FIGURES	vi
LIST OF ABBREVIATIONS.....	viii
GLOSSARY	ix
INTRODUCTION.....	1
1. MOTIVATION AND INTRODUCTION	1
THEORETICAL BACKGROUND.....	6
2. LIB ANODE OPERATION MECHANISM	6
2.1 ELECTRODE DEVELOPMENT	6
2.2 ELECTRODE PROCESSING.....	7
2.2.1 GRAPHITE ANODE SLURRY	7
2.2.2 AQUEOUS GRAPHITE ANODE MATERIALS	8
2.2.3 AQUEOUS GRAPHITE ANODE SLURRY MIXING	11
2.3 COATING PROCESS	22
2.3.1 RHEOLOGY.....	22
2.3.2 COATING.....	27
2.3.3 MULTILAYERING APPROACH	28
2.4 POST-FABRICATION PROCESS	29
2.4.1 ELECTRODE CHARACTERIZATION TESTS	30
EXPERIMENTAL METHODS AND OUTCOMES.....	32
3. OVERVIEW OF MATERIALS AND METHODS	32
3.1 RAW MATERIAL CHARACTERIZATION	32
3.1.1 PARTICLE SIZE EVALUATION	32
3.1.2 BRUNAUER-EMMETT-TELLER (B.E.T) SURFACE EVALUATION	33
3.1.3 RESULTS AND DISCUSSION ON MATERIAL CHARACTERISTICS	34
3.2 SLURRY CHARACTERIZATION	37
3.2.1 SLURRY MIXING	37
3.2.2 PYCNOMETER DENSITY EVALUATION.....	38
3.2.3 RHEOLOGICAL EVALUATION	39
3.2.4 RESULT AND DISCUSSION ON SLURRY CHARACTERISTICS.....	40
3.3 ELECTRODE ANALYSIS.....	52

3.3.1	COATING.....	52
3.3.2	POROSITY AND LOADING CALCULATIONS.....	53
3.3.3	MECHANICAL INTEGRITY	53
3.3.4	RESULT AND DISCUSSION ON ELECTRODE PROPERTIES	54
3.3.5	CALENDARING.....	62
3.4	ELECTROCHEMICAL ANALYSIS	62
3.4.1	CELL ASSEMBLY	62
3.4.2	FULL CELL ELECTROCHEMICAL EVALUATION	63
3.4.3	RESULTS AND DISCUSSION ON ELECTROCHEMICAL PROPERTIES	64
CONCLUSION AND OUTLOOK	78
4.	CONCLUSION.....	78
REFERENCES	80

INTRODUCTION

1. MOTIVATION AND INTRODUCTION

It is nearly impossible to imagine a world where drivers can stop for a short time to charge their vehicle's batteries to full capacity in the same amount of time it takes to fuel a traditional engine. Additionally, it is hard to envision a world where the storage devices for transitioning to renewable energy sources are more efficient, durable, and have a longer lifespan, with high energy densities and power output, while producing zero or low carbon emissions and being produced through sustainable manufacturing processes. Lithium-ion batteries (LIBs) have become an essential part of daily life in consumer electronics, vehicles, and industrial applications, such as grid storage and off-grid power systems, as in Figure 1.1 [1]–[5].



Figure 1.1: LIB Battery Applications areas [6]

Despite the exceptional properties of LIBs, there is a need for these batteries to have shorter charging times, longer ranges (coverable mileage), affordability, recyclability, and sustainability, as well as to meet requirements for specific applications [1], [2], [5], [7]. To address these challenges, researchers in academia and industry have been working to improve the different components of these batteries, leading to various material combinations [8].

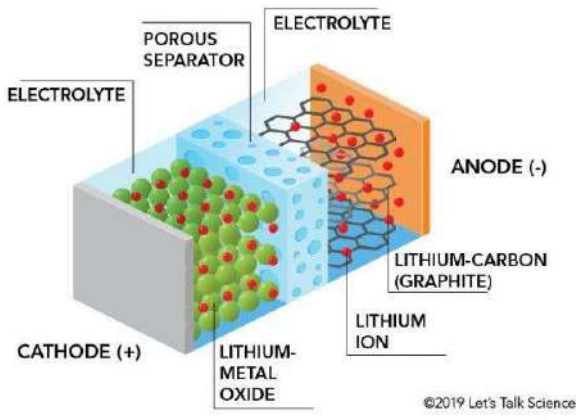


Figure 1.2: Components of a Lithium-ion battery [9]

One of the many aspects researchers focus on is the development of anodes [1], [10]. This research has led to the division between conversion type, alloying type, and other insertion type anodes in addition to graphite [3]–[5], [11].

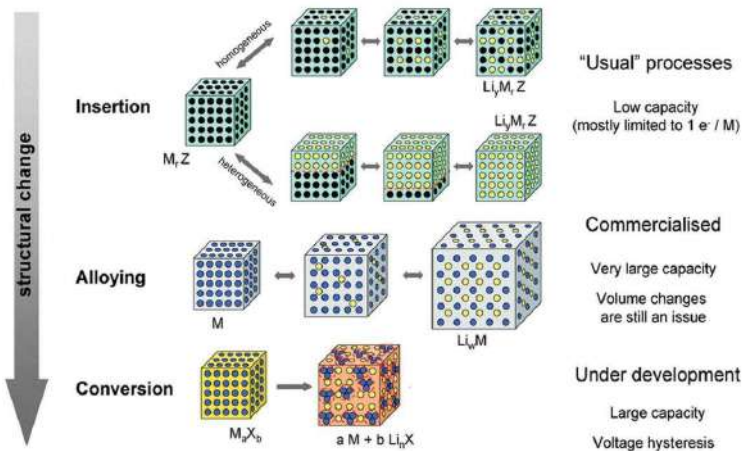


Figure 1.3: Classification of anodes based on reaction mechanisms [4]

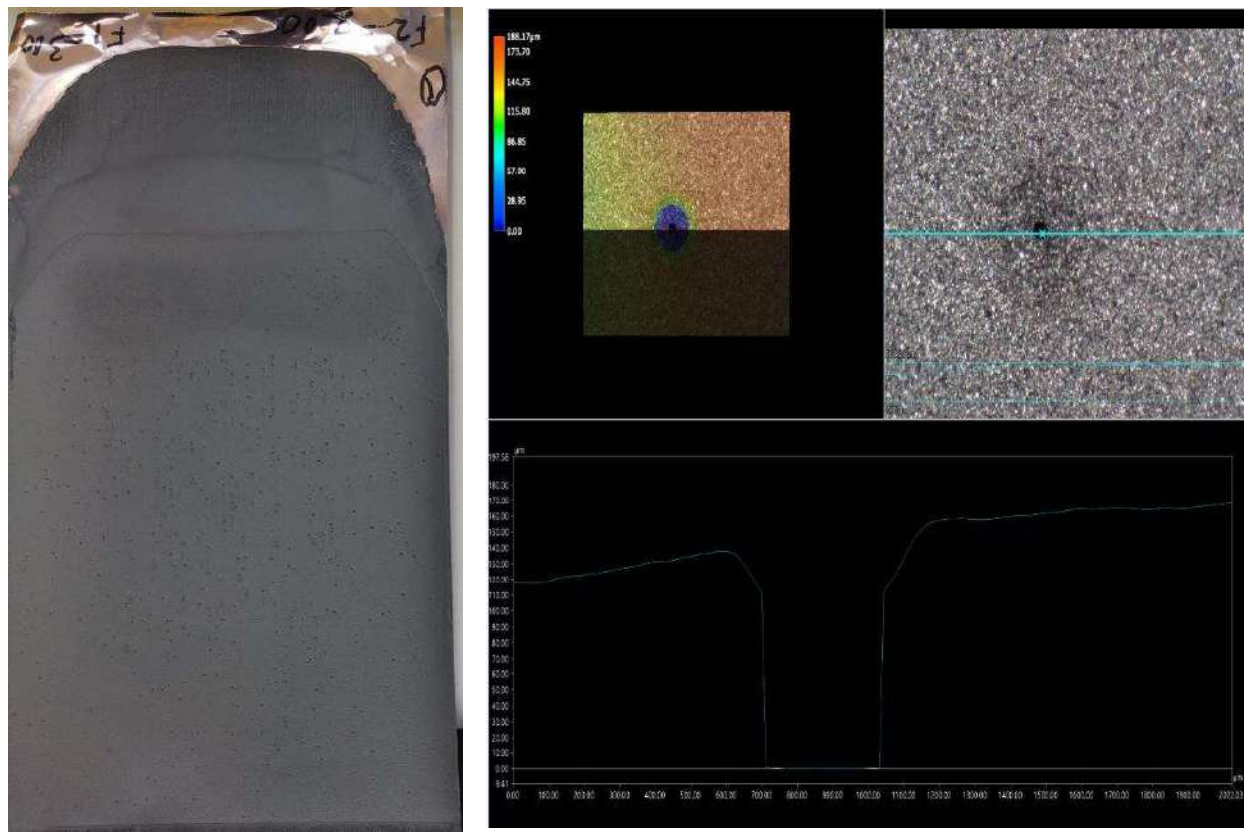
However, the drawbacks of contemporary anode materials have hindered their commercialization or use for specific applications, making graphite the best choice and most commonly used in commercial lithium-ion batteries [5], [12]–[14].

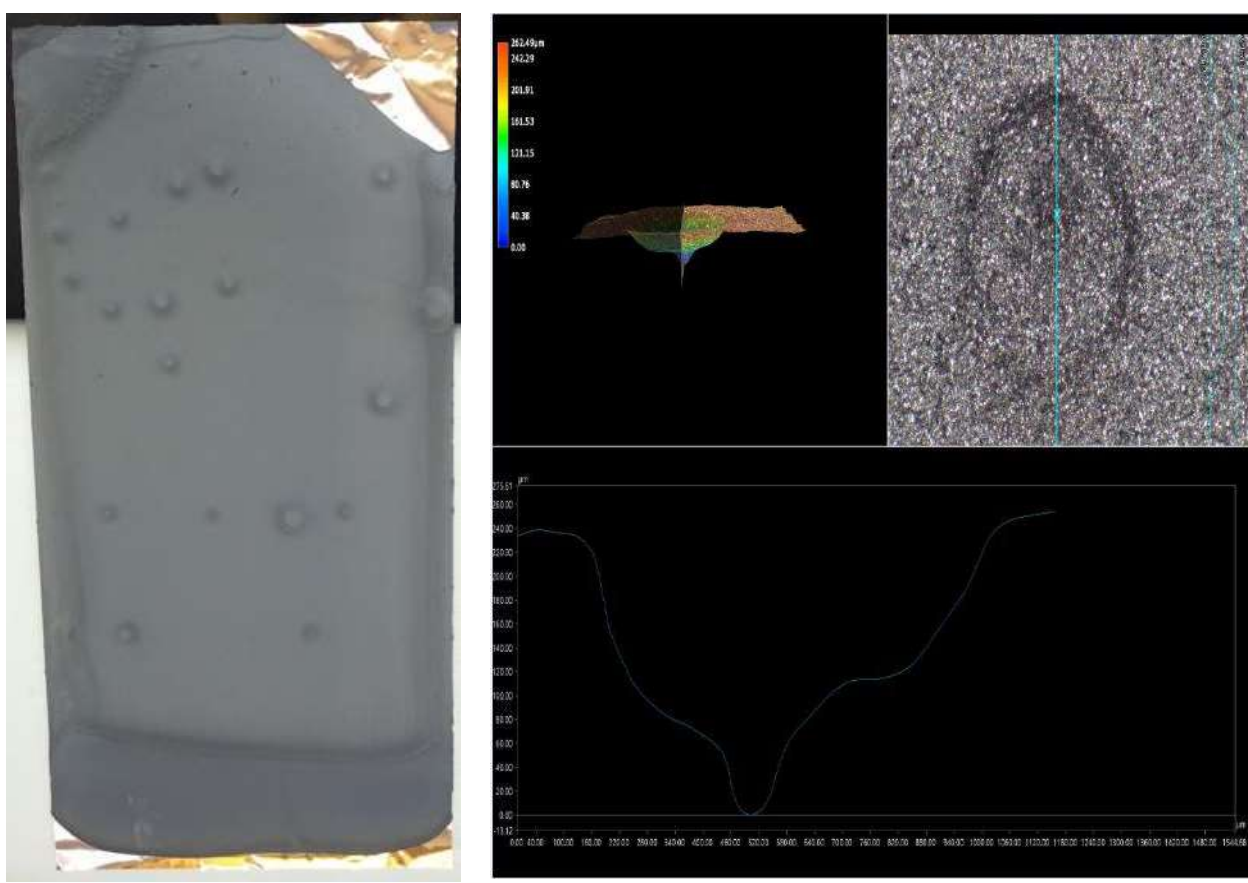
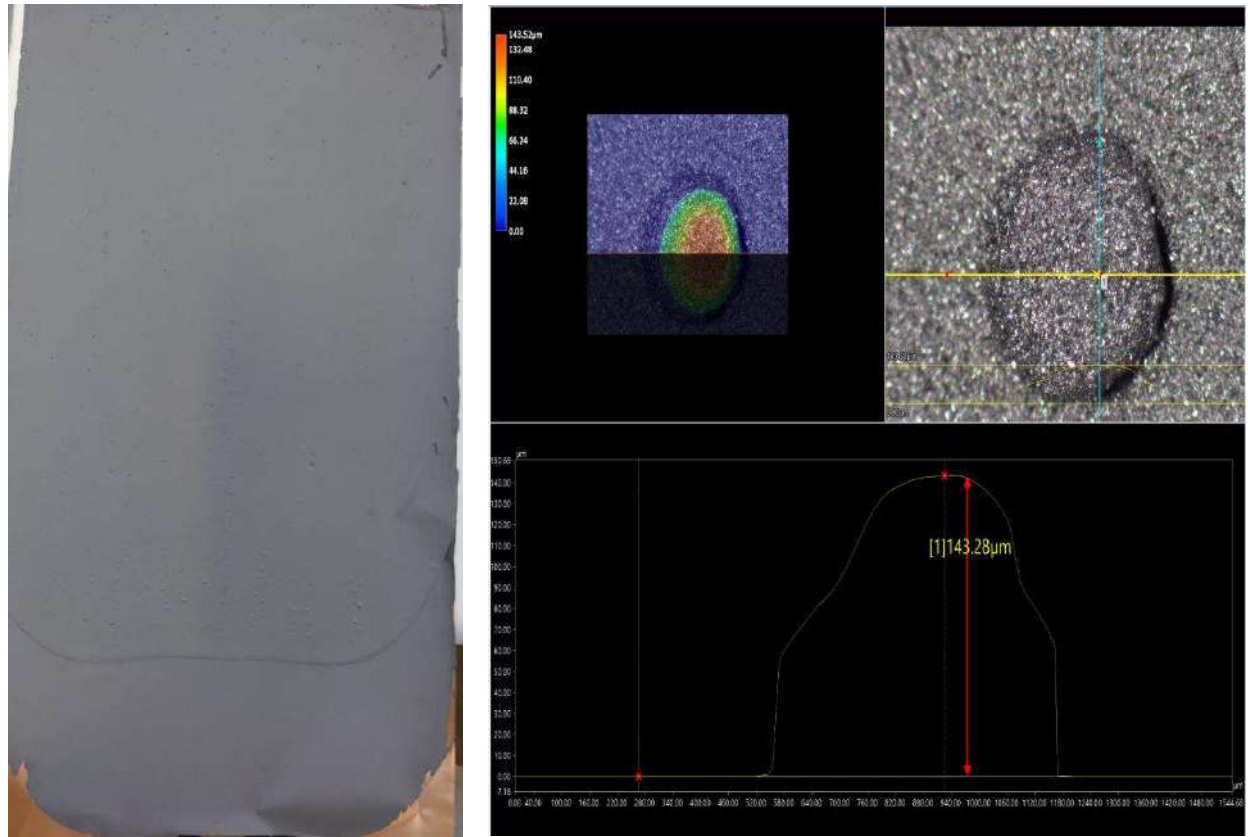
A current research trend aimed at promoting sustainability involves the advancement of graphite-based anodes by replacing the noxious solvent N-methyl-2-pyrrolidone (NMP) with water. Using water as a solvent in the production of lithium-ion batteries is advantageous for low-cost, environment-friendly, fast drying during manufacturing, better homogeneous electrode microstructure and SEI formation; however, it introduces new challenges in the manufacturing process [5], [7], [15], [16]. One of such challenges is the need to adjust the parameters of the electrode production process, such as the drying parameters, to ensure proper evaporation of solvents and smooth diffusion of binders during drying [7],

[17]. Thus, electrode production parameters must be considered to create defect-free and mechanically stable aqueous anodes and optimize the electrochemical performance of lithium-ion batteries [3], [7]. In addition, designing high-density cells and developing thick electrodes to replace traditional thin anodes adds complexity to using water and CMC binders, resulting in more defects and delamination [5], [7].

The primary issue of concern in the electric vehicle industry is the limited distance coverage of the average electric vehicle (EV). Currently, electric vehicles can only cover a few hundred kilometres, and to increase the mileage coverage while maintaining low manufacturing costs and overall product costs, the energy density must be increased. This means reducing the volume while increasing the energy [7], [18]. During the production of high-energy-density cathodes, the requirement for a corresponding anode to meet the high-energy density requirements, cost-effectiveness, and sustainability emerged.

Nonetheless, creating super-thick anodes with high energy density has been challenging due to poor dispersion of the constituents within the anodes and problems of binder insulation [7]. In order to tackle the difficulties mentioned above and account for the earlier-mentioned complexities, this thesis endeavors to investigate graphite as an anode material for lithium-ion batteries due to its exceptional properties. As previously noted, the illustration presented in Figure 1.4 highlights some of the challenges encountered stemming from the intricate interplay of water and increased electrode thickness that must be overcome to produce flawless anodes.





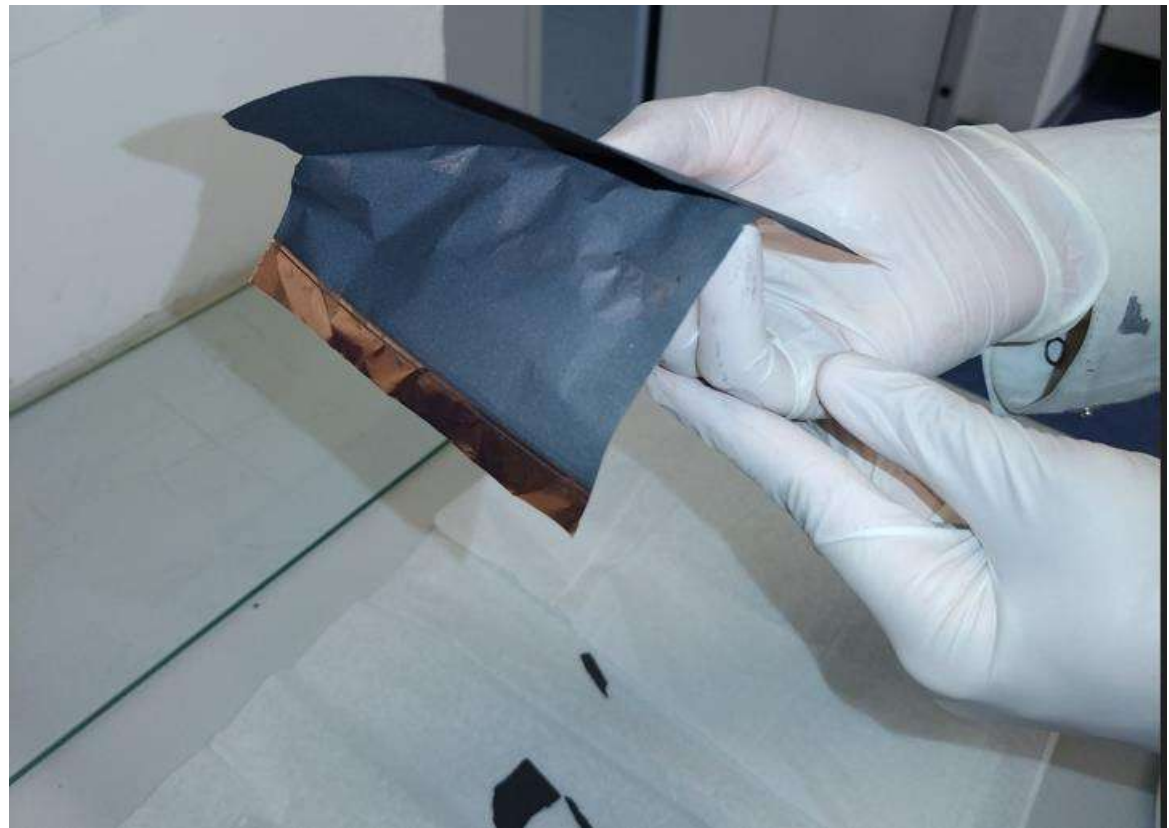


Figure 1.4: Defects occurring during an aqueous process of thick graphite anodes a) Pinholes b) Agglomerates c) Crates d) Delamination of coating.

The idea is to use a multilayer approach (which provides the avenue to stack or alternate layers of different materials to create an electrode with properties determined by the individual layers and interfaces [7], [19]) to create thick anodes while optimizing the process steps and their respective parameters to achieve high energy density and performance.

THEORETICAL BACKGROUND

2. LIB ANODE OPERATION MECHANISM

In lithium-ion batteries, the electrodes are responsible for storing and releasing lithium ions during charging and discharging [5]. This process is known as intercalation and deintercalation. During intercalation, lithium ions are inserted between the layers of graphite crystals in the anode (host). This increases the distance between the layers and expands the anode [5], [14]. The reverse process, deintercalation, occurs during battery discharge when lithium ions are extracted from the graphite layers with a corresponding decrease in distance between the layers, causing the anode to contract [8], [13], [20]. Therefore, the graphite anode must possess several vital properties to function well during intercalation and deintercalation. It must have a high reversible capacity, meaning it can store and release large amounts of lithium ions without degrading over time. It must also have good electrical conductivity to facilitate the flow of charge within the battery. In addition, the graphite anode should have good structural stability to withstand the expansion and contraction that occurs during intercalation and deintercalation [4], [8]. To this end, optimizing the anode (through improved fabrication) is crucial for improving the overall performance of lithium-ion batteries, as the efficiency of the electrochemical reactions at both electrodes significantly impacts the battery's performance [4], [8], [10], [13].

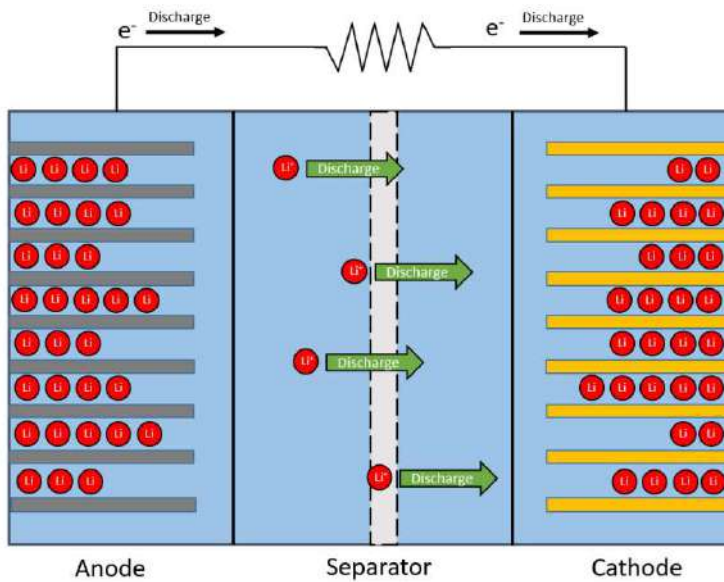


Figure 2.1: Schematic of the lithium-ion battery at discharge [21].

2.1 ELECTRODE DEVELOPMENT

An electrode is a conductive material that establishes an electrical connection with a non-metallic component in a circuit. Anodes and cathodes are the two types of electrodes. The anode is typically the electrode where oxidation occurs, and the cathode is where reduction occurs during discharging [20]. However, oxidation and reduction can occur at either electrode in battery technology, depending on whether the battery is being charged or discharged. Therefore, in battery technology, the anode is

defined as the electrode with a high concentration of Li^+ ions after charging, and the cathode is the electrode with a low concentration of these ions after charging. The opposite is true during discharge [13], [20]. The performance of graphite anodes is significantly influenced by the preparation of the electrode, as it affects the graphite network's porosity, tortuosity, and overall electronic conductivity [7]. It is, therefore, essential to evaluate the fabrication steps and consider the factors that impact the mechanical and electrical performance of the cell during each process step [22].

2.2 ELECTRODE PROCESSING

The manufacturing process of electrodes involves several steps such as mixing and coating a slurry, consequently drying and calendering the produced electrode layer. To create an electrode ink (or slurry) for a lithium-ion battery, active material, polymer binder, and conductive carbon are mixed in a solvent. The resulting mixture is then coated onto a thin aluminium or copper foil, depending on whether it will be used as the cathode or anode, and the solvent is evaporated through controlled drying. The coating is rolled to the desired thickness and cut or slit to the size needed for cell assembly [5], [15], [23], [24].

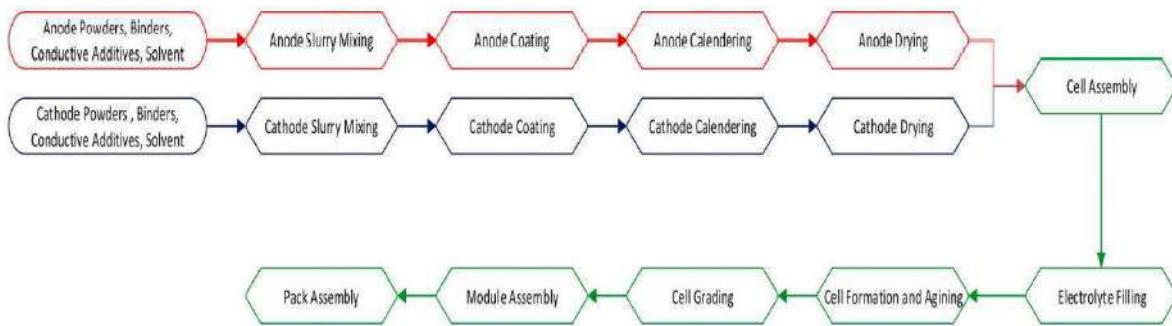


Figure 2.2: Electrode processing steps [5]

The final properties of the electrodes depend on a range of factors, including the characteristics and ratios of the raw materials, the mixing and coating techniques used, and the process parameters, such as the temperature and duration of the drying process or the applied compacting rate. Optimizing these parameters can improve the electrodes' microstructure and the battery's overall performance [23]. Thus, factors to consider when optimizing an electrode or cell include the materials, their proportions, the processing parameters, and the mixing process [5], [22], [25], [26].

2.2.1 GRAPHITE ANODE SLURRY

A slurry is a viscous paste that contains all the raw materials for the active mass. During processing, it loses its viscous nature to form a rigid structure with inherent mechanical and electrical (functional) properties for the electrode. The slurry used to make electrodes for lithium-ion batteries is made by mixing dry powdered components (electrochemically active and inactive) and a solvent to form a liquid slurry with evenly distributed particles [25], [26]. This slurry is then coated onto metallic foil current collectors and smoothed to create uniform electrode films. The films are then heated to remove the solvent and compressed by metal rollers to a desired thickness and porosity. Table 2.1 presents the

classification of graphite anode slurries based on solvent: the conventional non-aqueous slurry and the emerging aqueous slurry types for graphite-based anodes [5].

Table 2.1: Graphite anode materials [5], [23]

Anode type	Non-aqueous	Aqueous	Functions
<i>solvent</i>	NMP	Deionized water	Dissolves the solutes
<i>Active material</i>	Graphite	Graphite	Store and release li-ions
<i>Conductive agent</i>	Carbon black	Carbon black	electron transport
<i>Binder</i>	PVDF	CMC + SBR	Dispersant/adhesion to the current collector

While there are various binder systems for aqueous anodes in lithium-ion batteries, the combination of Carboxymethyl cellulose (CMC) and Styrene-butadiene rubber (SBR) is one of the most commonly used [23], [27]. The dispersion and flow properties of slurries are essential factors that can affect the quality and performance of the resulting products [25], [28].

2.2.2 AQUEOUS GRAPHITE ANODE MATERIALS

The materials are electrochemically active materials that participate in the chemical reaction, the conductive agent that transport the electrons generated during the chemical reaction, binders that thicken the raw material slurry and bond the raw material particles to the substrate material, and solvent acting as the dispersion medium [5], [23].

As the active material, graphene comprises of flat planes of hexagonal rings of carbon atoms to make a honeycomb-shaped lattice [8]. The carbon atoms in graphene are bonded through a combination of s and p bonds, that is, strong covalent bonds and weak Van der Waals (VDW) connections or π - π interactions of the delocalized electron orbitals when stacked. Moreover, graphite is composed of stacked graphene sheets, and it is a soft, greyish-black substance with a hexagonal lattice structure, thus a crystalline form of carbon [29], [30]. Graphite has high structural rigidity, with specific strengths of up to 130 GPa, making it suitable for use as an electrode material. It has a high melting point of around 3600 °C (6500 °F) and is highly chemically stable, not reacting with most acids or bases. Graphite has good electrical conductivity and is a good conductor of heat, but its conductivity is anisotropic, meaning it depends on the current's direction [29], [31].

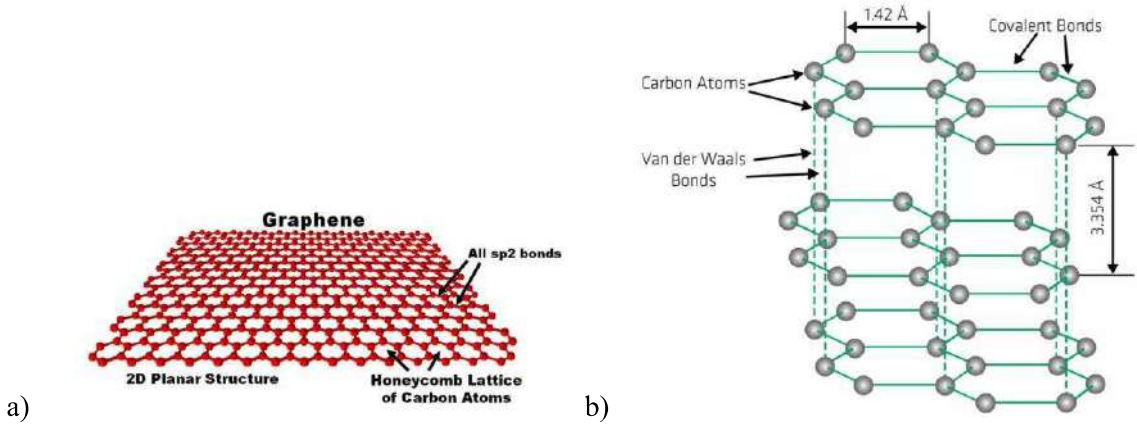


Figure 2.3: a) Honeycomb structure of monolayer graphene [32], b) Hexagonal structure of graphite [33]

Carbon black is a type of porous carbon with a high surface area-to-volume ratio and a crystalline structure of randomly arranged carbon atoms forming spherical particles [29]. These particles can easily move and compress relative to each other, making carbon black highly compressible and able to spread out when subjected to a compressive force [34]. This property allows carbon black to be an effective additive for increasing the electrical conductivity of a nonconductive compact, even in the absence of a matrix, and specifically, the purpose for its use in electrode manufacturing [34], [35]. Carbon black is used in various applications, including as a reinforcement in rubber, a pigment in the printing ink, sealants, coatings, and plastics, and as a catalyst that influences the structure of slurry in electrodes [34], [36].

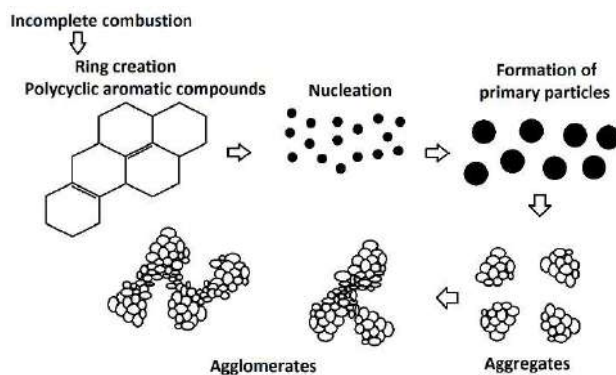


Figure 2.4: CB particles and agglomerates [37].

Sodium carboxymethyl cellulose, or CMC, is a white, tasteless, and odorless powder made from cellulose with partially-substituted hydroxyl groups. CMC separates into a sodium cation and a polymer anion that interact through electrostatic forces in water. CMC forms a clear, viscous solution with high water-holding capacity, good film-forming properties, and stability [25]. It is used as a thickening agent, binder, and stabilizer in various industries [28]. CMC's material and electronic properties are largely determined by the degree of substitution of the cellulose molecule with sodium carboxymethyl groups,

which can be varied to tailor the properties of CMC for specific applications. CMC has a high dielectric constant, dielectric loss factor, and resistivity [25], [38].

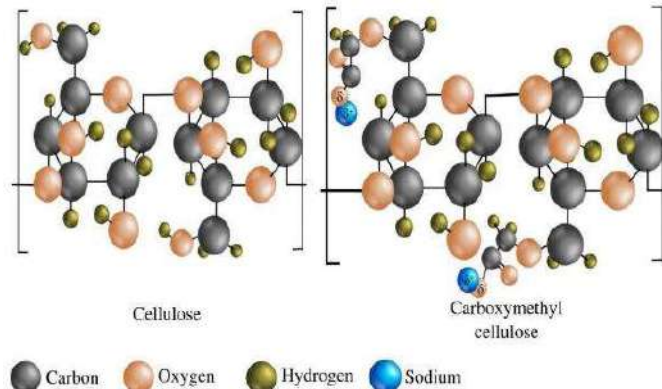


Figure 2.5: Structure of cellulose and sodium-carboxymethyl cellulose [39].

Styrene-butadiene rubber (SBR) is a type of polymer (random copolymer) that is elastic and has a low hardness level. It is made up of repeating units of two types of monomers, styrene and butadiene, which contribute different electronic properties to the polymer. The physical and electronic properties of SBR can be influenced by the ratio of styrene to butadiene and the degree of crosslinking in the polymer. SBR has good tensile strength and is resistant to wear and tear, UV radiation, extreme temperature changes, and humidity. It also has a low coefficient of friction and can be used as a lubricant. However, it is a poor conductor of electricity, has a low dielectric constant, can dissipate electrical energy as heat, and has high resistivity [38].

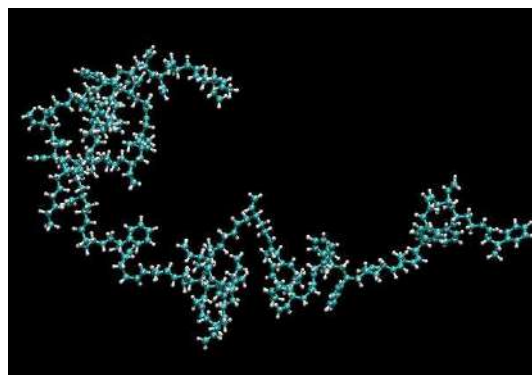


Figure 2.6: Structure of styrene-butadiene rubber (SBR) [40].

Solvents are commonly used to dissolve, disperse, or extract other substances [28]. Deionized water (DI water) is a type of purified water with its ions (e.g. Sodium and potassium) removed through ion exchange. Water molecules have a positive charge at one end and a negative charge at the other, giving them a polarity. This polarity allows water molecules to form hydrogen bonds with one another, giving water many unique properties, such as its high surface tension and ability to dissolve many substances. The ability of water to dissolve a wide range of substances due to its polarity makes it a proper solvent in many industrial processes. Additionally, its low boiling point of 100 °C compared to NMP (202 °C)

makes it more energy-efficient in drying [23]. This and its environmental-friendly properties, make water a popular choice in green lithium-ion battery manufacturing [7]. It has a neutral pH and does not react with most acids or bases. It has a high dielectric constant, storing and transmitting electrical charge [41]. During the early stages of lithium-ion battery manufacturing, NMP was commonly utilized as a solvent because of its distinctive physicochemical properties, which make it an excellent choice for dissolving non-aqueous binder polyvinylidene fluoride (PVDF).

2.2.3 AQUEOUS GRAPHITE ANODE SLURRY MIXING

While graphite, carbon black, and CMC are powders or flakes, SBR latex is usually a suspension. The anode slurry is, therefore, a two-phase system made up of solids (solute particles) and liquid (solvent) [42]. The properties of both the solids and the liquid can impact the slurry's quality and the resulting electrode's performance [23]. Factors such as the ratio of raw materials, mixing procedure and sequence, viscosity, and sedimentation stability can significantly affect the coating process [15], [22], [23].

2.2.3.1 CONSIDERATIONS FOR SLURRY MIXING

2.2.3.1.1 MATERIAL CHARACTERISTICS

As previously mentioned, the anode slurry in lithium-ion batteries is made up of a mixture of solid materials, such as active materials, conductive agents, binders, and a liquid solvent. The solid materials have at least one dimension within the nanometer to micrometer range, which makes the resulting slurry a colloidal system [30], [43]. Colloidal systems are made up of insoluble particles suspended or dispersed in a liquid medium and are classified into three types: colloidal dispersions, true solutions, and associated colloids. The slurry's properties depend on the roles of the constituent phases. The factors which contribute most to the general nature of a colloidal system are the particle size, particle shape and particle flexibility, particle-particle interaction, particle-solvent interaction, and surface and electrical properties [27], [44], [45].

For instance, polymers can be used as dispersants or thickeners in some cases, and they have unique shapes compared to typical solutes. Depending on the polymerization reaction, polymer binders have different molecular chain lengths and, as a result, different inherent properties. Polymer molecules have much flexibility due to their bond's ability to rotate. However, there are also limitations to this flexibility due to steric and excluded volume effects and dissolved linear polymers being more extended than random coils [42], [45]. If the polymer chain segments tend to attract each other, it can lead to a tighter configuration or precipitation. If they tend to repel each other due to strong solvation or electrical forces, the resulting configuration will be non-compact, as in a dispersion. Therefore, the strength of the interaction between polymer molecules and the polymer solvent is a factor for consideration.

Further, the powders have specific characteristics such as size, shape and surface area differences, all of which influences the properties of the colloidal system [27], [46]. For instance, larger particles tend to have higher inertia due to their greater mass, making them more difficult to accelerate or decelerate.

Elongated particles may also have a different response to external forces compared to spherical particles of the same size, and particles with an irregular shape may have more corners and edges, increasing their surface area and impacting their interactions with other particles due to the increased number of atoms or molecules on its surface that are available for chemical reactions. Some of the properties of a dispersion that these material features can influence include [18], [42], [44], [46], [47]:

- i. **Diffusion:** Smaller particles have a lower mass and are more easily moved by thermal motion and therefore tend to diffuse more quickly through a medium than larger particles. As a result, smaller particles tend to mix more easily with the medium than larger particles. Similarly, irregularly shaped particles may diffuse more quickly than spherical particles because the irregular shape provides more points of contact with the medium, allowing the particles to move more easily.
- ii. **Surface tension:** The presence of small particles in a medium can also affect the surface tension of the medium. This is because the small particles can interact with the surface of the medium, disrupting the cohesive forces that give rise to surface tension, resulting in lower surface tension. As a result, colloidal dispersions with small particles tend to have a lower surface tension than dispersions with larger particles. Similarly, irregularly shaped particles may disrupt the cohesive forces more than spherical particles because the irregular shape provides more points of contact with the surface of the medium.
- iii. **Viscosity:** The presence of small particles in a medium can increase the viscosity of the medium. This is because the small particles can interact with each other and the medium, increasing the resistance to flow. As a result, colloidal dispersions with small particles tend to have a higher viscosity than dispersions with larger particles. Similarly, irregularly shaped particles may increase the viscosity of a colloidal dispersion more than spherical particles because the irregular shape provides more points of contact with the medium. The surface area of the particles can also influence the viscosity of a colloidal dispersion, with particles with a larger surface area tending to increase the viscosity more than particles with a smaller surface area because there is more surface for the particles to interact with.
- iv. **Sedimentation:** Larger particles tend to sediment quicker than smaller particles because larger particles have a greater mass and are more affected by gravity. On the contrary, smaller particles tend to remain suspended in the medium. The shape of the particles can also influence sedimentation, with irregularly shaped particles generally sedimenting more slowly than spherical particles because the irregular shape provides more points of contact with the medium, which can slow the sedimentation process. The surface area of the particles can also influence sedimentation, with particles with a larger surface area tending to sediment more slowly than particles with a smaller surface area because the larger surface area provides more points of contact with the medium.
- v. **Stability:** Smaller particles are generally more stable in a colloidal dispersion than larger particles. This is because smaller particles have a larger surface area relative to their volume, which makes it

easier for stabilizing forces (examples are: charge, physical forces, and steric forces) to act on the particles and prevent them from aggregating or settling out of the medium. The shape of the particles can also influence their stability, with irregularly shaped particles generally being more stable than spherical particles because the irregular shape provides more points of contact for stabilizing forces to act on.

Additionally, due to the polydisperse nature of dispersions, it can be challenging to determine the size distribution of colloidal particles accurately. In this regard, two methods commonly used for determining average values of relevant characteristics in this study are direct observation of particles using microscopy and gas adsorption or adsorption from solutions [48]. Meanwhile, gas adsorption or adsorption from solutions is a technique used to measure the total surface area of particles, such as colloidal particles or nanoparticles. This technique is based on the principle that gases or solutions can be adsorbed onto the surface of a solid, and the amount of adsorbate that can be taken up is proportional to the surface area of the solid. One of the several techniques that can be used to measure gas adsorption is the Brunauer-Emmett-Teller (BET) method [46].

The BET method is commonly used for measuring the surface area of porous materials such as colloids and nanoparticles. It is based on the principle that gases can be adsorbed onto the surface of a solid, and the amount of gas adsorbed is proportional to the surface area of the solid. In the BET method, a gas, such as nitrogen, is adsorbed onto the material's surface at a series of pressure levels, as in Figure 2.7 [46].

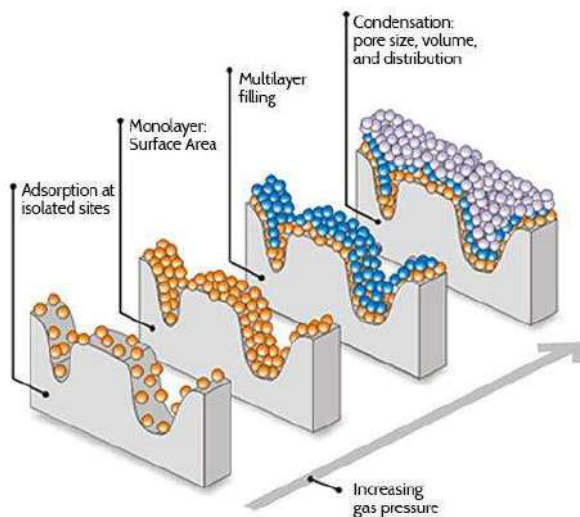


Figure 2.7: BET gas adsorption levels [49]

The amount of gas adsorbed is measured, and the surface area is calculated from the adsorption data using a specific mathematical model known as the BET equation (equation I),

$$\frac{1}{w\left[\left(\frac{P_0}{P}\right)-1\right]} = \frac{1}{w_m C} + \frac{C-1}{w_m C} \left(\frac{P}{P_0}\right) \quad (\text{Eqn. 2.1})$$

where $\frac{P}{P_0}$ is the relative pressure, w_m is the number of adsorbed gas on a solid surface, W is the number of gas molecules adsorbed at a given relative pressure, C is a second parameter related to the heat of adsorption [50]. The BET equation considers the interaction between the gas molecules and the material's surface, and it can be used to accurately predict the amount of gas adsorbed at different pressure levels. The chemist Paul Brunauer has also classified adsorption isotherms (graphs of the amount of gas adsorbed versus pressure) into several types based on the shape of the isotherm, as shown in Figure 2.8. These types include Type I (linear), Type II (concave up), Type III (concave down), and Type IV (non-monotonic). Each type of isotherm is associated with a specific type of material and adsorption mechanism and can provide insights into the structure and properties of the material. The BET method has been widely adopted in the field of materials science and engineering. It has been used to study a wide range of materials, including metal oxides, zeolites, and carbon-based materials [50], [51].

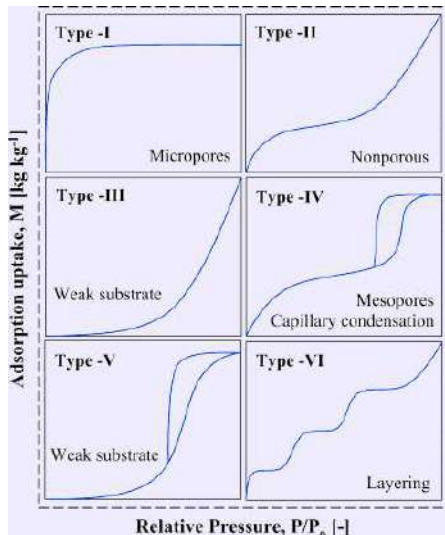


Figure 2.8: BET adsorption isotherms [46].

2.2.3.1.2 MATERIAL RATIO

The ratio of the materials in the electrode slurry is crucial because it affects the properties of the resulting electrode [22], [25], [52]. For instance, the ratio of active material to the binder, for example, will affect the electrode's electrical conductivity and mechanical stability. The ratio of conductive agent to binder will affect the ability of the electrode to transport electrons. The ratio of solvents to solids will affect the viscosity and flow properties of the slurry, which can impact the coating process. In general, it is essential to carefully formulate the ratio of materials in the electrode slurry to ensure that the resulting electrode has the desired properties for its intended application [5]. In the manufacture of electrodes for lithium-ion batteries, the ratio of the electrochemically inactive materials is reduced to the barest minimum to accommodate more electrochemically active constituents and thereby improve cell performance [5], [24], [28].

2.2.3.1.3 MIXING SEQUENCE

The mixing procedure and sequence of the materials in an electrode slurry are vital because they can affect the dispersion and distribution of the particles in the slurry. The mixing procedure can also affect the viscosity of the slurry, which can impact its coating properties and the ability of the slurry to flow and spread evenly on the current collector [5], [15], [22], [23], [26]. If the materials are not properly mixed or are added in the wrong sequence, it can result in inhomogeneities in the slurry and uneven distribution of the particles within the coating, which can lead to poor performance of the resulting electrode. Therefore, it is essential to carefully control the mixing procedure and sequence of the materials in order to ensure that the slurry has the optimized structure and properties necessary to produce high-quality electrodes [22], [23], [26].

2.2.3.2 MIXING TECHNIQUES

Various slurry mixing equipment has been utilized in battery manufacturing, depending on the mixing mechanism, which helps disperse and distribute electrode materials effectively [23]. In this study, the mixing equipment used employs mechanical stirring and planetary centrifugal stirring (discussed in Chapter 3). The two stirring mechanisms are discussed briefly.

- i. The mechanical stirring technique involves mixing the slurry components with a mechanical stirrer or agitator. This can be done using a simple hand-held stirrer or a more complex machine with adjustable speed and torque settings. Among other commercially available equipment based on this stirring mechanism are the Planetary and Dispermat mixers (in Figure 2.9) [53]. The Planetary mixer, with a name inspired by the similarity of the components similar to the motion of the planets around the sun, uses a rotating central axis (rotating around a fixed point) and one or more outer arms (rotating around each of their axes and together around the central axis) to agitate and mix materials. The stirring mechanism of a planetary mixer can be either a kneading process, in which the materials are pushed and pulled by the rotating arms or a shearing process, in which the materials are cut and mixed by the arms. It is typically used for mixing dough, pastes, and other materials that are difficult to stir [15], [22].

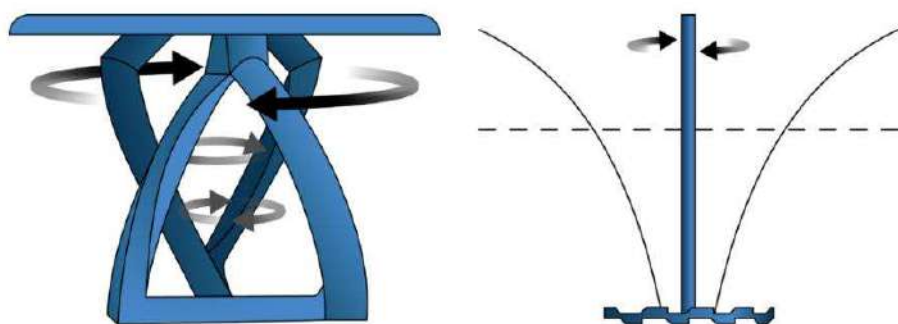


Figure 2.9: Schematic of Planetary mixer and Dispermat mixer propellers [53]

Furthermore, the Dispermat mixer consists of a stationary mixing vessel and a rotating impeller that is mounted on a shaft (rotor-stator system). The impeller is designed to create a shearing action on the material being mixed, breaking up agglomerates and dispersing the material evenly. The high-speed rotation of the rotor creates a strong shearing action that effectively disperses and mixes materials. Despite its ability to mix and disperse materials (even highly viscous materials) quickly and efficiently, it can be considered unsuitable for mixing materials sensitive to shear forces or prone to degradation during the mixing process.

- ii. Planetary centrifugal stirring, as the name implies, is based on using centrifugal force. A typical piece of equipment based on this mixing mechanism is the Thinky Mixer. This mixer uses a rotating inner cup suspended in a stationary outer cup. As the inner cup rotates, the material being mixed is subjected to both centrifugal and gravitational forces. Combining these forces results in a highly efficient and thorough mixing action capable of producing homogeneous mixtures with a short mixing time. The Thinky Mixer is advantageous in handling various mixing tasks, including dispersing, emulsifying, homogenizing, and deaerating.

These are among the recognized methods that can produce homogeneously dispersed slurries. Other mixing methods that could be used include extruder, ultrasonic mixing, which creates agitation through high-frequency sound waves, and high-energy ball milling, which blends the slurry components using a ball mill machine.

2.2.3.3 ANODE SLURRY AND INTERACTION FORCES

The slurry can be defined as a colloidal system since it contains graphite and carbon-black particles in the micrometre and nanometre range, respectively [36]. It is a dispersion containing materials of varying sizes and shapes and rigidity or flexibility when other constituents are added [51]. The ratio of mixing constituents dictates the quantity of polymer binders (highly electrically resistive) to the graphite and carbon black (electrochemically conductive) based on the end performance requirements. Further, colloidal dispersions particles have the tendency to aggregate or be uniformly dispersed, and so the stability of dispersions is determined by the interaction between the particles during frequent encounters. Since a well-dispersed medium is a desire in most cases, mixing sequence is crucial to achieving a well-dispersed slurry, resulting in efficient electrodes [26], [51].

2.2.3.3.1 DISPERSION FORCES

Colloidal interactions in the graphite anode slurry can be divided into two types, DVLO (Van der Waals and Electrostatic double layer) and non-DVLO interactions (steric, hydrophobic, depletion, polymer bridging, hydration), as illustrated in Figure 2.10 [43], [46], [54], [55]. The DLVO theory, which stands for Derjaguin, Landau, Verwey, and Overbeek, is a theoretical framework that describes the stability of suspensions and emulsions in terms of two main interactions: the Van der Waals forces, and the electrostatic double-layer repulsion. For brevity, the Van der Waals forces are the attractive forces

between particles caused by the fluctuation of electron density in the particles, while the electrostatic double-layer repulsion is the repulsion between particles caused by the Coulombic interaction of the charges on the surfaces of the particles and the charges in the surrounding medium. According to the DLVO theory, these two interactions determine the stability of suspensions and emulsions by balancing the attractive and repulsive forces between particles [42].

Electrostatic interactions occur when aqueous solutions are used as the medium of dispersion and are present in the surface interactions. [51], [54]. It is the force of attraction or repulsion between charged particles. When in conjunction with Van der Waals (VDW) forces, an electric double layer (EDL) is formed when the charged particle surfaces are in contact with water. The EDL is composed of two layers: the surface layer, or Helmholtz layer, which is composed of counterions that are attracted to the electrode, and the diffuse layer, which is composed of ions that are farther away from the electrode. The distance between these layers is called the Debye length. When the molecules of the charged particles and water have the same charges, the EDL surface is repulsive, preventing the aggregation and precipitation of the particles [42].

The VDW interactions originate from electrical forces, which can be attractive or repulsive, between atoms or molecules. This means that when two atoms or molecules are close, their electron clouds overlap and interact. The resulting attractive or repulsive forces depend on the electron density distribution of the two atoms or molecules. For example, if the electron density is higher around one atom or molecule than the other, there will be an attractive force between them. On the other hand, if the electron density is higher around both atoms or molecules, there will be a repulsive force between them. The fact that they are not due to covalent bonds or ionic charges makes it a weaker form of bonding. VDW forces are long-range forces caused by the fluctuating electric dipoles that arise due to the movement of electrons in atoms and molecules. These attractive forces can be divided into three categories: dipole-dipole forces, where two molecules with permanent dipoles orient themselves in a way that creates attraction; dispersion forces, where dipolar molecules induce dipoles in other molecules, leading to attraction; and hydrogen bonding in which attractive forces also exist between non-polar molecules, as shown by the liquefaction of certain gases. The Van der Waals interaction's strength depends on the interatomic separation, or the distance between the two atoms or molecules [51], [54].

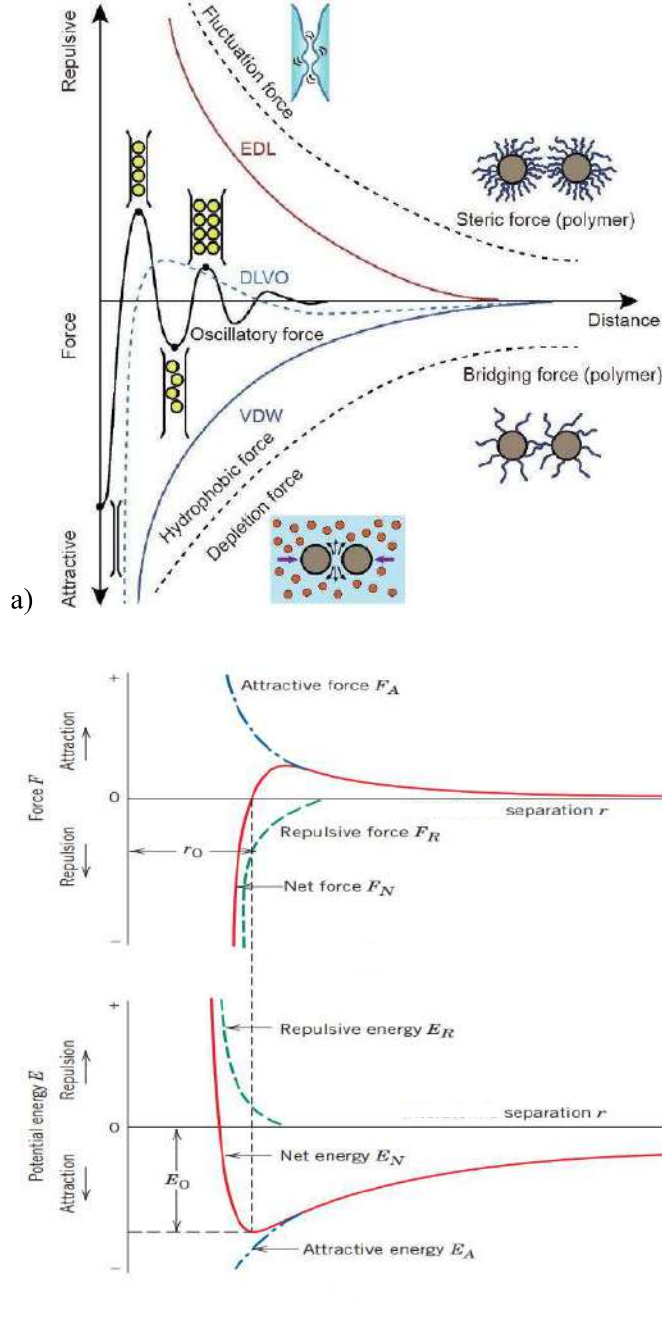


Figure 2.10: a) Colloidal forces [54], b) Force-distance and potential energy-distance profiles [56]

As the particle distance or separation decreases, the Van der Waals interaction becomes stronger. This results in an increase in the potential energy between the atoms or molecules. As the interatomic separation increases, the Van der Waals interaction becomes weaker, and the potential energy decreases. At short interatomic separations (r), the Van der Waals interactions are repulsive. This is known as the Van der Waals repulsion. As the interatomic separation increases, the Van der Waals interaction becomes attractive, and the potential energy decreases. This attractive force is known as the Van der Waals attraction. It arises from the induced dipoles formed in the two atoms due to the fluctuations in their electron distributions [51], [56].

On the other hand, non-DVLO interactions refer to other types of interactions that occur in suspensions, such as steric, hydrophobic, depletion, polymer bridging, and hydration interactions. For brevity, depletion interactions occur due to the presence of a third component in the suspension that causes a reduction of the attractive forces between particles. Polymer bridging interactions occur due to the presence of polymer molecules between particles, and hydration interactions occur due to the presence of water molecules surrounding the particles. Steric interactions occur due to polymer molecules surrounding the particles, and hydrophobic interactions occur due to the repulsion between particles and water. Steric effects occur when polymers are present at a solid-liquid interface (CMC is at the interface of graphite and water), and there is an entropic force due to the compression of the polymer chains when two solvated surfaces approach each other [28]. Steric repulsion occurs when the size or shape of two molecules or molecular fragments is such that they cannot come close to each other without experiencing a significant increase in energy. Steric attraction, on the other hand, occurs when the size or shape of two molecules or molecular fragments is such that they can come close to each other without experiencing a significant increase in energy [42].

Since the colloidal forces (VDW) are long-range forces and their strength determines the extent of aggregation or good dispersion, equally long-range forces are required to counteract the colloidal forces and promote stability [42], [51]. Solvation is a process in which a substance dissolves in a solvent and it is referred to as hydration if the solvent is water. Although solvation is short-ranged (that is has a limited range of influence), the way the molecules are organized during solvation can affect the stability of the substance for a longer distance. The solvent and solute are reorganized into solvation complexes during the solvation process. The particular force involved depends on the molecular structure and properties of the solvent and solute. Solvation can be used to stabilize a substance in two ways [36], [51]:

- i. Through the overlap of electric charges (i.e. overlap of similarly charged double layers)
- ii. Through the use of polymers or surfactants

2.2.3.3.2 DISPERSED AQUEOUS GRAPHITE ANODE DISPERSION

In the aqueous anode dispersion, the particles are surrounded by a thin layer of solvent molecules and are in contact with each other via attractive forces such as Van der Waals forces and electrostatic forces. These forces are responsible for holding the particles together in the dispersion, and the balance between these forces determines the stability of the dispersion [15], [28], [43], [51]. Typically, the hydrophobic nature of graphite particles leads to their aggregation and formation of a gel-like structure in an aqueous slurry [28]. While both CMC and SBR binders can disperse the graphite particles by adsorbing onto their surface, a well-dispersed slurry is more effectively obtained when CMC is added before SBR [25], [26]. If a low dosage of SBR is added to graphite first, SBR will be adsorbed onto the graphite surface, causing coagulation, and resulting in the formation of aggregates. This is because the graphite particles

are crosslinked together through adsorption, making it difficult to achieve uniform dispersion. However, as the concentration of SBR increases or is at high dosages of SBR, the SBR reduces the attractive force between the graphite particles. The graphite particles will be coated with an appropriate amount SBR, creating a repulsive force and dispersing the particles well in the medium [26]. Additionally, in the case of a solution containing both CMC and SBR, the binders interact in an associatively. When this binder solution is added to the graphite particles, they are adsorbed onto the surface of the graphite particles, resulting in dispersion due to the repulsive force from the CMC solution [23], [26], [57].

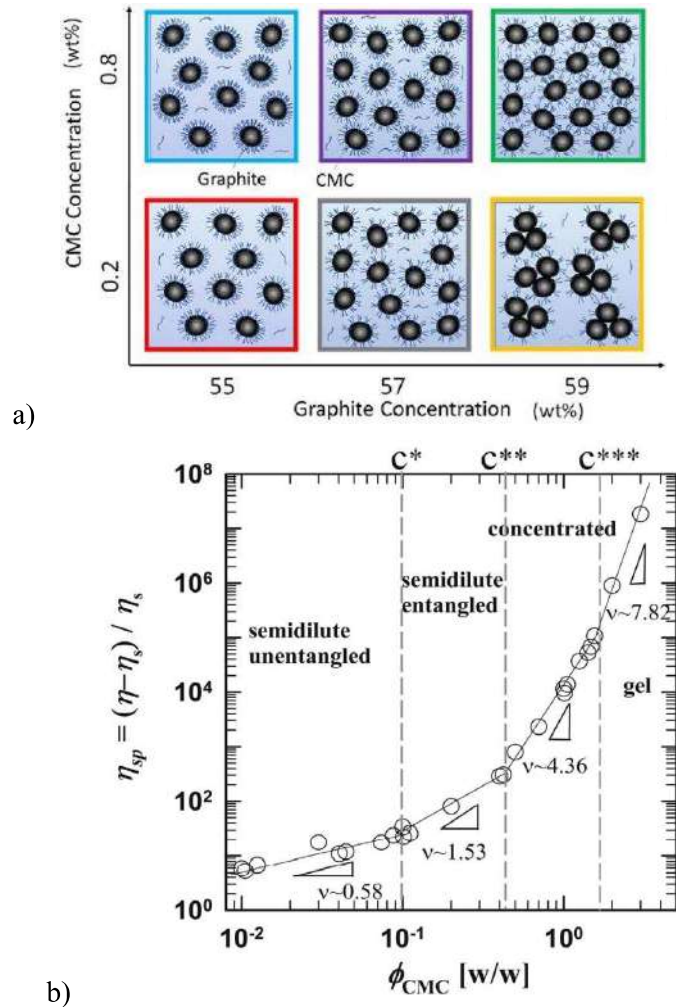


Figure 2.11: a) CMC-graphite concentrations [28], b) CMC dosage-viscosity relationship [57].

If CMC is in contact with the graphite particles first, when there is a meager dosage/ratio of CMC to graphite, the graphite particles will form a gel structure due to hydrophobic attraction. However, when the CMC ratio is not too low, the graphite particles will be dispersed in the slurry due to the electrosteric (electrostatic and steric effects) repulsion caused by the CMC adsorbed onto the surface of the graphite particles. This is because the amount of CMC adsorbed on the surface of the graphite particles also increases [28], [57]. On the other hand, when the ratio of CMC to graphite is high, the graphite particles will form aggregates due to depletion attraction from the non-adsorbed CMC in the medium, resulting

in the slurry exhibiting a gel-like behavior again due to the formation of a polymeric network structure by the CMC molecules at high concentrations of CMC molecules [26], [28], [38]. The influence of CMC dosage on graphite and viscosity is illustrated in Figure 2.11.

If SBR is added to a mixture already containing graphite particles and a high dosage of CMC, the remaining CMC molecules that are not adsorbed to the graphite particles will get adsorbed associatively with the SBR molecules. The CMC on the graphite particles and those associated with the SBR molecules will then repel each other, preventing SBR from adsorbing onto the graphite particles [22]. On the other hand, if a low dosage of CMC is mixed with graphite particles, the graphite particles do not have sufficient CMC molecules adsorbed onto them (since the amount of CMC adsorbed increases with CMC dosage). When SBR is added, it can adsorb on the graphite particle's surface and, synergistically with CMC, influence dispersion (similar to a CMC/SBR solution) [25], [26], [28], [38].

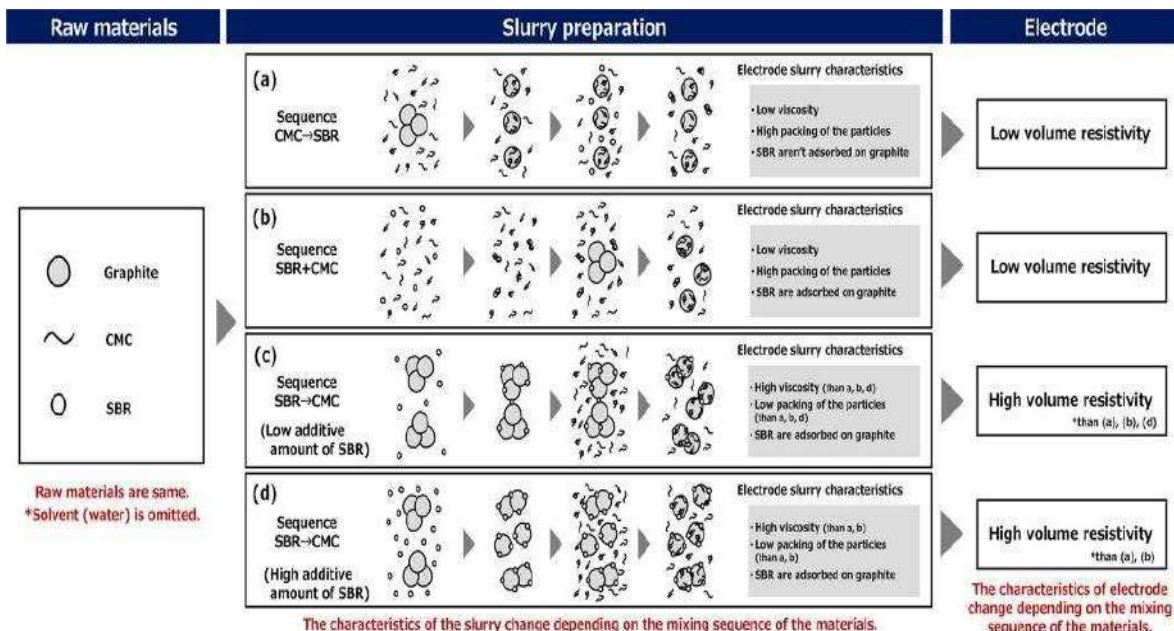


Figure 2.12: Summary graphite–binder mixing sequence of anode slurry dispersion [26].

Therefore, optimized electrode sheets or electrode structures with a low-volume resistivity can be obtained from slurries (summarized in Figure 2.12) in which the graphite particles are uniformly dispersed [26]. The adsorption state of the binder affects the particle dispersion state in the slurry, resulting in changes in the slurry's rheological properties and the particles' packing characteristics [23], [38]. These changes in mixing sequence can influence the performance of the electrodes, even if the material composition remains constant [26].

Further, studies have reported the influence of carbon black in the graphite anode slurry. The authors stated that carbon blacks, due to its nano size and consequent high surface area, primarily appear as aggregates and tend to form secondary aggregates with sizes in the range of several hundred nanometres owing to the hydrophobicity of carbon black surface [23], [36], [43]. Moreover, carbon black is in the

same range as the interface with the dispersion medium and, based on this, can influence the dispersion [36], [51]. Conversely, graphite cannot form fractal structures since it is in the micrometre range in size or hydrodynamic. Adsorbing a polymer dispersant to the carbon-black particles can also improve dispersion stability, particularly when the polymer dispersant has a hydrophobic structure that promotes a steric repulsive force between the nanoparticles [36]. In a slurry of carbon-black and polymer, the interaction between particles is influenced by polymer steric interaction. The strength of attraction between two carbon black particles depends on the length of the absorbed polymer brush. When the distance between the particles reaches $2L$ (L is the adsorbed polymer brush length), the polymer steric repulsion becomes stronger than the Van der Waals attraction [43]. With a lower molecular weight polymer, the brush length is smaller, and the attraction between particles is stronger, resulting in faster reaction/aggregation than particle diffusion. As the molecular weight increases, the polymer brush length becomes larger, and the attraction between particles becomes weaker [58]. Therefore, in the graphite anode slurry, particles in the nanometer range exhibit stronger colloidal forces or interaction and thus impact the anode slurry more [27], [43], [51].

2.3 COATING PROCESS

The electrode fabrication process involves depositing the slurry onto a substrate (current collector). The coating technique and parameters are crucial in ensuring uniform distribution and preservation of the slurry's network structure. The rheological properties of electrode slurries used in lithium-ion battery production significantly impact on the manufacturing process and the quality of the batteries [16], [43]. Rheology is used to study the behavior of the slurry before coating, to understand the impact of different mixing conditions on the assembly structures [23], [25].

2.3.1 RHEOLOGY

Rheology studies how materials flow and deform in response to applied forces or stress [45]. It utilizes principles from mechanics, such as forces, deflections, and velocities, to understand the physical properties of materials and how they behave under different conditions, including temperature, pressure, shear rate, and loading duration [25], [45]. Two extremes can characterize a material's deformation or flow behavior: elastic (solid-like) and viscous (fluid-like). While most materials have both properties, the material's behavior can fall at extremes or anywhere in between. To investigate non-Newtonian flow behaviors, there are two main types of rotational tests: controlled shear rate (CSR) and controlled shear stress (CSS). Controlled shear rate (CSR) involves pre-setting the rotational speed or shear rate, and controlled shear stress (CSS) involves pre-setting the torque or shear stress. The rheometer controls the pre-set parameters in both testing modes [45], [59].

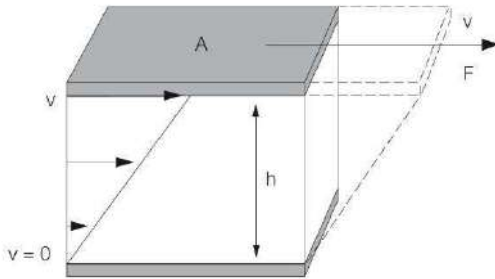


Figure 2.13: Two-plate model of rheology [59]

The typical setup for performing rheological tests is the two-plate model (Figure 2.13), which is based on the assumption that the flow is laminar. The model enables measurement of the resulting velocity (v) of the upper plate (of area A) for a material placed between the two plates with a specific distance (h) when a shear force (F) is applied to it, and the lower plate is held stationary [42], [45]. All fluids in motion have relative motion between their molecules, which leads to internal frictional forces and a certain amount of flow resistance, which can be quantified using the fluid's viscosity. Viscosity is a measure of a fluid's resistance to flow, determined by the strength of the attraction between the fluid's molecules and the size of the molecules. Accurate measurement of the rheological parameters is only possible if specific conditions are met [59]. The shear viscosity is the ratio of the shear stress to the shear rate. Flow curves which depict the relationship between shear stress (τ) and shear rate ($\dot{\gamma}$), and viscosity curves are products of rheological measurements [45]. Thus shear stress, shear rate and viscosity are defined by the following equations [45], [59]:

$$\text{Shear stress } \tau = \frac{\text{shear force } F \text{ (N)}}{\text{shear area } A \text{ (m}^2\text{)}} ; \text{Unit (kg.m.S}^{-2}\text{)} \quad (\text{Eqn. 2.2})$$

$$\text{Shear rate } \dot{\gamma} = \frac{\text{velocity } dv \text{ (mS}^{-1}\text{)}}{\text{distance } dh \text{ (m)}} ; \text{Unit (S}^{-1}\text{)} \quad (\text{Eqn. 2.3})$$

$$\text{Viscosity } \eta = \frac{\text{shear stress } \tau}{\text{shear rate } \dot{\gamma}} ; \text{Unit (Pa.S)} \quad (\text{Eqn. 2.4})$$

2.3.1.1 STEADY-STATE FLOW BEHAVIOUR

The flow behaviors of materials depend on the shear load applied (Figure 2.14). Fluids with a resistance to flow proportional to the flow velocity are referred to as Newtonian fluids and have a constant viscosity regardless of the shear load. Shear thinning is when viscosity decreases with an increase in shear rate due to inhomogeneous deformation and material flow characteristics related to its internal structures. Conversely, Shear thickening is when viscosity increases with an increase in shear rate, as often observed in dispersions at high particle concentrations, in highly concentrated, chemically unlinked polymer solutions and melts due to mechanical entanglements between the molecule chains. Both shear thinning and shear thickening play a role in the formation and shape retention of wet films [28], [45], [59].

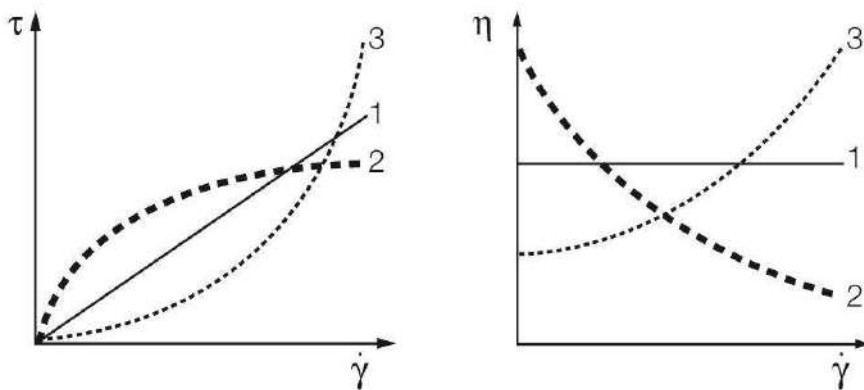


Figure 2.14: Flow and viscosity curves for (1) ideally viscous, (2) shear-thinning, and (3) shear-thickening flow behavior [59].

2.3.1.2 TIME-DEPENDENT FLOW BEHAVIOUR

The time-dependent flow behavior of materials is measured at constant shear rates. This measurement can be used to demonstrate structural decomposition and regeneration, known as thixotropy and rheopexy, respectively. Thixotropy is the property of some solidified colloids to temporarily become a liquid when subjected to mechanical forces, resulting in a structural change or transition. One approach to measure thixotropic behavior is the 3ITT test (Figure 2.15), which consists of three intervals: a low-shear phase where the material is at rest and the viscosity is constant, a high-shear phase simulating the application process and providing the viscosity under a strong shear force, and a low-shear phase where the sample can recover its structure and viscosity, allowing for the structural regeneration of the sample to be determined using various analysis methods [45], [59].



Figure 2.15: 3ITT test approach for (1) constant low shear, (2) constant high shear rate, and (3) the same constant low shear as in the first interval [59]

2.3.1.3 OSCILLATION TESTS AND VISCOELASTICITY

Oscillatory tests, also known as dynamic mechanical analysis (DMA), are used to evaluate the viscoelastic properties of materials that exhibit viscous and elastic behavior when sheared. These materials include polymer solutions, dispersions, pastes, gels, elastomers, and even rigid solids. The complex shear modulus (Figure 2.16), a measure of the deformation energy stored by the material during the shear process, describes the entire viscoelastic behavior of the material [45], [59]. This is based on Hooke's law, which states that the deformation of a material is proportional to the applied force, as presented in the equation:

$$\text{complex shear modulus, } G^* = \frac{\text{shear stress amplitude } \tau(t)}{\text{shear strain amplitude } \gamma(t)}; \text{ Unit (Pa)} \quad (\text{Eqn. 2.5})$$

where G^* is the complex shear modulus in units of Pa, and $\tau(t)$ and $\gamma(t)$ are sinusoidal functions with units of Pa and 1, respectively.

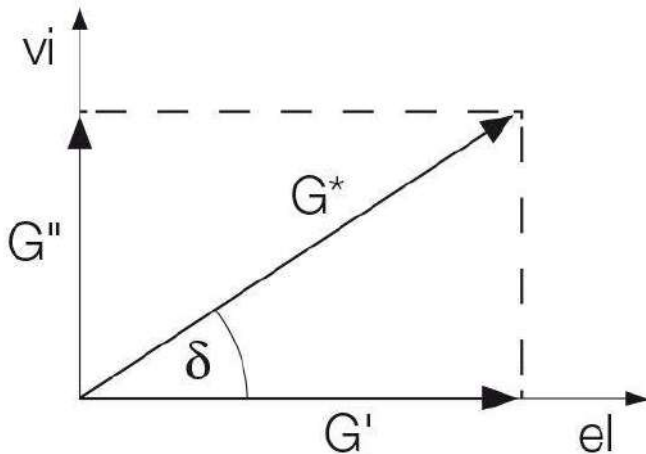


Figure 2.16: Relationship between complex shear modulus G^* , storage modulus G' and loss modulus G'' using the phase-shift angle δ [59].

The storage modulus (G') represents the elastic behavior of a material, which is the amount of deformation energy that is completely retained after the load is removed and drives the reformation process, due to stretching of the internal structures without overstressing the interactions or damaging the material. The loss modulus (G'') represents the deformation energy that is used up by the material during the shear process and is lost due to internal friction between the molecules and particles. This energy is spent on changing the material's structure as it flows. The phase shift (δ) is the time lag between the applied and the resulting sinusoidal oscillation. The $\tan \delta$ is the loss factor, which is the ratio of the lost deformation energy to stored deformation energy. It reflects the ratio of the viscous to the elastic behavior of the material [35]. The storage modulus describes the solid-state behavior of the sample, while the loss modulus describes the liquid-state behavior of the sample. Commonly, two types

of oscillation tests are amplitude sweep and frequency sweep, which can be used to analyse a sample's time-dependent behaviour [45], [59].

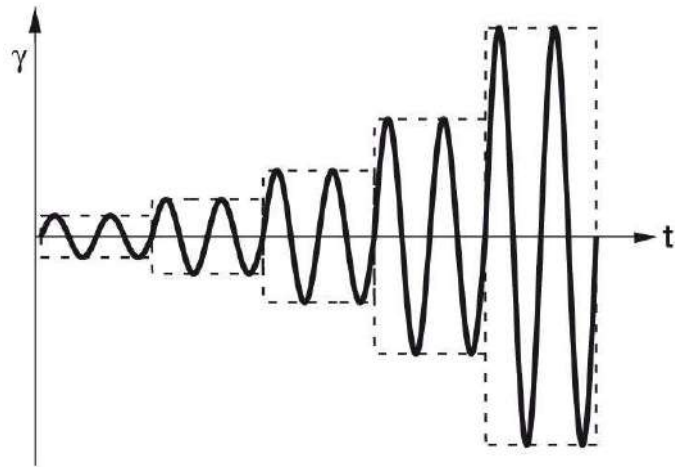


Figure 2.17: Pre-set of an amplitude sweep test [59]

The amplitude sweep test measures the deformation behavior of a material at a constant frequency (Figure 2.17). It helps to determine if the material is a viscoelastic solid or liquid (Figure 2.18), which exhibits both viscous and elastic properties. The test can also be used to understand the balance between these properties for optimal practical use. The viscoelastic solid ($\tan\delta > 1$ (since $G' > G''$)) will exhibit reversible deformation, returning to its original shape after a load cycle, while the viscoelastic liquid ($\tan\delta < 1$ (since $G'' > G'$)) does not, and at the sol-gel transition point, $\tan\delta = 1$ (since $G' = G''$). Additionally, the amplitude sweep test can help understand the internal friction and permanent alteration of the internal structure of the material due to the viscous behavior. A part of the resulting friction heat may heat the sample itself or be conducted to the outside, being lost to the sample [59].

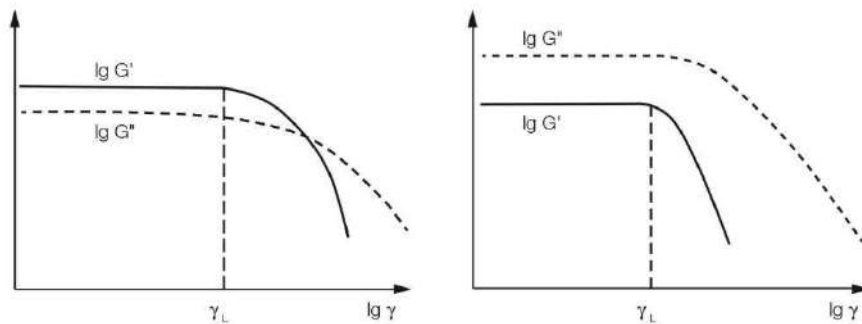


Figure 2.18: Amplitude sweep curves for viscoelastic solid (left) and viscoelastic liquid (right) [59].

In frequency sweep testing, the oscillation frequency is controlled, and the amplitude is kept constant (Figure 2.19) to study the time-dependent behavior of a sample under non-destructive deformation.

High frequencies simulate quick motion over short periods, while low frequencies represent slow motion over more extended periods or when the material is at rest. This test provides insight into the stability of the dispersion over time [59].

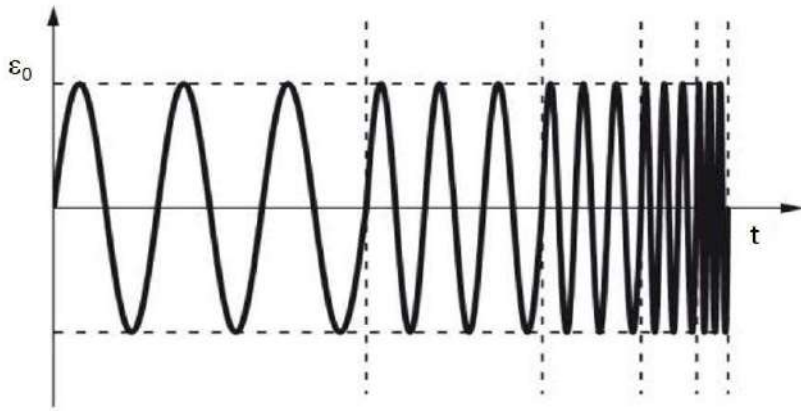


Figure 2.19: Schematic profile of the applied deformation during a frequency sweep test [59].

Graphite anode slurries with high solid content are gaining attention because they can result in electrodes with high capacity and performance. This is due to the higher ratio of electrochemically active material to electrochemically inactive content. Low solid content in a slurry used for battery electrode manufacturing can result in several issues, including a decrease in electrochemical performance due to a lower amount of active material present in the electrode. Additionally, achieving a uniform coating of the slurry onto the current collector can be more challenging, and low solid content can increase the likelihood of defects such as cracks or voids in the electrode, which can lead to variations in electrode thickness and further degrade electrochemical performance. On the other hand, higher solid content in the slurry can lead to higher ratios of active material in the final electrode, as a thicker coating of active material can be achieved on the current collector, resulting in increased electrochemical performance. However, the morphology of the solid particles in the slurry can affect the viscosity and flow, leading to either shear thickening or shear thinning, depending on the factors previously discussed (in section 2.4.3.1). Shear thinning can be desirable in some applications, but the rheological properties of the slurry must be carefully controlled to achieve the desired viscosity at both low and high shear rates. On the other hand, shear thickening can cause problems, such as clogging of pipes or filters [25], [28]. To overcome these issues, it is crucial to fully disperse the particles in the slurry and form a network structure in the static state [28]. Additives such as dispersants and thickeners (for instance, carboxymethyl cellulose) may be used to achieve these goals [23], [28], [34].

2.3.2 COATING

In the battery industry, a coating is used to create electrodes that are essential components in the functioning of the battery. Electrode coating in battery technology refers to the thin coating of an

adequate quantity of slurry (active mass) to form a layer on a substrate (such as aluminium or copper), forming an electrode. The most common technique for electrode coating for industrial production of lithium-ion-batteries is the roll-to-roll (R2R) coating process, in which electrode material is coated onto a substrate and transferred with the help of rollers [15], [43], [51]. Doctor blade coating is also a common lab-scale coater that uses a flat blade to evenly spread the slurry and remove any excess material, especially on a laboratory scale [5]. Equipment used in doctor blade coating includes a coating station and a doctor blade. The process of using the doctor blade is also known as tape casting [60]. Other industrial electrode coating techniques include extrusion and slot die application [5], [15]. The coating process is crucial to optimize electrode performance. So the coating parameters, such as coating speed and temperature, must be controlled to obtain the desired thickness, uniformity and adhesion of the coating to the substrate.

2.3.3 MULTILAYERING APPROACH

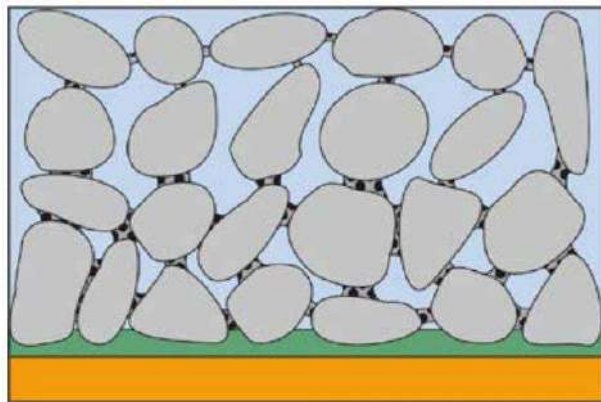


Figure 2.20: Illustration of a single-layer coating [19]

The single-layer coating (illustrated in Figure 2.20) can be a layer of coating on one side of the current collector or a layer per side on both sides of the current collector. It is a widely used way of depositing due to its simplicity; that is, it is relatively easy to control the thickness and uniformity of the coating and cost-effectiveness, especially in large-scale production. However, it is challenging to achieve specific functionalities, among which is the high energy density or capacity, which is obtainable with increased mass and corresponding increased thickness. To this end, the multilayer coating approach is emerging for lithium-ion electrodes.

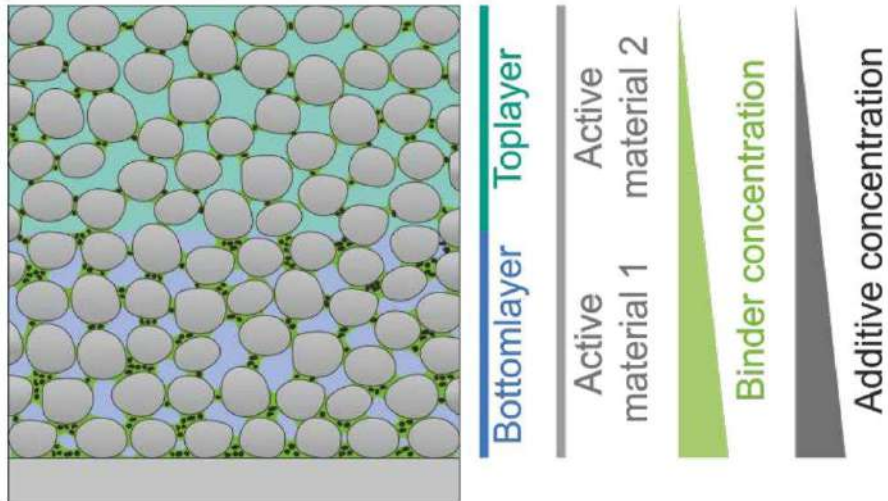


Figure 2.21: Illustration of multilayering [19]

The multilayer approach (illustrated in Figure 2.21) involves the application of multiple layers of material onto a substrate in a controlled manner. This technique offers the potential to achieve complex multilayer structures and specific functionalities, not achievable with single-layer coating [3], [7]. There is sparse information available about the feasibility of manufacturing thick electrodes using the multilayer approach, as it is currently an active area of research; however, some studies have examined the use of freeze casting to create multilayer electrodes and have found that the areal capacity can be increased with thickness, the layers can inter-penetrate each other due to internal capillary pressure during drying of multilayers [1], [3], and that better adhesion of the active mass to the current collector can be achieved. Other researchers have implemented the multilayering approach through slot die coating to fabricate electrodes. These studies have found that the additive and binder distribution can be adjusted by combining different slurries, which leads to weight savings while also improving cell performance.

Additionally, different active materials can be combined to improve efficiency. They established that multilayer and conventional single-layer anodes are chemically identical and have identical thicknesses. The only difference between them is the engineered architecture imposed on the multilayer version. When multilayer anodes and their homogeneous baselines are paired with the same electrolyte, separator, and cathode, assembled into the same cell design, and tested under the same conditions, any difference in performance can be attributed solely to the engineered mesoscale architecture [7]. In summary, the multilayer approach can be utilized to improve the rate performance of lithium-ion batteries (LIBs). This enhancement becomes apparent through changes in electrode processing and properties, as well as overall battery performance [1], [3], [61].

2.4 POST-FABRICATION PROCESS

Drying, calendaring, cell assembly and testing are encompassed in the post-coating process. Drying the anode in lithium-ion batteries is critical because the anode coating is usually applied in a wet state and must be dried to remove solvents, especially true for water-based processing due to the high reactivity of the components with water [5], [7], [17]. In addition, the SEI layer protecting the graphite anode and preventing dendrites from forming can be attacked by hydrofluoric acid (with H from moisture in the electrode and F from the electrolyte salt, LiPF₆), which can lead to short-circuiting and decrease battery performance and lifespan [62]. Therefore, it is crucial to dry the anode to remove all residual moisture. Further, calendaring is crucial for the dry electrode because it helps to achieve a uniform thickness and smoothness of the coating. After all, a consistent and uniform coating thickness is essential for proper battery cell performance. Both drying and calendaring can help to improve the overall appearance, quality of the electrode, performance and safety of the battery [5], [15], [63].

Cell assembly is the final step of lithium-ion battery manufacturing, where the anode, cathode and separator are assembled to form a complete cell. It is essential at this point to ensure that the battery is assembled correctly, with the anode and cathode in the correct position and the separator inserted adequately between them. A proper assembly yield cells with good contact and conductivity between the electrodes and current collectors and maintain the safety and performance of the battery over its lifetime [15], [63].

2.4.1 ELECTRODE CHARACTERIZATION TESTS

Several tests and techniques can be used to simulate and characterize the performance of lithium-ion cells under environmental and application conditions.

Mechanical testing involves evaluating the mechanical properties of the electrode using techniques such as tensile testing, compression testing, and bend testing. The Peel and Drag tests are used to evaluate the mechanical integrity or strength of electrodes in battery manufacturing [52].

A Peel test, also known as a "drag-out" test, is a technique used to determine the mechanical robustness of electrodes used in battery production. It involves attaching the electrode to a sample plate and then applying a force to pull it off the sample plate. The force required to detach the electrode is measured and used to evaluate the adhesion strength of the electrode to the substrate. This test is used to assess the mechanical properties of the electrode, such as adhesion strength, flexibility, and cohesion. It simulates the mechanical stress the electrode material will experience during battery cycling and indicates its ability to withstand these stresses without breaking or delaminating. The results of the test can be used to compare different electrode materials or formulations, as well as to evaluate changes in the properties of the same material over time [22], [52], [64].

Electrochemical testing involves measuring the electrical properties of the electrode using techniques such as cyclic voltammetry, galvanostatic cycling, and electrochemical impedance spectroscopy [65].

Galvanostatic cycling is a technique used to evaluate the performance of batteries and other electrochemical devices by applying a constant current to the device and measuring the voltage as a function of time. This information is used to determine the device's capacity, energy efficiency, and other performance characteristics. This is typically done within a fixed potential window, such as 3.0 V to 4.2 V. The current is usually expressed in C-rate, which represents the charge or discharge rate equal to the battery's capacity in terms of hour, and the magnitude of the current determines the rate of the charge and discharge processes [65].

$$C - \text{rate} = \frac{\text{current (Amps)}}{\text{battery capacity (Ah)}}; \text{Unit } \left(\frac{1}{\text{h}}\right) \quad (\text{Eqn. 2.6})$$

Microstructural analysis, thermal analysis, and electrolyte compatibility testing are other tests to characterize LiBs.

EXPERIMENTAL METHODS AND OUTCOMES

3. OVERVIEW OF MATERIALS AND METHODS

This study employed a mixed research design approach to assess the developed anodes. A digital microscope was used to examine the microstructure and mechanical adhesion of the anodes. In addition, a series of experiments to determine the slurry properties, electrode properties, and electrochemical properties were studied quantitatively. The experimental design is motivated by a need to achieve the factors and samples required for each analysis. The design of the experiment aims to address the problem of lack of mechanical integrity during the fabrication of thick, defect-free aqueous anodes for lithium-ion cells. The performance of the electrodes is hindered by the presence of pinholes, agglomerates, and delamination from the current collector (Figure 1.4).

The objectives of the work are to improve the flexibility of the electrodes to the bending radius of the R2R coater while maintaining good adhesion for post-coating processes. The target performance is defect-free electrodes with good mechanical stability/adhesion and electrochemical performance. The experiment considers two formulations and two layers to meet the objectives. Therefore, thick single-layer samples will be created using the first formulation, and multilayer samples will be produced using both formulations.

It is important to note that different terms are used to refer to the distinct active material (graphite), and their slurries and resulting electrode in each section, as outlined in Table 3.1.

Table 3.1: Designation

<i>Section designation</i>	<i>Supplier A</i>	<i>Supplier B</i>
<i>Materials section</i>	Type A	Type B
<i>Slurry/Rheology</i>	Slurry A	Slurry B
<i>Mechanical</i>	Electrode A or Anode A	Electrode B or Anode B
<i>Electrochemical</i>	Cell A	Cell B

3.1 RAW MATERIAL CHARACTERIZATION

This section presents the series of experiments that examined the graphite brands and subsequent results and discussion based on the observations per experiment. This study compared two graphite materials with distinct characteristics from different suppliers (Hitachi and Targray).

3.1.1 PARTICLE SIZE EVALUATION

To further understand the differences in particle characteristics, the CILAS particle size analyzer was utilized to identify the size of the graphite particles and offer more specific information about their dimensions.

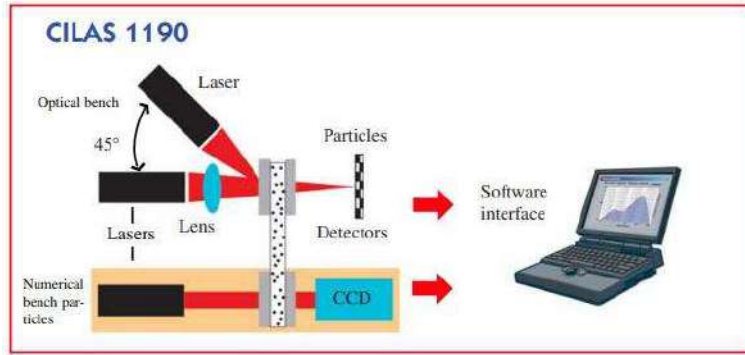


Figure 3.1: Schematic of CILAS particle analyzer [66]

Laser diffraction is a technique used to measure the size distribution of particles in a sample, and the CILAS particle sizer is an equipment that utilizes this method (Figure 3.1). It can measure particles in the 0.04 - 2500 μm and analyze both liquid and dry samples. The technique uses laser diffraction to measure the angular variation in the intensity of light scattered as a laser beam passes through a dispersed particulate sample (Figure 3.2) and then applies the Mie theory of light scattering to calculate the size of the particles. It has been used in various industries such as pharmaceuticals, construction, and metallurgy [67], [68].

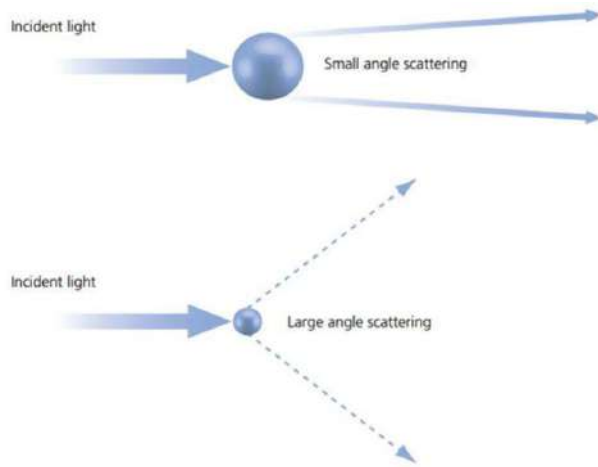


Figure 3.2: Diffraction scattering angles [68]

3.1.2 BRUNAUER-EMMETT-TELLER (B.E.T) SURFACE EVALUATION

The material morphology characterization of both graphites ended with a surface area analysis experiment. The test was performed using a Quantachrome (Autosorb-iQ-MP/XR) BET equipment, as illustrated in Figure 3.3.



Figure 3.3: Quantachrome BET equipment

The samples were treated to remove impurities and moisture by subjecting them to vacuum conditions at approximately 110 °C for approximately 6 hours. The instrument was calibrated using helium gas, which does not adhere to the surface of the powdered samples. The BET analysis was carried out at a low temperature using nitrogen gas, which adheres to the surface of the samples and forms a monolayer. After forming the gaseous monolayer, the sample is placed in a non-nitrogen atmosphere and heated to release the adsorbed nitrogen gas molecules from the sample's surface. The released gas molecules can then be quantified to calculate the surface area and porosity of the sample. The adsorption process is kinetically limited, and the cold temperature of the liquid nitrogen facilitates rapid kinetic equilibrium. During the actual test, the instrument introduced known quantities of ultra-pure nitrogen gas into the tube while recording the pressure (P/P_0) and determining the parameters.

3.1.3 RESULTS AND DISCUSSION ON MATERIAL CHARACTERISTICS

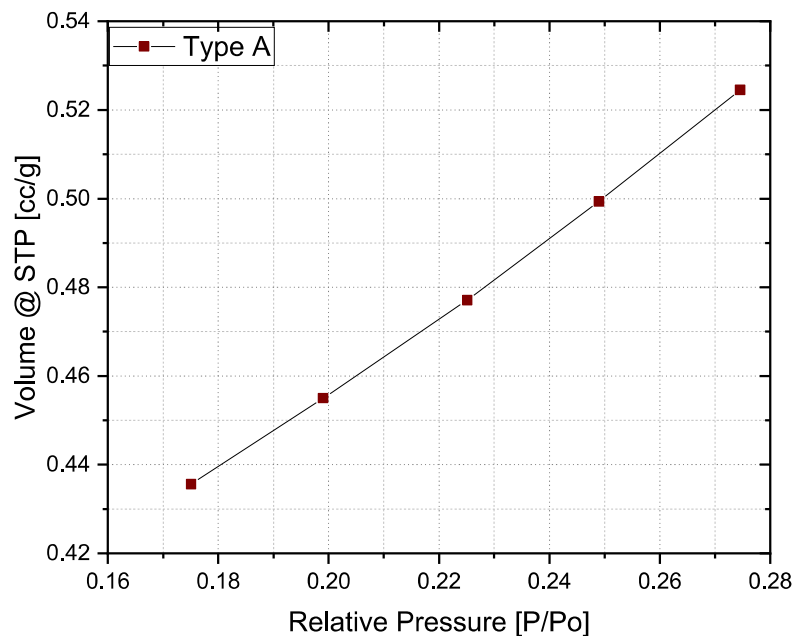
Table 3.2 present the average diameter obtained from the CILAS particle sizer. The measurements from the CILAS particle sizer, at the 10%, 50%, and 90% confidential intervals, indicate that most particles from both Type A and Type B graphite are smaller than 20 μm in diameter. Furthermore, the data collected from only 10% of the particles allows for a more focused evaluation of a smaller subset, which is likely more accurate and provides a more detailed analysis of the sample's morphology. Thus, the CILAS measurements alone indicate that the particle size of both types of graphite is comparable, with only a small variation.

Table 3.2: CILAS particle size of both graphite brands

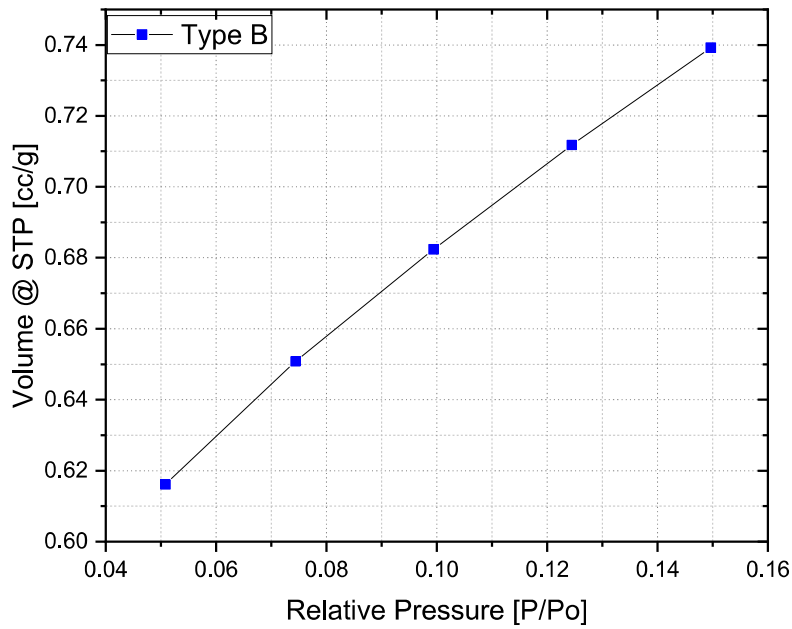
Graphite	Diameter 10% [μm]	Diameter 50% [μm]	Diameter 90% [μm]
Type A	6.80	14.36	24.84
Type B	5.54	15.17	29.78

Further, the BET surface area test results for both Type A and Type B graphites are illustrated in Figure 3.4. The graph shows the relationship between the volume of nitrogen gas introduced per sample mass

and the relative pressure (P/P_0). The data suggest a linear relationship between the two parameters for both types of graphite. However, while Type A graphite has a higher relative pressure than Type B graphite, the volume of adsorbed gas molecules onto Type A graphite is observed to be lower than for Type B graphite. Moreover, the specific surface area (calculated using equation 2.1) for Type A and Type B graphites showed that Type A had a specific surface area of $1.789 \text{ m}^2/\text{g}$; in comparison, Type B had a specific surface area of $2.809 \text{ m}^2/\text{g}$, both with a correlation coefficient of 0.999. This indicates that the specific surface area of Type A is lower than that of Type B graphite.



a)



b)

Figure 3.4: Volume of nitrogen as a function of relative pressure for a) Type A and b) Type B graphite

While The CILAS particle analyzer suggests that the particles of both graphites are similar in size, the BET surface area analysis has revealed a difference between the two types of graphite, particularly in terms of surface area. Surface area can give an insight into the shape or size of particles [46]. Relying solely on particle size differences alone would have led to the conclusion that Type A graphite has larger particles than Type B graphite. However, based on the findings from the CILAS particle analyzer, the BET surface area measurement has revealed a distinction in the particle shape. The CILAS particle sizer had previously established that the particle sizes of both Type A and Type B graphites are similar, so the difference in shape must have been the cause of the distinction in tap densities. The BET surface area analysis clarified that the distinction between the two types of graphite is due to their shape. A small specific surface area is an attribute of regularly shaped particles, while particles with an irregular shape have a larger specific surface area [46].

Therefore, it can be inferred that Type A graphite has a smaller specific surface area, which implies a regular particle shape, leading to higher packing density and smaller pore size/volume. On the other hand, Type B graphite has a larger specific surface area, indicating an irregular particle shape, resulting in lower packing density and larger pore size/volume. The variation in relative pressure and volume adsorption between the two types of graphite confirms the difference in their pores [46].

Having determined that the materials are distinct and recognizing that the particle shape variation results in a high packing density (with small pore size/volume) of Type A graphite and a low packing density (with large pore size/volume) of Type B graphite, it is likely to have a substantial effect on the properties

of the slurry. The following section will examine the slurries made from the different graphites, with all other slurry constituents being kept constant or in comparable amounts. The only variations that will be observed are the characteristics of the distinct graphites.

3.2 SLURRY CHARACTERIZATION

This section describes the series of experiments that evaluated the density and rheology of the slurries made from the different graphite brands, followed by results and discussion based on the observations from each experiment. The study compared the impact of the distinct graphite materials on the measured properties within the slurry, with all other slurry constituents being kept constant or in similar proportions.

3.2.1 SLURRY MIXING

The ingredients in the slurry were combined in a ratio to attain 55% solid material and a final dry weight of 10 grams.

Table 3.3: Proportion of slurry constituent for a total dry mass of 10 grams

	<i>Slurry Formulation</i>	<i>Formulation 1 (F1)</i>	<i>Formulation 2 (F2)</i>
<i>s/n</i>	Content	Dry target [%]	Dry target [%]
1.	AM	95	94
2.	CB	2	2
3.	CMC	1	2.5
4.	SBR	2	1.5
	Total	100	100

To prepare the anode slurry, a solution containing 2 wt.% battery-grade sodium carboxymethyl cellulose (WALOCEL™ CRT 2000 P.A., DuPont de Nemours Inc.) was made by dissolving the CMC in deionized water (Figure 3.5) using a mechanical dissolver/stirrer (DISPERMAT CV3- PLUS, VMA GETZMANN GMBH). The solution was mixed at a starting rotational speed of 1000 rpm for 1 hour, then increased to 1500 rpm for an additional hour with the propeller moving up and down to ensure thorough mixing. The solution was allowed to mix overnight at a lower speed of 500 rpm. At the same time, the as-received graphite powders (of different particle characteristics from two suppliers) were also dried in an oven overnight at 80 °C.



Figure 3.5: $\text{CMC}_{\text{solution}}$ mixing setup

The mixing sequence recommended in the literature [26] was followed to obtain a well-dispersed slurry, and the proportions of each material in the slurry were based on the formulations in table 3.4. The slurry was prepared using the sequence: $\text{CMC} \rightarrow \text{graphite} \rightarrow \text{CB} \rightarrow \text{SBR}$. The first step in preparing the slurry was by mixing the graphite and CMC solution (Figure 3.6a) in a container using a planetary centrifugal mixer (THINKY MIXER, ARE-310, THINKY Co., Japan) at 2000 rpm for 90 seconds. The second step (Figure 3.6b) was the addition of Carbon-black (C-NERGY™ SUPER C45, TIMCAL Ltd.) and mixing at 2000 rpm for an additional 90 seconds. The final step was the addition of the latex, a 40 wt.% styrene butadiene rubber suspension (Figure 3.6c) and mixing the entire slurry at a lower speed of 600 rpm for 120 seconds.



Figure 3.6: Slurry plus a) Graphite plus $\text{CMC}_{\text{solution}}$, b) Carbon black, c) SBR

The protocols for mixing with the Thinky mixer were followed during each mixing step. Besides, when preparing the second formulation with the 2 wt. % CMC solution, it is essential to note that additional deionized water was added to the CMC -graphite slurry to dilute it and achieve a total solid content of 55 %. The diluted slurry was mixed at 2000 rpm for 90 seconds before carbon black was added for the second formulation.

3.2.2 PYCNOMETER DENSITY EVALUATION

The density of the various slurries was then determined using a pycnometer density cup with a volume of 50 ml. The mass of the empty cup before- and after adding the slurry was recorded. The mass of the

empty cup was subtracted from the cup's mass with slurry to determine the tap density of the slurry. This process was carried out according to all necessary protocols [69].

3.2.3 RHEOLOGICAL EVALUATION

As the final experiment for the characterization of the prepared slurry, the rheological properties were determined using a rheometer (MCR302e, Anton Paar, Austria). The slurry was mixed with a spatula for 1-2 minutes before being placed on the rheometer's plate (diameter 50 mm) with a 1 mm testing gap between the rotating top plate and the fixed bottom plate (Figure 3.7). Peltier cover was utilized to ensure temperature consistency during testing. All experiments were conducted at 25°C with proper procedures followed.



Figure 3.7: Anton Paar Rheometer

3.2.3.1 STEADY-STATE FLOW EVALUATION

The procedure began with a steady state flow test to evaluate and compare the flow and the effect of shear rate on viscosity, with each trial repeated three times. The shear stress and viscosity of the slurries were measured using the step-up method of the shear rate sweep (CSR) test as the shear rate gradually increased to a preset value of 500 s⁻¹. This preset shear rate includes the range of shear rates required for Doctor Blade coating applications and simulates the electrode coating process relevant to this study.

3.2.3.2 TIME-DEPENDENT EVALUATION

The thixotropy and recovery characteristics of the slurries were subsequently evaluated using a three-step flow procedure. In the first step, a low shear rate of 0.1 s⁻¹ was applied to the sample to mimic the rest status of all molecules. In the second step, different high shear rates were preset (15 s⁻¹, 50 s⁻¹ and 100 s⁻¹, respectively) to mimic the coating application shear rate for each slurry, and the changes in viscosity were recorded. In the third step, the preset shear rate of 0.1 s⁻¹, similar to the first interval, was applied to simulate the moment when shearing is stopped, and the slurry's recovery from the viscosity

change perspective was monitored over time. The measurement at each specific shear rate was carried out for about 190 seconds.

3.2.3.3 VISCOELASTICITY EVALUATION

The final test of the rheological study assessed the dynamic and viscoelastic properties of the slurries. This examination showed how the elastic moduli depend on strain and angular frequency to determine the level of shear thickening and the stability of the slurries [18]. The amplitude sweep test measured the storage modulus (G') and loss modulus (G'') of the slurry at a constant angular frequency (preset oscillating shear rate of 10 s^{-1}) over a range of shear strains from $10^{-2} \%$ to $10^2 \%$. Additionally, the frequency sweep was measured over a range of $10^3 \%$ to $10^{-1} \%$ at a small shear strain oscillation of 0.1 %, which falls within the linear range of the sample. All these measurements were done at a temperature of 25°C . The anode slurries were left to rest for about 3 minutes before conducting the rheological measurements to ensure that the results were not affected by previous shearing.

3.2.4 RESULT AND DISCUSSION ON SLURRY CHARACTERISTICS

The method of mixing used in this study follows established protocols described in the literature [26]; however, in this specific slurry, a Carbon-black (CB) step is added before incorporating SBR. As shown in Table 3.3, the prepared slurry mixture comprises a significant amount of graphite mixed with a small amount of CMC already dissolved in water, followed by the addition of CB, resulting in a gel structure due to hydrophobic attraction as both graphite and carbon black are hydrophobic [36]. The CB formed a network with the binders, with the graphite particles embedded within the network (illustrated in Figure 3.10) [27]. Finally, when SBR was added, the concentration of SBR was appropriate to interact with the CMC, reducing the attractive force between the graphite particles and creating a repulsive force. This resulted in well-dispersed particles in the medium. The well-dispersed slurry is attributed to the synergistic influence of the binders (CMC and SBR). The low binder concentration, in comparison to the electroactive material (graphite) and the conductive agent (CB), implies a small polymer brush resulting in a smaller distance between the particles and a well-dispersed slurry via electro-steric repulsion [26]. Figure 3.8 shows the anodic slurry after mixing all the materials.



Figure 3.8: Graphite anode slurry

After the slurry mixing process, the respective slurries were evaluated to investigate and determine the influence of variations in density resulting from the use of different types of graphite.

Table 3.4: Pycnometer results

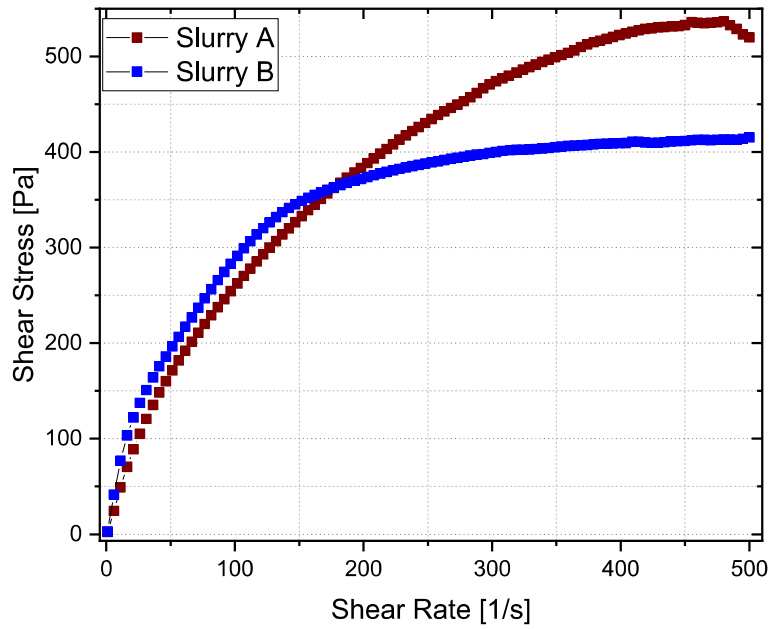
Graphite Type	Slurry A	Slurry B
<i>Mass(g)</i>	71.24	71.18
<i>Absolute density(g/cm³)</i>	1.43	1.42

The results from the pycnometer density test of 50 ml proportions of each slurry, as presented in Table 3.4, indicate that the slurries have similar masses and thus have comparable absolute density values. The consistency in mass and calculated density suggests that the proportion of the constituent materials is the same in both slurries. However, it does not reveal any variations in density resulting from the distinct shape of the different graphites.

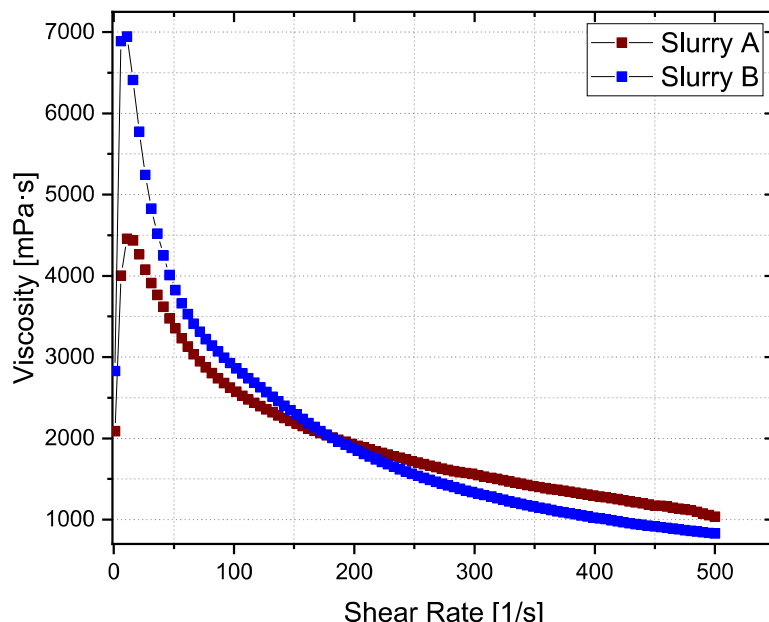
On the other hand, distinctions were observed in the rheological behaviors of both slurries.

The results of the steady-state flow behavior of both slurry A (wine color) and slurry B (blue color) are shown in Figure 3.9. Both slurries show a similar shear stress-shear rate relationship that is non-linear but at different magnitudes, as shown in Figure 3.9a. In the low to intermediate shear rate region (0 s^{-1} - 175 s^{-1}), it is observed that lower shear stress values were recorded for slurry A than slurry B, and in the intermediate to high shear rate region (175 s^{-1} - 500 s^{-1}), higher shear stress values were recorded for slurry A than slurry B. Likewise, both slurries show a similar viscosity-shear rate relationship that is non-linear but also at different magnitudes, as shown in Figure 3.9b. In the low to intermediate shear rate region (0 s^{-1} - 175 s^{-1}), it is observed that lower viscosity values were recorded for slurry A than slurry B, and at intermediate to high shear rates (175 s^{-1} - 500 s^{-1}), higher viscosity values were recorded for slurry A than slurry B. Overall, the flow and viscosity curves of slurry A are shallow, and both the flow and viscosity curves of slurry B are steeper in relation to the shear rate. While the flow curve indicates that both slurries exhibit a shear-thinning behavior, the viscosity curves, as shown in Figure

3.9b, indicate that both slurries exhibit an abrupt increase in viscosity initially (between 0 s^{-1} - 18 s^{-1}) at the onset of shearing to a peak viscosity value within the range and then an immediate decrease in viscosity beyond the peak viscosity value, indicating a shear thickening behavior precedes the shear thinning behavior.



a)



b)

Figure 3.9: a) Flow curve, and b) viscosity curves of slurries A & B

Due to the formation of a network of well-dispersed particles through electro-steric repulsion as a result of the optimized mixing sequence, the slurry can be likened to a network (molecules of different sizes and shapes) of solvated graphite particles connected by a binder-carbon black domain (that is, carbon-black intertwined with the polymer binder chains), as illustrated in Figure 3.10 [27], [70].

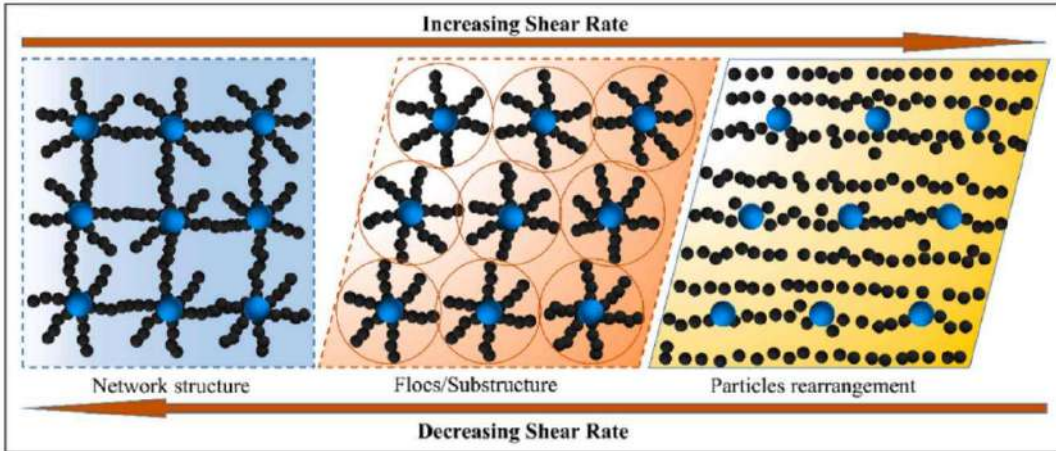


Figure 3.10: Illustration of the slurry response to shear rate [70]

Based on the observations from the plots, it can be inferred that at 0 s^{-1} , the binder (polymers) molecules in the slurry are curled and not in motion, and the particles are randomly oriented and undisturbed. The slurry behaves like a solid network structure. As the shear rate increases from 0 s^{-1} to about 18 s^{-1} , the strong inter-particle interaction of the slurry's components causes flow resistance. The initiation of movement in previously stationary particles leads to the gradual deformation of the slurry, resulting in more accidental particle collisions and the entanglement of polymer chains until 18 s^{-1} . This causes an increase in viscosity or shear thickening behavior, and high-stress values for deformation, as shown in the flow curve. As the shear rate increases, the consistency of the slurry shifts from solid-like to liquid-like due to the breakdown of the binder-carbon black chains. This results in the breaking down of the previous solid network structure into smaller flocs or sub-structures, causing a decrease in viscosity. This decrease in viscosity progresses as the curled binder molecules become untangled and the particles align in the direction of shear. The decrease in viscosity or shear-thinning behavior is reflected in the decrease of shear stress recorded as the shear rate increases due to the reduction of the initially strong inter-particle interaction.

The rheological behavior at low shear rates is primarily influenced by the inter-colloidal properties of the binder-carbon black particles [35], [70]. However, in this study, the difference in the observation for both slurries can be attributed to the distinct graphite shapes, as all other slurry constituents are similar. In the low to the intermediate shear region ($0 \text{ s}^{-1} - 175 \text{ s}^{-1}$), the greater viscosity observed in slurry B can be attributed to the influence of its irregular particle shape. The large surface area resulting from the irregularity in shape results in more points of contact and stronger interparticle interaction than the regularly shaped particles of slurry A, which have a weaker interparticle interaction due to their low

specific surface area, thus, less interaction with the dispersion medium. Additionally, due to the difference in shape, the stronger interparticle forces in slurry B resulted in more significant shear stress needed to deform it than in slurry A.

As the shear rate increases, the alignment of some polymer and particle molecules in the direction of the shear causes a progressive decrease in viscosity.

In the intermediate to the high shear regime (175 s^{-1} to 500 s^{-1}), the slurries exhibit more pronounced shear thinning behavior characterized by a continuous decrease in viscosity and deformation stress. This behavior is due to the further breakdown of substructures held together by weak dispersion forces, which can be broken down at increasing shear rates. The breakdown results in the release of binder molecules trapped within the substructures, reducing viscosity. The decrease in viscosity is a result of the increased binder concentration of the slurry (as seen in Figure 2.10), allowing the graphite particles to rotate more in alignment with the direction of the shear. Overall, at intermediate to high shear rates, the behavior of the fluid is influenced by the hydrodynamic interaction of the rotating graphite particles [23], [70]. In addition, at intermediate to high shear rates (175 s^{-1} - 500 s^{-1}), the lower viscosity observed in slurry B can still be attributed to its irregular shape. The large surface area means more substructures containing entrapped binder molecules within large pores (due to a lower packing density) than slurry A. As the substructures break down, more binder molecules are released, making the slurry behave like it has a high binder concentration at high shear rates than slurry A, allowing the graphite particles to rotate easily in alignment with the shear direction. This implies a further reduction in the viscosity of slurry B than slurry A. The same shape difference reasoning applies to the flow curve. Upon the release of entrapped binders in slurry B, less stress is required to deform the slurry as the shear rate increases (shear stress independence on shear rate or typical plastic behaviour). In contrast, slurry A, with its high packing density due to its regular shape and small pores, can collide more easily at higher shear rates, leading to higher shear stress at increasing shear rates (shear stress dependence on shear rate) for deformation than slurry B.

$$\text{Shear rate } \dot{\gamma} = \frac{\text{velocity } dV (\text{ms}^{-1})}{\text{distance } dh (\text{m})} = \frac{\text{coating speed } dV (\text{ms}^{-1})}{\text{thickness of wet layer } dh (\text{m})}; \text{Unit } (\text{s}^{-1}) \quad (\text{Eqn. 3.1})$$

In addition to flow and viscosity measurements, a thixotropic evaluation was also conducted to determine the extent of recovery after the different slurries were sheared. The shear rates used in the evaluation were calculated based on equation 3.1 provided, using the coating parameters for this study as listed in Table 3.5. A shear rate of 15 s^{-1} was selected as it is relevant to the coating rates used in this study. The other two shear rates (50 s^{-1} and 100 s^{-1}) are out of the reasonable range; however, they provided an understanding of what may happen if the coating speed parameters were changed, for example, if the shear rate is increased due to a faster coating speed, or if the slurry thickness is altered.

Table 3.5: Tape Casting coating parameters and calculated shear rates

<i>Coating velocity (m/s)</i>	<i>Gap thickness (μm)</i>	<i>Approximate shear rate (s⁻¹)</i>
0.003	200	15
0.003	500	6
0.005	500	10

The thixotropy behavior of Slurry A and Slurry B is visually represented in Figure 3.11, which illustrates the time-dependency of the slurries and simulates the behaviour of the slurries before, during, and after shearing.

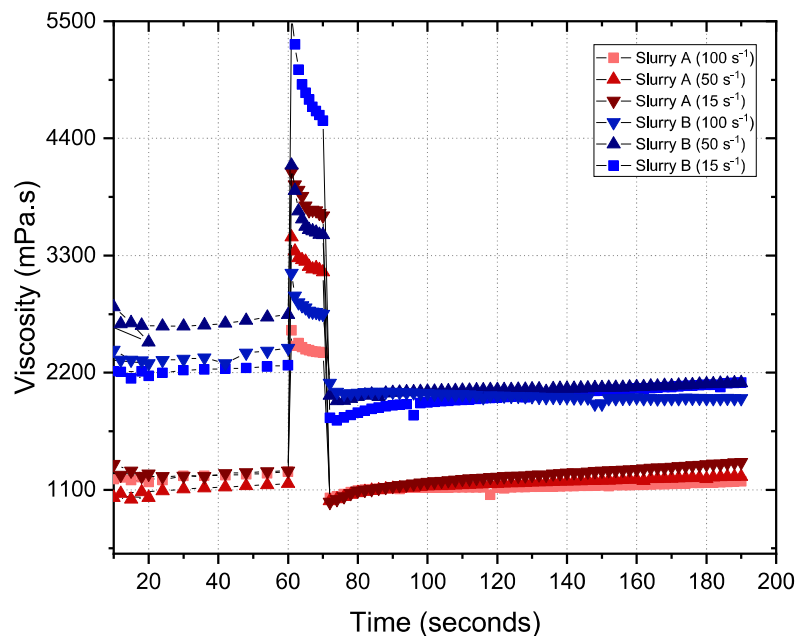


Figure 3.11: Thixotropic behaviour of slurry A and slurry B.

The viscosity values of slurry A are consistently lower than those of slurry B across all the shear rates (15 s^{-1} , 50 s^{-1} , and 100 s^{-1}) that were considered. Additionally, the viscosity values in the first and third intervals are observed to be lower than the viscosity measured for the second interval.

In the first interval (time range: 0 - 60 seconds), the slurry is in a state of rest or nearly stationary as the applied shear rate insufficient to alter the position of the resting molecules in the slurry. As a result, the slurry behaves like a solid of undisturbed molecules. The average viscosity value for slurry A and slurry B is similar to their initial viscosity values at the beginning of the shearing process in the viscosity curve (Figure 3.9b). The slight deviation in the starting point for each slurry at the start of this interval is related to differences in the timing of when the measurement resumed after the slurries were fed in between the measuring plates of the instrument.

In interval 2 (time range: 60 seconds – 72 seconds), the slurries were tested at different shear rates of 15 s⁻¹, 50 s⁻¹, and 100 s⁻¹. Both slurries exhibited an increase in viscosity, but slurry B has higher viscosity values than slurry A. The shear-thickening behavior observed in this second interval can be explained by the discussion of the low shear rate region in the viscosity curve (Figure 3.9b), as the shear rates considered for thixotropy fall within the range of 0 s⁻¹ to 100 s⁻¹. As previously observed in the viscosity curve, a shear rate of 15 s⁻¹ falls within the range of intense shear-thickening behavior, thus it is not surprising that it has the highest viscosity value in the second interval of the thixotropy test, compared to the moderate viscosity values at 50 s⁻¹ and low viscosity value at 100 s⁻¹. The shear rates can be thought of as the slurry's degree of spread or deformation. A low shear rate leads to more accidental particle collisions and entanglement of the polymer chains but less alignment. Therefore, while the 15 s⁻¹ shear rate may cause a disturbance or collision of the resting molecules, it is not enough to cause significant alignment of particles and polymer chains within the duration. Similarly, the 50 s⁻¹ shear rate causes moderate alignment of particles and polymer chains within the duration. The 100 s⁻¹ shear rate causes a significant alignment of particles and polymer chains within the duration, resulting in a lesser viscosity value than the other shear rates.

Of particular interest is the recovery of the slurries when the shearing force is halted, which is simulated in region 3 (time range: 72 seconds to 195 seconds). In this region, the slurries' structural recovery is observed for approximately 125 seconds after shearing. This means that for the 15 s⁻¹, only a few molecules need to return to a state of rest, whereas a higher shear rate of 100 s⁻¹ requires more molecules to return to rest within the 125-second duration. Although both slurries showed similar recovery in terms of viscosity, the recovery time can be attributed to the intensity of the shear rate and the composition of the slurries.

Thixotropic recovery time, which is shown in Table 3.6, is the amount of time it takes for a sample's viscosity to return to a specified percentage (80%) of its initial viscosity in the first interval. As a result of the differences in specific surface area (or shape), at a shear rate of 15 s⁻¹, Slurry A recovered its viscosity to approximately 1020.8 mPa.s (out of 1228 mPa.s) within 5 seconds, while Slurry B recovered its viscosity to about 1819.2 mPa.s (out of 2274 mPa.s) within 10 seconds.

$$\text{Thixotropic Index} = \frac{\text{low-shear rate viscosity}}{\text{high-shear rate viscosity}} \quad (\text{Eqn. 3.2})$$

Further on thixotropy recovery, the thixotropic index, which is the ratio of a material's viscosity at two different speeds, indicates its ability to retain its shape. It was calculated using equation 3.2, and the results are presented in Table 3.6. Although Slurry B has a high level of shear thickening, meaning it holds its shape well compared to Slurry A, its high thixotropic index means that its viscosity is more prone to decrease as agitation or shear stress increases. The findings about Slurry B's susceptibility to structural destruction at high shear stresses are supported by the discussion of its shear stress-shear rate

independence or plastic behavior at high shear rates (Figure 3.9). This means that as agitation or shear stress increases, Slurry B's viscosity will decrease.

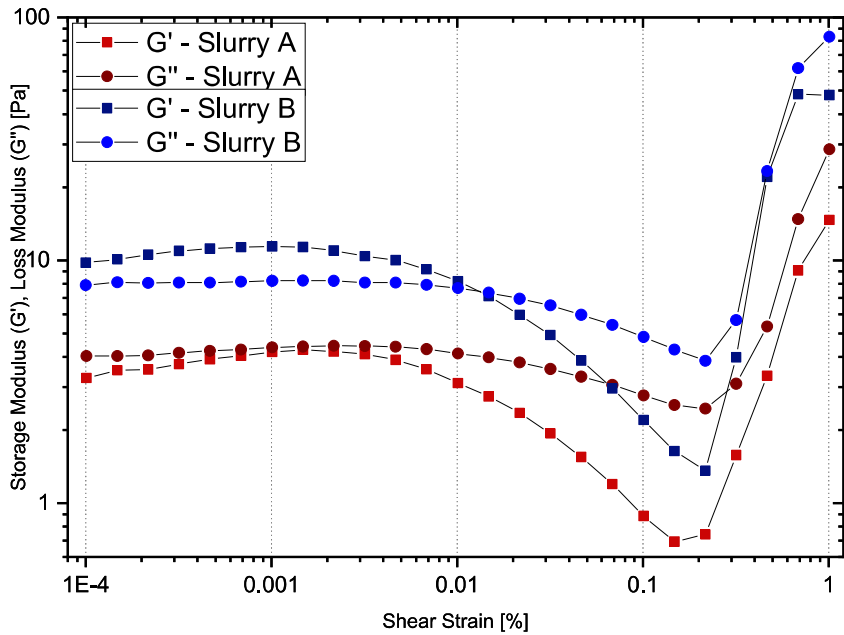
In summary, the viscosity of slurry B is consistently higher than that of slurry A at all shear rates due to the shape differences of the graphite particles used in each slurry. Both slurries exhibit thixotropic behavior, meaning their microstructure has a time-dependent response to changes in applied shear rate. However, slurry B's thixotropic behavior is more pronounced due to the irregular shape and increased interactions of its graphite particles. The many contact points of the Type B graphite particles in slurry B result in slower structural recovery of the viscosity when compared to Slurry A. The thixotropic index confirms that Slurry B show a more pronounced response to changes in shear rate. This suggests that while Slurry B exhibits stronger shear-thickening properties, it may also exhibit greater shear-thinning properties than Slurry A at high shear rates.

Table 3.6: Summary of thixotropic index

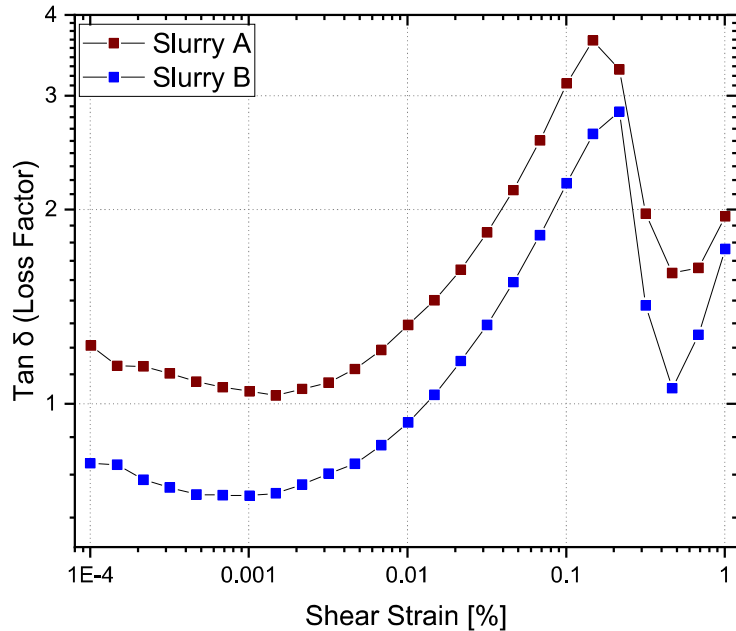
Thixotropic Parameters	Slurry A	Slurry B
Thixotropy Viscosity at: 15 s^{-1} (mPa.s)	4059	5460
	2568	3102
Thixotropic Index: (15 s-1:100 s-1)	1.58	1.76
Thixotropic recovery time at 80% (seconds)	5	10

The thixotropic test provided insight into the degree of shear thickening, structural recovery or susceptibility to structural degradation. The dynamic and viscoelasticity tests offer more information on the slurries' viscoelasticity levels and shelf life. The amplitude sweep test in Figure 3.12 illustrates the moduli and loss factor of slurry A (in red) and slurry B (in blue) as the amplitude of deformation was varied while keeping the frequency of deformation (that is, the preset shear stress) constant.

The amplitude sweep measurement compared the moduli and loss factors of slurry A and B. The results showed that the storage modulus (G') and the loss modulus (G'') of slurry A were lower in magnitude than those of slurry B. The measurement gives the linear viscoelastic (LVE) region as a result. The point where the storage modulus and the loss modulus coincide around the shear strain 0.013 %, after which is the non-linear region where the structures get deformed. Based on these observations, it can be concluded that Slurry A is a viscoelastic liquid (because $G'' > G'$) and Slurry B is a viscoelastic solid ($G' > G''$). The behavior beyond the LVE region might be ascribed to the destruction of the network structure, strain hardening [18].



a)



b)

Figure 3.12: a) Storage modulus (G') and loss modulus (G'') of both slurries against shear strain b) Loss factor ($\tan \delta$) of both slurries against shear strain

The loss factor supports the conclusions from the amplitude sweep measurement. The loss factor of Slurry A is observed to be above unity irrespective of the shear strain, and that of Slurry B is below unity at the low shear strain range. At around 0.013 % shear rate (where G' and G'' coincide in Figure 3.17a), the loss factor of Slurry B increased beyond unity. This suggests that Slurry A has a higher

proportion of viscous behavior than elastic behavior, leading to more loss due to viscous heating and more shape change. In contrast, Slurry B has a higher proportion of elastic behavior than viscous behavior, resulting in less loss due to viscous heating and less shape change.

In conclusion, the amplitude sweeps revealed that Slurry A exhibits viscoelastic liquid behaviour even at low-stress amplitudes. This can be ascribed to the symmetrical shape of the molecules, which allows them to rotate and spread easily. The high level of viscous heating in Slurry A is due to the high packing density of the molecules, which increases the frictional force of the colliding and rotating molecules and leads to energy loss and consequent liquidity. On the other hand, the amplitude sweep tests showed that Slurry B exhibits viscoelastic-solid behaviour due to the asymmetrical shape of the particles and their high surface area, which strongly aids the formation of a firm network structure due to the strong binder-carbon black domain connecting the graphite particle strongly [24]. The low packing density of the molecules allows them more space to rotate, reducing the frictional force between the particles and leading to less viscous heating and consequent solidity. This results in a higher storage modulus than loss modulus within the LVE region. Previous studies have also shown that the movement of particles within an aggregate contributes to the viscosity of the material, as seen in Slurry A. Additionally, the connection between aggregates plays a role in determining the material's stiffness, as observed in Slurry B. [24], [35].

In addition to the dynamic tests, the graph in Figure 3.13 illustrates the moduli and the loss factor of slurry A and slurry B, as determined by a test that changed the frequency of deformation while maintaining a constant amplitude of deformation (or preset shear stress). This measurement provides a clearer understanding of the stability of the slurries over time (shelf life).

At very low frequencies, both slurry A and slurry B, which are a viscoelastic liquid and a viscoelastic solid, respectively, behave like solids or gels in the absence of any disturbance. Also, the storage modulus of both slurries is greater in value than their respective loss modulus. As the frequency increases in the low- to the intermediate-frequency range, the storage and loss moduli of the two slurries responded similarly with a decreasing storage modulus and an increasing loss modulus. The fact that $G' > G''$ implies a rigidity or reversible deformation at low to intermediate frequencies can be attributed to the minimal disturbance of the resting molecules, indicating a low impact of shear stress/force at these frequencies.

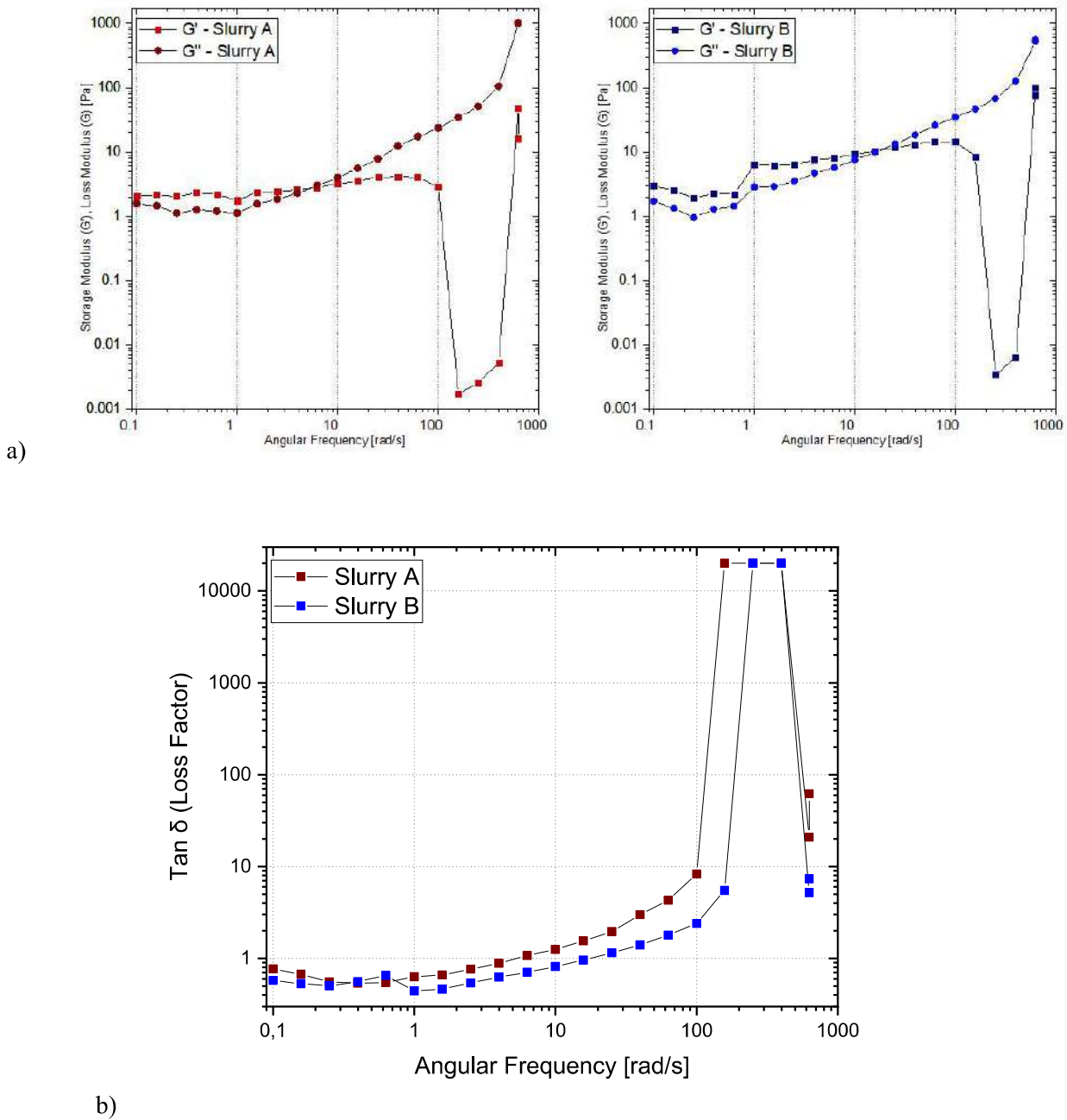


Figure 3.13: a) Frequency sweep of slurry A and slurry B, b) Loss factor ($\tan \delta$) of both slurries against angular frequencies.

In the intermediate-frequency region, specific points unique to each slurry are observed where the storage and loss modulus cross over each other, resulting in the loss modulus becoming greater in magnitude than the storage modulus. This crossover point, which marks the transition from solid-like to liquid-like behavior, occurs at approximately 5.2 rad/s for slurry A and 17.9 rad/s for slurry B. The difference in crossover frequency suggests that slurry B is more stable than slurry A. This difference can be attributed to the many points of contact (due to the larger surface area) for stabilizing forces to act on in slurry B.

At high frequencies, G'' is greater than G' , indicating that the slurries behave more like liquids. This is because the molecules of both slurries are greatly disturbed by more frequent collisions and energy loss, causing the slurries to behave like viscous liquids. The G' curves for both slurries reach a minimum at higher frequencies, indicating that the samples have a weak structure network or experience a structural breakdown. The structural breakdown becomes more prominent as the frequency increases. The instability at intermediate to high frequencies can be attributed to the high disturbance of the molecules caused by the high impact of shear stress/force at high frequencies.

The $\tan \delta$ value, which is a measure of the ratio of loss modulus to storage modulus, can also be used to identify changes in the structure of the slurry. A $\tan \delta$ value below 1 indicates a low binder concentration and a gel structure formed by the graphite particles due to low binder/CMC concentration. As the CMC concentration is increased, due to the breakdown of substructures at sufficient oscillation frequencies, the $\tan \delta$ value increased beyond unity (1) at the respective crossover points of 5.2 rad/s for Slurry A and 17.9 rad/s for Slurry B. Beyond the crossover point, it remains above 1 until a critical concentration is reached, at which it starts to decrease to values below 1. This critical concentration is the point at which the liquid-like behavior of the slurry changes to a solid-like behavior. The network structure formed at this stage is made up of CMC molecules, with the graphite particles trapped or embedded within it.

In conclusion, at low frequencies, both slurries exhibit a behavior typical of particulate systems that form gel structures. The storage modulus is larger than the loss modulus and remains nearly constant. This can be attributed to the formation of gel structures by the graphite particles, which tend to aggregate in an aqueous solution due to their hydrophobicity. However, at high frequencies, where G'' is larger than G' and the moduli depend on the frequency, it indicates that the gel structure in the slurry no longer exists and has changed into a liquid-like structure due to the dispersion of the graphite particles. This study demonstrates that the stability and flowability of the slurry can be greatly impacted by variations in the morphology or features of the materials [14].

In summary of the rheological evaluation, it is essential to evaluate the flow and viscosity of a slurry over a wide range of shear rates to determine its stability and processability. This information is crucial for predicting the slurry's behavior and determining its suitability for coating applications. An ideal slurry should have low viscosity at high shear rates for smooth and consistent coating on the substrate while maintaining high viscosity at low shear rates for stability. This is particularly important for coating methods such as roll-to-roll or doctor blade coating, which usually occur at shear rates ranging from several hundred to several thousand reciprocal seconds [5], [16]. The thixotropic behavior of a slurry also significantly affects the coating and drying process of the electrode. If the formulation takes longer to recover its structure or viscosity, it may be more prone to phase separation, precipitation, or settling, resulting in a lower-quality electrode.

Given the established differences between the two slurries, where Slurry A, with its low BET specific surface area, exhibits characteristics of a viscoelastic liquid with lower viscosity and shorter shelf-life, while Slurry B, with its high BET specific surface area, behaves like a viscoelastic solid with higher viscosity and a longer shelf-life, it is likely that these rheological variations will have a significant impact on the properties of the final electrode after coating. In the subsequent section, we will investigate the anode produced from these distinct slurries.

3.3 ELECTRODE ANALYSIS

This section explains the procedures used to evaluate the impact of the two different slurries on the characteristics of thick aqueous graphite anodes. The findings and interpretation are drawn from the data obtained through the conducted experiments.

3.3.1 COATING

The slurries were coated onto the current collectors using a doctor blade coater, as shown in Figure 3.14. A glass slide was placed on the coater to prevent equipment contamination and allow the slurries to be cast onto 11 µm thick copper foils (Carl Schlenk AG). Single-layer and bilayer anodes were coated based on different designs. For the single-layer samples, a conventional film layering method was used, coating a single layer of slurry paste on one side of the copper substrate to achieve the desired wet thickness by adjusting the gap size of the knife on the doctor blade coater to 500 µm. In the case of multi-layer coating, a two-step process was employed. The first step involved coating the slurry paste onto one side of the copper substrate current collector with a wet gap thickness of 200 µm (as the bottom layer) at 60 °C. After the first layer was deposited, it was left to cool down to room temperature before the second layer was coated on top. The second layer was dried at room temperature, which allowed slow evaporation of solvent from the top of the coating and gentle flow of the binder for good adhesion of the layers, resulting in the production of defect-free electrodes. The coating speed for both layers was 3 mm/s.



Figure 3.14: Lab-scale doctor blade coater

After the coating process, the as-fabricated sheet electrodes were dried in an oven at 80 °C for 12 hours under a vacuum to remove residual solvent.

3.3.2 POROSITY AND LOADING CALCULATIONS

After the drying step, small samples in the form of discs with a diameter of 16 mm were cut out from the fabricated anode sheets for testing (Figure 3.15).

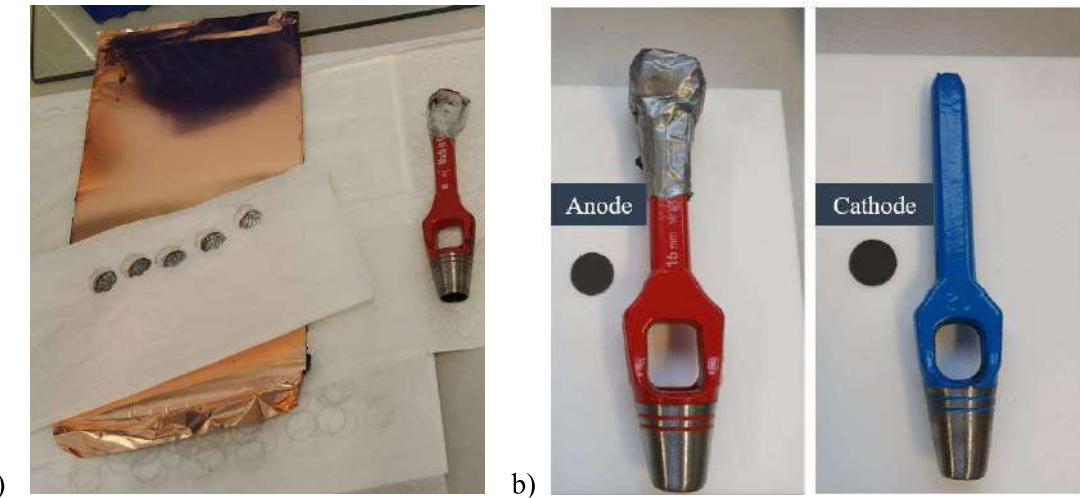


Figure 3.15: Punched electrode discs for coin-cells

The thickness and masses of the coin discs were recorded and subsequently used to calculate the porosity and loading of the single and multi-layer samples using equations 3.3 and 3.4 provided below.

Capacity equations: (Eqn. 3.3)

$$\text{Theoretical Capacity of AM (mAhg}^{-1}\text{)} = 340$$

$$\text{Electrode Capacity (mAh)} = \text{Capacity of AM (mAh/g)} * \text{Mass of AM(g)}$$

$$\text{Areal Capacity (mAh/cm}^2\text{)} = \frac{\text{Electrode Capacity (mAh)}}{\text{Area of coating (cm}^2\text{)}}$$

Porosity calculation: (Eqn. 3.4)

$$\text{Density of the coating, } \rho_c = \frac{\text{mass of the coating, } m_c}{\text{volume of the coating, } V_c}$$

$$\text{Sum of all bulk densities, } \rho_{ph} = \sum_i ((\text{fraction of coating (} p_i \text{)} * \text{bulk density (} \rho_i \text{)})$$

$$\text{Porosity, } \epsilon = 1 - \frac{\rho_c}{\rho_{ph}}$$

The relationship between the wet thickness, the dry thickness, the dry mass, and the areal loading was then compared for the two different coatings, Anode A and Anode B.

3.3.3 MECHANICAL INTEGRITY

The surface topography and cross-sectional imaging of the electrode samples were carried out using a digital microscope (VHX7000, Keyence Corporation, Osaka, Japan) to assess coating homogeneity and examine inter-layer transitions in the multi-layered electrodes. Additionally, the adhesion strength of

the coating to the current collector foil was characterized by visually inspecting the substrates after the coating was peeled off the substrate via a peel test.



Figure 3.16: Keyence Digital Microscope VHX 7000

The peel test was conducted by firmly pressing a double-sided scotch tape (3M 600) onto the sample plate of known width, followed by attaching the strips of anode facedown onto the tape, ensuring there were no air bubbles between the tape and the anode. A mechanical press setup (Figure 3.17a) was then used to apply similar pressure to each sample. The sample holder was then placed in the clamp of the peel tester (Figure 3.17b), and the free end of the current collector (or of the strip) was attached to the movable end of the instrument. The tape was peeled at an angle of 180° from the film at a speed of 20 mm/s until the foil was utterly detached. The load cell measured the force required to peel the tape [52].

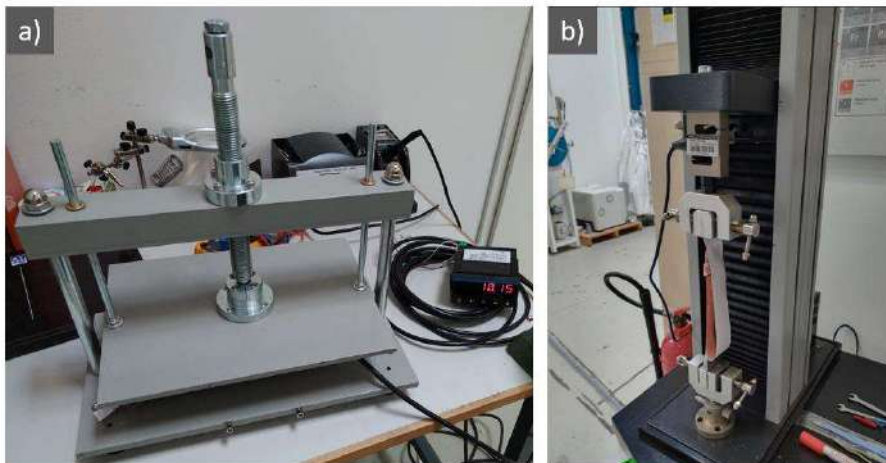


Figure 3.17: Setup a) Press b) Peel tester

3.3.4 RESULT AND DISCUSSION ON ELECTRODE PROPERTIES

Figure 3.18a displays images of defective thick anodes before the implementing different formulations, and specific mixing sequences, understanding the rheological properties and adjusting the coating parameters for the multilayer approach. On the other hand, Figure 3.18b shows defect-free anode sheets that were produced after considering the factors mentioned earlier. The coating process resulted in

anode sheets of single and multilayers and each with either or both slurry formulations. They all (Figure 3.18b) have a homogeneous surface that indicates a uniform distribution of all materials; that is, examining the surface of each coating, a continuous film without defects of any kind was fabricated (compared to Figure 1.4). Even before calendaring, both samples have a smooth and homogeneous surface. This is a significant improvement considering the high thickness and aqueous processing of the electrode [7].



a)



b)

Figure 3.18: Comparison of a) initially defective- and b) defect-free-thick aqueous anodes.

Comparing the before (Figure 3. 18a) and after images (Figure 3.18b) of the developed anodes demonstrates the vitality of suitable slurry formulations, mixing sequence, prior testing and analysis. To achieve a thick defect-free graphite anode, it is essential to consider fine-tuned coating parameters and use a multilayer approach to prevent the formation of pinholes, agglomerates, crates, and delamination, among other challenges.

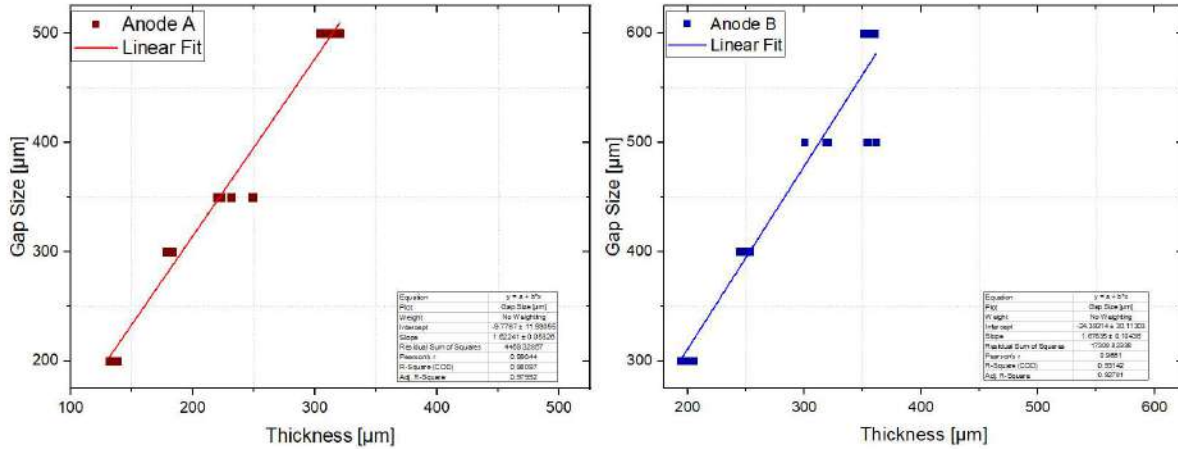


Figure 3.19: Correlation of slurry gap size vs electrode thickness

Figure 3.19 illustrates the correlation between the wet and dry thickness of single-layer (SL) electrodes. It is observed that the dry thickness is generally less than the wet thickness, which is a typical occurrence due to the evaporation of the solvent. Moreover, a linear correlation is observed between the wet and dry thickness, as shown by the linear fittings in equations 3.5 and 3.6 for Anode A and Anode B, respectively. It should be noted, however, that the linearity is only an approximation, as not all data points may fall within the linear range due to variations in gap size and drying rates.

The slopes of the fittings are comparable, but the intercepts differ greatly between Electrode A and Electrode B. This means that, in general, a larger wet gap size (y) is required for Electrode B to achieve a similar actual dry thickness (x) as Electrode A. These plots and fittings are crucial as they assist in determining the quantity of slurry required to attain a specific dry thickness (x) based on a specified wet gap size (y).

$$\text{Electrode A: } y = 1.6224x - 9.7767 \quad (\text{Eqn. 3.5})$$

$$\text{Electrode B: } y = 1.6763x - 24.393 \quad (\text{Eqn. 3.6})$$

Interestingly, the high thicknesses did not correspond to higher masses. Electrode A has higher masses than Electrode B, as shown in Figure 3.20 by the red and blue square symbols. This can be explained by the irregular shape of the particles of graphite B resulting in a high pore volume, even after the removal of solvents. This high pore volume or low packing density contributes to an electrode structure of higher thickness than mass. The irregular shape of the particles in Electrode B is responsible for the large pore size and, thus, higher thickness. This could also be linked to rheology as good thickness accuracy is an attribute of the shear thickening behavior of Slurry B at the low shear region, which is relatively higher than that of Electrode A [22].

It was anticipated that there would be a significant difference in loading due to Electrode A having a higher mass than Electrode B. However, it was found that the capacity of the two electrodes is almost

identical. This can be attributed to the fact that the particle sizes of the active materials (graphites) are similar, as shown by the CILAS analysis.

To summarize, the evaluation of the electrode properties using single-layer electrodes of the two distinct electrodes shows that while Electrode A has a higher mass, lower thickness and porosity, Electrode B has a lower mass, higher thickness and porosity, and their loading is comparable. The difference in porosity between the single-layer Electrode A and Electrode B is evident in Table 3.7 and is attributed to differences in packing density or resulting pore size/volume.

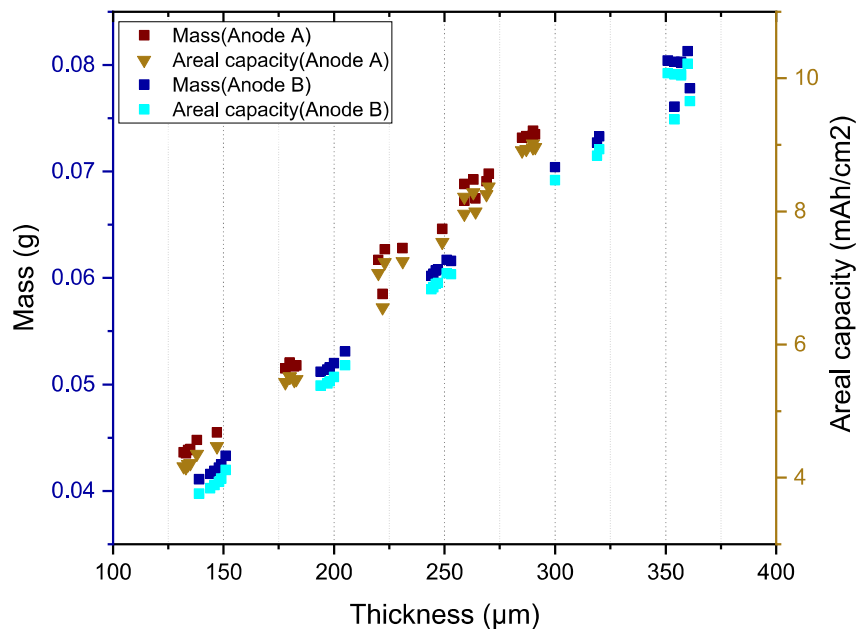


Figure 3.20: Correlation of Mass, thickness, and areal capacity.

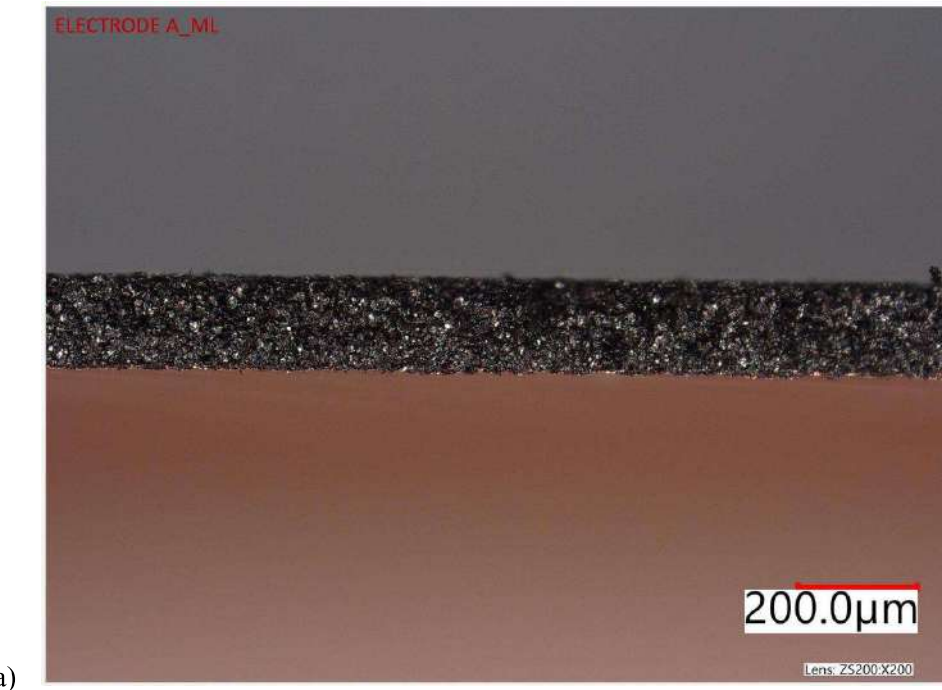
Furthermore, the analysis of the masses and thicknesses of the multi-layer electrodes revealed that the porosity of the 200 μm bottom layer was slightly less than that of the thick single-layer and multi-layer configurations (as displayed in Table 3.7). Despite having a higher mass, the thick multi-layer (ML) electrodes have comparable porosity to single-layer electrodes.

The comparable average porosity in the multi-layer configuration can be attributed to interpenetrating layers during the coating process, leading to a higher mass than single layers. This is because the liquid slurry seeps into the rigid bottom layer, slightly filling the pores and forming an interpenetrating layer. This flow into the pores slightly changes the pore size and greatly reduces the amount required to attain the same loading. On the other hand, single-layer anodes do not have interpenetrating layers, thus requiring less slurry and resulting in a lower mass. Despite similar porosity values between the multilayers and single layers, the interpenetration of layers in multi-layer configurations provides stronger interlayer adhesion.

Table 3.7: Summary of the porosity and areal loading.

Electrode Type	Electrode	Porosity	Anode Areal Capacity	Cathode Areal Capacity
	Layers	[%]	[mA h/cm²]	[mA h/cm²]
<i>Electrode A</i>	Single-layer	55 ± 0.3	9.5 ± 0.1	8.6 ± 0.1
	Multi-layer	54 ± 0.1	9.5 ± 0.3	8.6 ± 0.1
	Bottom-layer	54 ± 0.2	4.2 ± 0.1	8.6 ± 0.1
<i>Electrode B</i>	Single-layer	60 ± 0.1	9.05 ± 0.1	8.6 ± 0.1

Figure 3.21 demonstrates the mechanical integrity results, which align with the prior discussion on the effect of graphite particle shape on electrode mass, loading, and thickness. The absence of a clear separation interface between the two layers in multi-layer electrodes A and B is noteworthy. Figures 3.21a and 3.21b show that Electrode A_{ML} in multi-layer form is thinner than Electrode B_{ML}, reinforcing the earlier findings about their single-layer thickness difference due to differences in packing density and pore size/volume. Furthermore, single-layer electrodes have a higher thickness than the multi-layer, as shown in the comparison of Figures 3.21b and 3.21c. The cross-section image displays that both single and multi-layer electrodes have a uniform thickness without a visible interface between the layers of the multi-layer anodes.



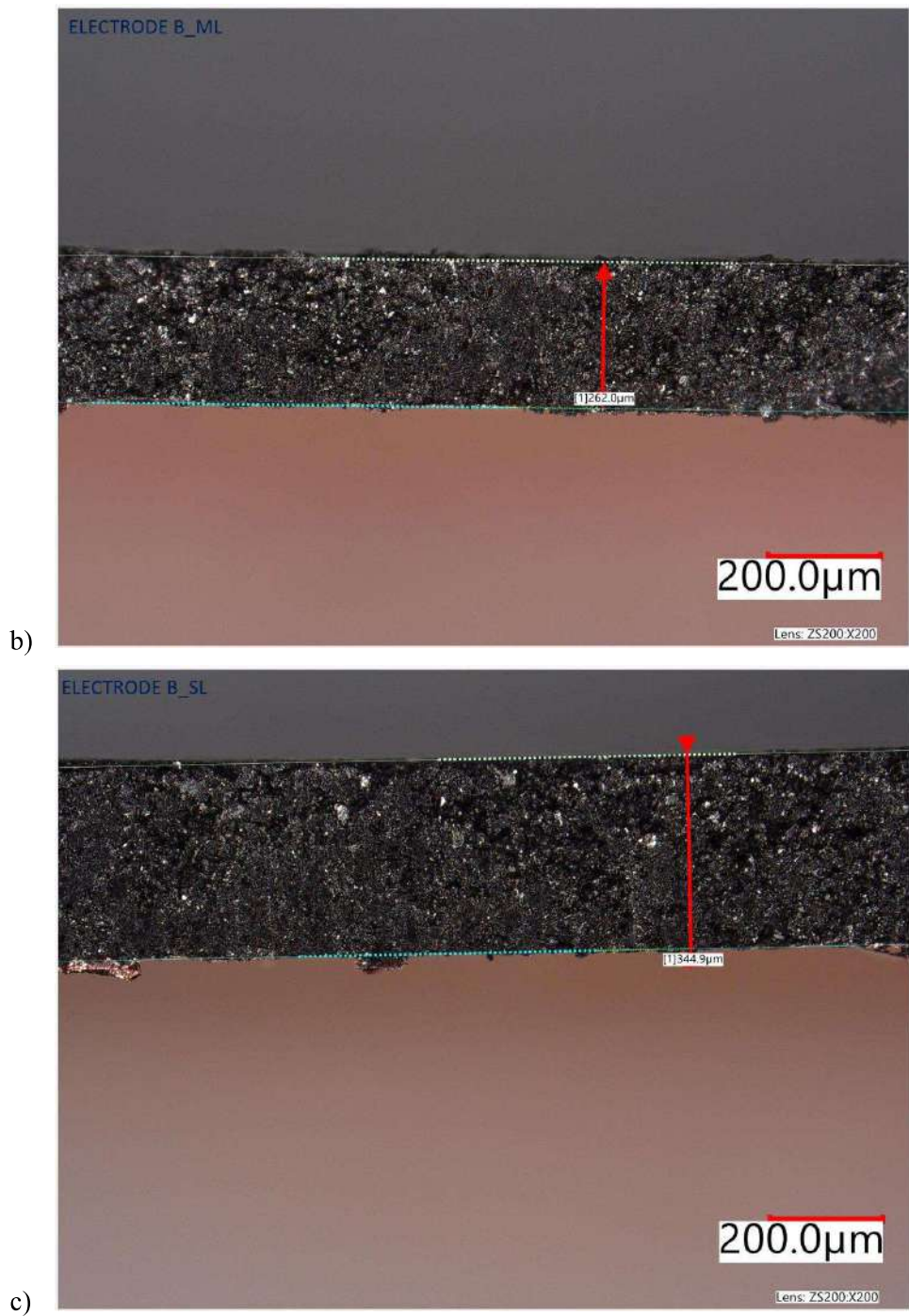
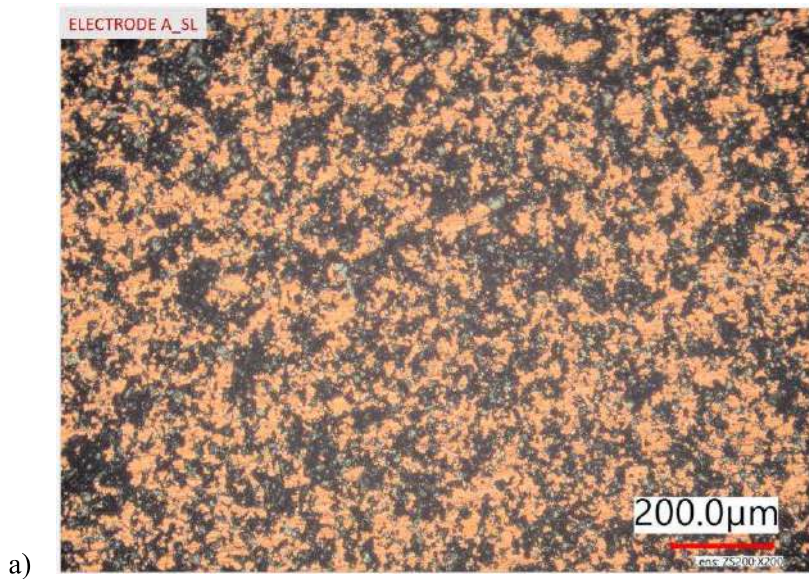


Figure 3.21: Micrograph comparing the cross-section of a) Electrode A_ML, b) Electrode B_ML, c) Electrode B_SL

Additionally, the peel test was used to evaluate the mechanical stability of the anodes with a known force and analyzed with a digital microscope. Figures 3.22a and 3.22b show the results of the peel test. While the exact adhesion force can not be quantified due to the ease of peeling off the electrode from the substrate, the amount of material left on the current collector can be used as a gauge of adhesion strength. More of the current collector surface of the ML than SL is covered with the coating at the same content of carbon black, which leads to a higher ratio of adhesion regions to the Copper region in Figure 3.22b. This implies that multi-layer electrodes exhibit stronger adhesion to the current collector

than single-layer electrodes because they have more points of contact on the collector. Adhesion also depends on the mixing sequence, as using a lower proportion of carbon black (CB) compared to the total binder (CMC/SBR) concentration results in low adhesion due to high polymer (binder) from non-uniformly embedded CB particles, according to Hu et al. [27]. However, in contrast to the dependence of mechanical strength and electrode flexibility on composition [52], in this study, the mixing sequence and the multilayer approach enhanced the bonding of more polymer-CB islands (from both layers) onto the current collectors of the ML anodes.

Although the mixing sequence impacts adhesion, the multilayer approach enhances bonding by providing more binder solutions, thus improving interlayer and electrode-current-collector adhesion. Therefore, this section also highlights the significance of multilayer and the optimization of coating and drying parameters, which improve the flow of the binder during the multilayer coating process and result in enhanced mechanical integrity.



a)

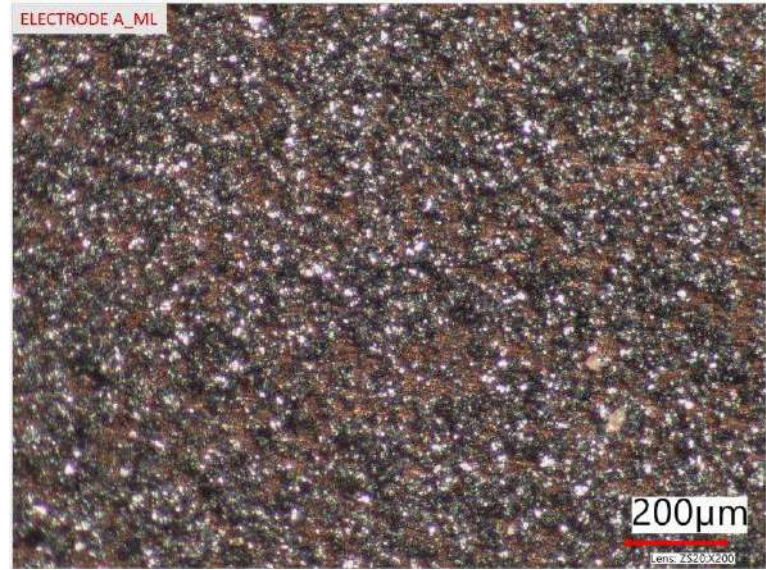


Figure 3.22: Micrographs of peeled SL and ML of Electrode A

3.3.5 CALENDARING

Subsequently, in preparation for the cell assembly, the anodes and cathodes were then rolled and compressed using a hot press machine. The process aimed to achieve a consistent thickness of 38 % for the anodes and 40 % for the cathodes to reduce internal resistance and increase surface area for charge transfer. The process, called calendaring, also improved the electrodes' flexibility and resistance to cracking, as shown in Figure 3.23.

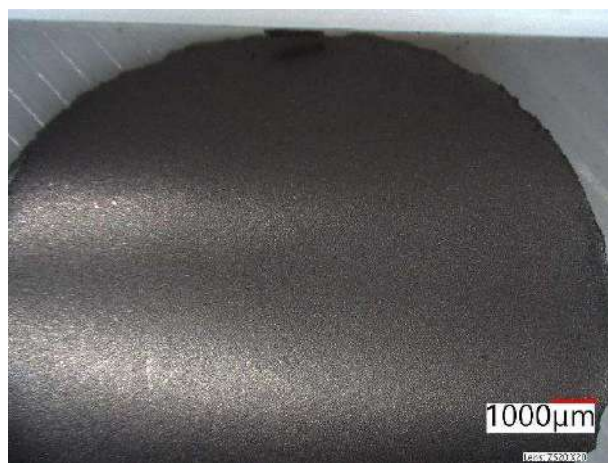


Figure 3.23: Calendared anode

3.4 ELECTROCHEMICAL ANALYSIS

3.4.1 CELL ASSEMBLY

All electrochemical tests were performed in a coin cell configuration, and the selected casing components, including 2032 coin cell (CR2032) stainless steel casing, 1.1 mm springs, and 1.5 mm spacers, were cleaned with ethanol in an ultrasonic bath for 15 minutes and dried in a Buchi at 60 °C for 1 hour before use.

The cathodes were prepared using similar methods as anodes and had a capacity of 8.6 mAh cm^{-2} , as reported by Neidhart et al. (2022) [7]. Single-layer and multilayer anodes were chosen for their capacity of 9.3 mAh cm^{-2} , all with an N/P ratio of approximately 1.1, taking into account both cathodes and anodes. The selected electrode samples (cathode and anode) for full coin cells were also dried under vacuum for 12 hours at 80°C overnight to eliminate any remaining moisture or solvent.

They were then transferred into a glovebox (MB200-G, MBRAUN, Garching, Germany) filled with argon gas (with $\text{O}_2 < 0.1 \text{ ppm}$, $\text{H}_2\text{O} < 0.1 \text{ ppm}$). Inside the glovebox, the necessary casing accessories and a Celgard 2500 separator were selected. The liquid electrolyte used for the cell configurations was a 1.2 M LiPF₆ in a 3:7 weight ratio mixture of ethylene carbonate (EC) and ethyl methyl carbonate (EMC).

The assembly sequence (Figure 3.24) involved placing the negative casing, then the spring, followed by the spacer, and then the anode facing up, with a few drops of electrolyte added from a pipette. Next, the Celgard 2500 separator was placed, and the remaining electrolyte was added (about 150 μL of electrolyte was added using the pipette) to secure the separator to the anode. Finally, the cathode was placed face down on the separator before the positive casing was placed to enclose all other components, and partially clamped down.

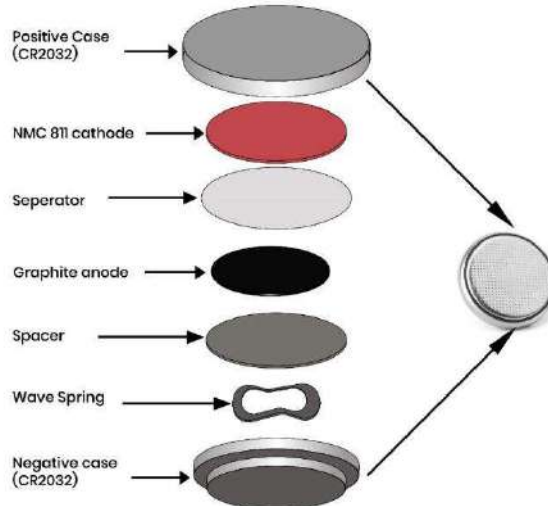


Figure 3.24: Full cell configuration [18]

The newly assembled coin cells were allowed to rest for about 120 seconds to allow the electrolyte to be fully absorbed before being crimped (using the MSK-110 Hydraulic Crimping Machine from M.T.I. Corporation, Richmond, CA) at 50 bar pressure to ensure proper sealing of the casing.

3.4.2 FULL CELL ELECTROCHEMICAL EVALUATION

After the cells were assembled, they were connected to a battery test station (Arbin BT-21084). The cycling process used was a constant current and constant voltage (CCCV) method, ranging from 3 V to

4.2 V. There were two formation cycles (at C/20 rate) and five preconditioning cycles (at C/10), which consisted of a sequence of: a 4 hour rest period after assembly, followed by a CC charge from 3.0 V to 4.2 V, a CV step at the voltage of 4.2 V, a 15-minute rest, and finally a CC discharge from 4.2 V to 3.0 V. The rate capability test procedure following the formation and preconditioning cycles with a starting capacity that was adjusted to the average of the five preconditioning (C/10) cycles. Additionally, it deviated from the formation and preconditioning procedures regarding the number of cycles per C-rate, as it spanned a loop of 10 cycles each of C/5, C/2, 1C, and C/10 C-rates. In total, the electrochemical test consisted of 47 cycles.

3.4.3 RESULTS AND DISCUSSION ON ELECTROCHEMICAL PROPERTIES

This provides a comprehensive comparison between the single layers, the single-layer and multilayer aqueous systems (as illustrated in Figure 3.25), as well as aqueous (water) and non-aqueous (NMP) solvents. Figure 3.26 clearly represents the lithium arrangement within the graphite structure from a top and side view perspective of the lithiation between the graphene layers of the graphite particles (Figure 3.28). All results and relevant factors are presented for a thorough understanding of the findings.

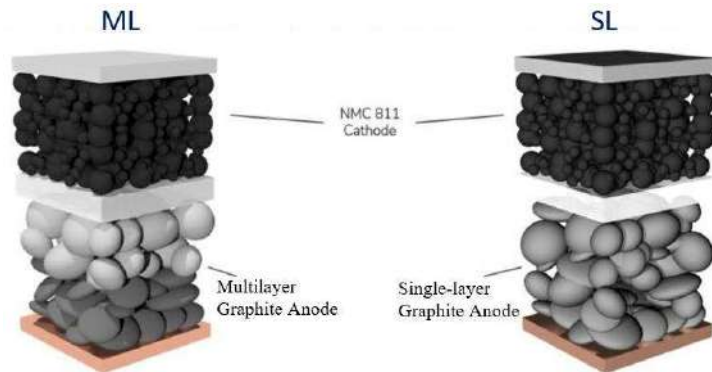


Figure 3.25: Illustration of Multilayer and single-layer cell configuration [61].

The best-performing electrode is chosen at each stage of comparison for further testing. Moreover, the capacity readings of the plots are obtained from the specific discharge capacity, which facilitates a clear observation of the anode's efficiency through the delithiation profiles during discharge. In this section, terms like "Cell A or Electrode A" and "Cell B or Electrode B" refer to the working anode produced from Type A graphite and Type B graphite, respectively.

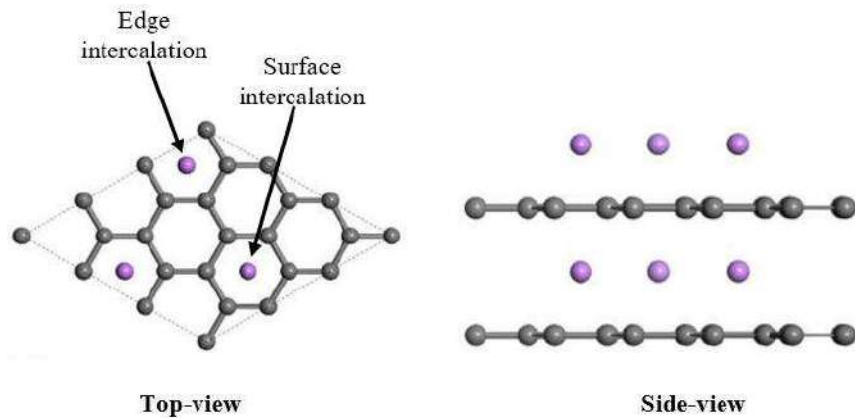


Figure 3.26: Top view and side view of intercalated graphite anode [71]

This illustration provides a visual representation of the state of the graphite-based anode after charging, highlighting the surface and edge parts available for lithiation. It also shows how to expect lithium ions to be removed during the discharge process from the edges and surface at different energy demands, as discussed in the next subsection.

3.4.3.1 SINGLE-LAYER ANODES

3.4.3.1.1 ANODE A VS ANODE B

The graph in Figure 3.27 shows the electrochemical performance results for cells made with single-layer anodes (SL) labeled as Electrode A and Electrode B; Cell A consists of Electrode A_SL as the anode, and Cell B is made up of Electrode B_SL as the anode.

During the first two charge/discharge cycles at the C/20 rate, the formation phase was established, and a homogeneous solid electrolyte interphase (SEI) passivation layer was formed. Table 3.8 showcase the recorded specific discharge capacity values at the start of formation and the start and end of preconditioning, respectively. By comparing the capacity of the first preconditioning cycle with that of the formation, about 4.01 mAhg^{-1} (2.23%) of irreversible capacity was recorded due to SEI formation in Electrode A_SL. Similarly, a loss of approximately 0.9 mAhg^{-1} (0.69%) of irreversible capacity was recorded in Electrode B_SL.

A homogeneous or smooth SEI formation at the end of cycle index 2 is due to the slow charge/discharge rate (C/20). This SEI formation caused an irreversible capacity loss, which can be explained by the electrolyte breakdown at both the anode and cathode interfaces, leading to a state of the overall cell (thermodynamic) equilibrium. The results suggest that Cell A experienced a higher irreversible capacity loss due to SEI formation compared to Cell B. Electrodes with a lower surface area are more susceptible to SEI formation as they have fewer points of interaction than electrodes with a larger surface area with more contact points. The inference is that the amount of SEI formed probably remains constant for the same material but depends on the surface area of the graphite. Also, according to Joho et al. (2001), the geometrical surface area of the graphite particle influences the SEI formation [72].

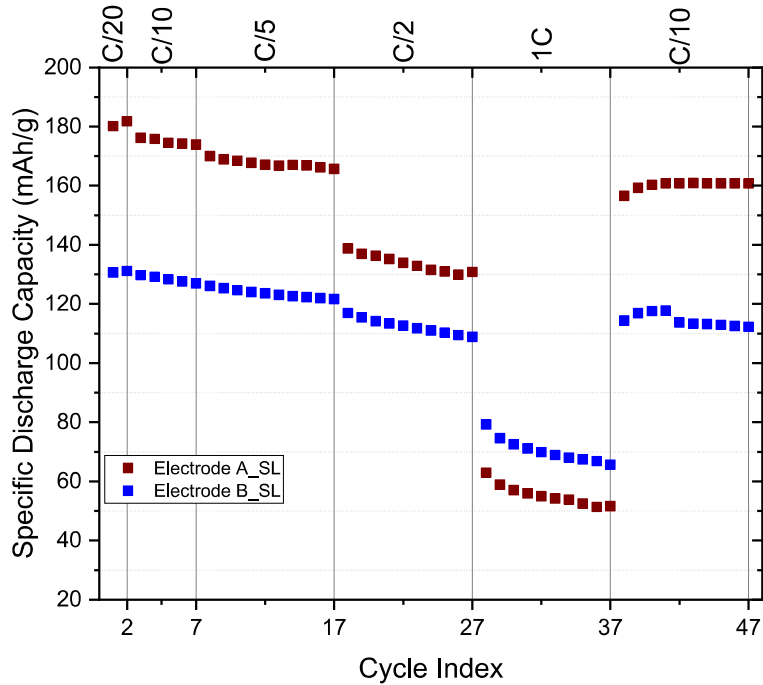


Figure 3.27: Single layer: Cell A vs Cell B

Further, at the end of preconditioning, Electrode A_{SL} lost approximately 1.27% and Electrode B_{SL} lost approximately 2.16% of its initial capacity at the start of preconditioning. In the rate capability phase, a general observation of the two different electrodes (Table 3.9) reveals that Electrode A_{SL} had a higher specific discharge capacity than Electrode B_{SL}. This difference is more pronounced at lower C-rates rather than the 1C-rate. However, at the 1C rate, equivalent to the highest applied current, Electrode A_{SL} and Electrode B_{SL} still showed lower specific discharge capacities, although Electrode B_{SL} performed better than Electrode A_{SL}. In the end, both SL cells had good overall performance and were able to recover about 80% of their capacity during the final C/10 rate cycles (capacity recovery phase), demonstrating good recovery from the previous fast charge at 1C.

Table 3.8: Formation and preconditioning data of aqueous cells

<i>sample</i>	<i>0.05C start</i>	<i>0.1C start</i>	<i>0.1C end</i>	<i>% difference (between 0.1C start and end)</i>
Cell/Electrode A _{SL}	180.15	176.14	173.91	1.27
Cell/Electrode B _{SL}	130.65	129.75	126.95	2.16
<i>Improvement [%] of Cell A vs. Cell B</i>	27.48	26.34	27	

Table 3.9: Rate capability data of aqueous cells

<i>sample</i>	<i>0.2C</i>	<i>0.5C</i>	<i>1C</i>	<i>0.1C</i>
---------------	-------------	-------------	-----------	-------------

	S	E	S	E	S	E	S	E
Cell A_SL	169.97	165.69	138.79	130.83	62.93	51.58	156.58	160.70
Cell B_SL	126.11	121.64	116.96	108.85	79.23	65.66	114.33	112.28
Improvement [%] of Cell A vs. Cell B	25.80	26.59	15.73	16.80	-25.90	-27.30	26.98	30.13

The comparison of Electrode A_SL and Electrode B_SL based on their reversible specific discharge capacity, as shown through the preconditioning and rate capability cycles, provides insight into their energy density and capacity retention. The variations in their performance, such as the more significant irreversible loss in Electrode A_SL and the higher energy density in Electrode A at low C-rates (C/20, C/10, C/5, C/2) and the higher specific discharge capacity in Electrode B at high current density (1C), can be attributed to differences in the morphologies of their graphite particles and the C-rates.

The surface area of the graphite particle in an anode affects the decomposition rate during SEI formation and the ability to store lithium ions (lithiation). A low BET specific surface area leads to higher decomposition. It is presumed that there is a higher decomposition because, for the same material (graphite), the amount of SEI formed remains nearly similar since the cathode material is identical. Therefore, more reactions are anticipated in graphite anodes with low SSA materials than those with high SSA. Also, a low BET SSA enhances lithiation at low C-rates because there is more time for the diffusion and migration of lithium ions. This is why the specific discharge capacity decreases as the C-rates increase from C/20 to C/2. Conversely, a high BET surface area with more contact points for interaction and larger pores, results in lower decomposition during SEI formation and better lithiation at high C-rates (1C). The presence of more active sites is likely the reason for the high specific capacity at 1C, despite lithium ions' faster diffusion and migration.

In summary, at lower C-rates, Anode A has a low number of active sites, which results in limited interaction with lithium ions and minimal side effects, leading to high specific discharge capacity. On the other hand, Anode B has more active sites, which can lead to more interaction between sites and increased side effects at low C-rates. However, at high C-rates, Anode B's larger surface area allows for better diffusion and migration of lithium ions, resulting in a higher specific discharge capacity than Anode A. This indicates that the large surface area of Anode B helps accommodate faster lithium ion migration and minimizes side effects at high current density.

3.4.3.1.2 ANODE A: WATER VS NMP

The comparison of single-layer anodes shown in Figure 3.28 highlights the effect of the two different solvents, water for aqueous electrodes and NMP for non-aqueous electrodes, on cell performance. The comparison between Electrode A_SL and Reference_SL provides insight into this influence.

Assuming a homogeneous SEI was formed after the first two cycles at the C/20 rate, Electrode A_SL and Reference_SL showed similar behavior, ending with higher irreversible specific discharge capacity than the first cycle. However, Electrode A_SL had a higher specific discharge capacity than Reference_SL.

The recorded specific discharge capacity values at the start of formation, preconditioning and the end of preconditioning can be seen in Table 3.10. Comparing the capacity after the SEI formation, Electrode A_SL lost 4.01 mAhg⁻¹ (2.23%) of irreversible capacity, while Reference_SL gained 7.73 mAhg⁻¹ (-5.83%) of irreversible capacity. The gain in capacity for Reference_SL can be attributed to non-smooth SEI formation, and suggests that the overall cell equilibrium was not reached yet. Since both electrodes are from the same active material, these results suggest that aqueous electrodes are less prone to side reactions during cycling than non-aqueous electrodes. In the case of non-aqueous electrodes, the microstructure of the active mass may have been modified to accommodate for side reactions during anode preparation, which could have influenced the results.

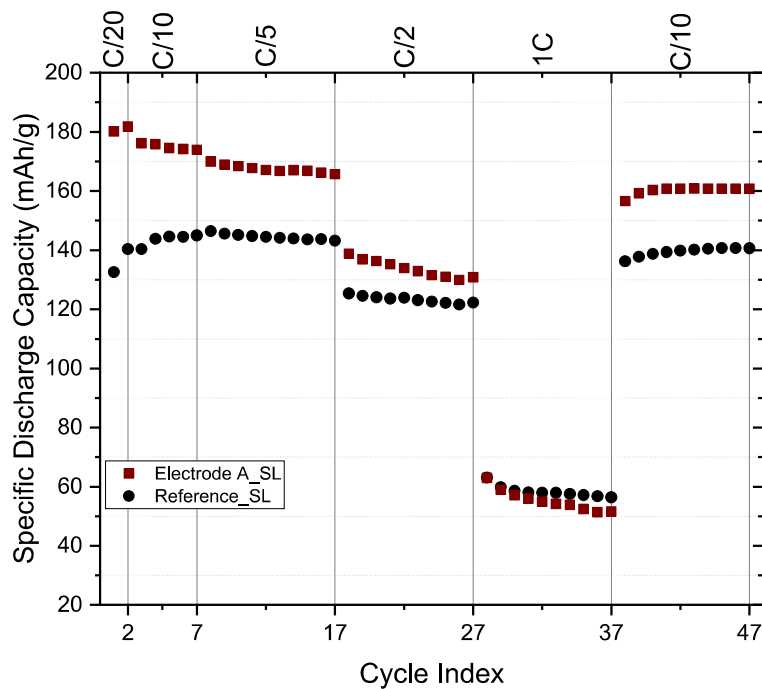


Figure 3.28: Single Layer: Aqueous (Cells A, Cell B) vs. Reference Cell

Further, at the end of preconditioning, Electrode A_SL lost about 1.27%, while Reference_SL gained about 3.32% of its initial capacity. During the rate capability test, it was observed that Electrode A_SL had a higher specific discharge capacity than Reference B_SL, particularly at low C-rates. Both Electrode A_SL and Reference_SL had similar capacities at the 1C rate. Ultimately, both single-layer cells demonstrated good performance, with a capacity recovery of about 80% during the final C/10 rate

after the fast charge at 1C. Also, the difference between the two cells became smaller as the C-rate increased.

Table 3.10: Formation and preconditioning data of aqueous and non-aqueous cells

<i>sample</i>	<i>0.05C start</i>	<i>0.1C start</i>	<i>0.1C end</i>	<i>% difference</i>
<i>Cell/Electrode A_SL</i>	180.15	176.14	173.91	1.27
<i>Reference_SL</i>	132.59	140.32	144.98	-3.32
<i>Improvement [%] of Cell A vs. Reference_SL</i>	26.40	20.34	16.64	

Table 3.11: Rate capability data of aqueous and non-aqueous cells

<i>sample</i>	<i>0.2C</i>		<i>0.5C</i>		<i>1C</i>		<i>0.1C</i>	
	<i>start</i>	<i>end</i>	<i>S</i>	<i>E</i>	<i>S</i>	<i>E</i>	<i>S</i>	<i>E</i>
<i>Cell A_SL</i>	169.97	165.69	138.79	130.83	62.93	51.58	156.58	160.70
<i>Reference_SL</i>	146.41	143.19	125.35	122.25	63.06	56.39	136.22	140.64
<i>Improvement [%] of Cell A vs. Reference_SL</i>	13.86	13.582	9.68	6.56	-0.21	-9.33	13.00	12.48

The performance difference between Electrode A_SL and Reference_SL is most apparent at low C-rates, with Electrode A_SL exhibiting a higher energy density. This disparity can be attributed to the microstructure and solvents used in their production. Although both electrodes were made from the same type of graphite (Type A), with identical BET SSA, the solvents used (water for the aqueous electrode and NMP for the non-aqueous electrode) led to distinct end morphologies and impacts on the overall cell performance. At high current densities, the similarities in performance can be attributed to fast diffusion, indicating that neither solvent favors lithiation at high C-rates. This subsection suggests that the result is intrinsic and only reflected in the structure of the anodes since the solvents were evaporated and not involved in the electrochemical reaction. However, a significant factor that could have influenced the result is the varying strength or capability of different microstructures to endure repeated cycling over time. The anode structure formed with water as the solvent appears superior in terms of mechanical stability and electrochemical performance compared to the structure formed with NMP as the solvent.

3.4.3.2 SINGLE-LAYERS VS MULTI-LAYER ANODES

The results of the comparison between single-layer and multi-layer cells made from the identical formulation F1 are displayed in Figure 3.29. The single-layer and multi-layer cells have comparable loading, even though the multi-layer consists of two layers of the same formulation. The comparison demonstrates the impact of multilayering, as both Electrode A_SL and Electrode A_ML are made of the same material composition or formulation.

Observations indicate that both Electrode A_SL and Electrode A_ML display similar behavior overall. The specific discharge capacity values recorded at the start of formation, preconditioning, and end of preconditioning can be seen in Table 3.12. Comparing the capacity after SEI formation (cycle no. 2), Electrode A_SL lost 2.23% (4.01 mAhg⁻¹) of its reversible capacity, while Electrode A_ML lost 2.89% (5.28 mAhg⁻¹) of its reversible capacity. The results suggest that Cell A_SL and Cell A_ML have almost similar irreversible capacity losses due to SEI formation, with the slight difference potentially attributed to an interface between the two layers in Cell A_ML.

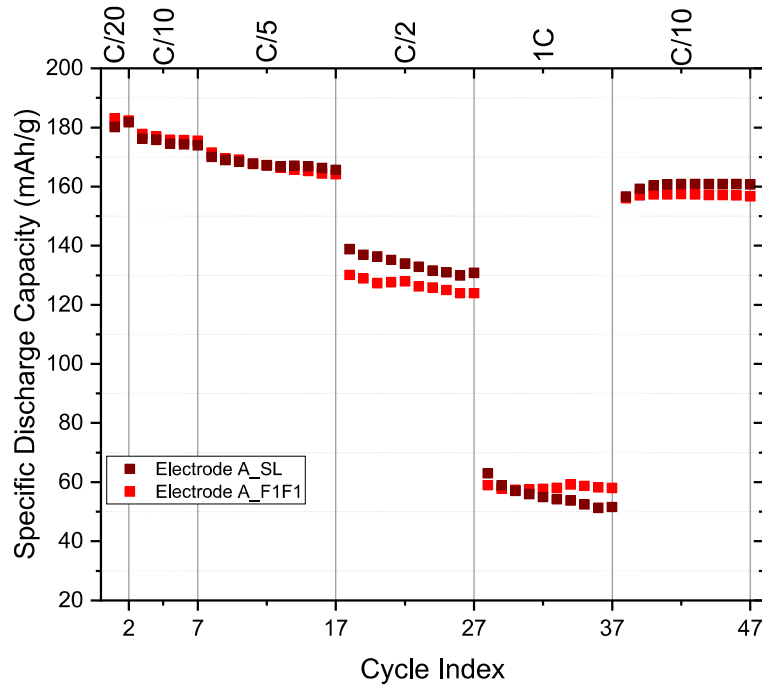


Figure 3.29: Single-layer vs multilayer of similar formulation (F1)

Furthermore, at the end of preconditioning, Electrode A_SL lost approximately 1.27%, and Electrode A_ML lost approximately 1.32% of its capacity (compared to the start of preconditioning). In the rate capability test, a general comparison of the two electrodes (as seen in Table 3.13) reveals that Electrode A_SL and Electrode A_ML exhibit a similarly higher specific discharge capacity at low current rates (C/20 to C/5). However, there is a slight difference at higher current densities, with Electrode A_SL having a slightly higher specific discharge capacity by an average of 6.15% at C/2 rate. Both electrodes behave similarly at a 1C rate. This suggests that the deviation is only evident at the C/2 rate, indicating that the two cells behave similarly at low current densities as the rate is sufficient to accommodate the diffusion and migration of lithium-ions. However, at the 1C rate, Electrode A_SL and Electrode A_ML exhibit lower specific discharge capacities. Ultimately, both cells display similar behavior, recovering about 80% of their capacity during the final C/10 rate cycles, demonstrating good recovery from the previous fast charge at 1C.

Table 3.12: Formation and preconditioning data of SL and ML cells

<i>sample</i>	<i>0.05C start</i>	<i>0.1C start</i>	<i>0.1C end</i>	<i>% difference</i>
<i>Cell/Electrode A_ML_F1F1</i>	183.04	177.76	175.42	1.32
<i>Cell/Electrode A_SL</i>	180.15	176.14	173.91	1.27
<i>Improvement [%] of Cell A: ML_F1F1 vs. SL</i>	1.58	0.91	0.86	

Table 3.13: Rate capability data of SL and ML cells

<i>sample</i>	<i>0.2C</i>		<i>0.5C</i>		<i>1C</i>		<i>0.1C</i>	
	<i>start</i>	<i>end</i>	<i>S</i>	<i>E</i>	<i>S</i>	<i>E</i>	<i>S</i>	<i>E</i>
<i>Cell/Electrode A_ML_F1F1</i>	171.4	164.1	130.1	123.9	58.9	58.1	155.9	156.7
<i>Cell/Electrode A_SL</i>	169.9	165.7	138.8	130.8	62.9	51.6	156.6	160.7
<i>Improvement [%] of Cell A: ML_F1F1 vs. SL</i>	0.85	-0.95	-6.69	-5.60	-6.68	11.18	-0.38	-2.55

The evaluation of Electrode A_SL and Electrode A_ML's reversible specific discharge capacity, as seen through the preconditioning and rate capability cycles, reveals a comparable energy density in both Electrode A_SL and Electrode A_ML at low C-rates (C/20, C/10, and C/5). The disparity in specific discharge capacity at C/2 and 1C rates is due to the distinct layering techniques used in each electrode.

The single layer does not impede the movement of lithium ions within the microstructure. However, even though the cross-section of the multi-layer appears to be homogeneous, there still exists an interpenetrating layer where the rigid bottom layer as-cast bonds with the slurry during the top layer coating. Although this interpenetrating effect is minimal at certain C-rates, at intermediate C-rates, the lithium ions may struggle to move quickly when they reach the interpenetrating interface, even though both layers have the same porosity (the same porosity as single layers) as they are both made from the same slurry formulation. In conclusion, the multilayering approach improves the mechanical stability of the anode structure (as demonstrated by the stability of the capacity in the ML compared to the SL). However, in electrochemical behavior, it maintains performance based on the formulations.

3.4.3.3 MULTI-LAYER ANODES

Further, to gain a deeper understanding of the effect of layering on cell performance, another multilayer cell was produced, the F1F2 cell, with a bottom layer of 200 μm and a top layer of 300 μm . This complements the previously discussed Electrode A_ML_F1F1, which consisted of two layers from the F1 formulation with a bottom layer of 200 μm and a top layer of 300 μm .

The comparison between multi-layer cells F1F1 and F1F2, with bottom layers from the identical formulation F1 and top layers from different formulations F1 and F2, respectively, is shown in Figure 3.30. Both the single-layer and multi-layer cells have similar energy densities at low C-rates, with a

slight increase in the specific discharge capacity shown by F1F2. This comparison highlights the impact of the combination of multilayer cells on cell performance. Electrode A_{ML}_F1F1 and Electrode A_{ML}_F1F2 exhibit similar overall behavior, but there is a slight improvement in the specific discharge capacity recorded during formation, preconditioning, and the end of preconditioning, as seen in Tables 3.14. When comparing the capacity after SEI formation, Electrode A_{ML}_F1F1 lost 2.89% (5.28 mAhg⁻¹), while Electrode A_{ML}_F1F2 lost 2.93% (5.46 mAhg⁻¹). This suggests that both Cell A_{SL} and Cell A_{ML} have comparable losses in irreversible capacity due to SEI formation.

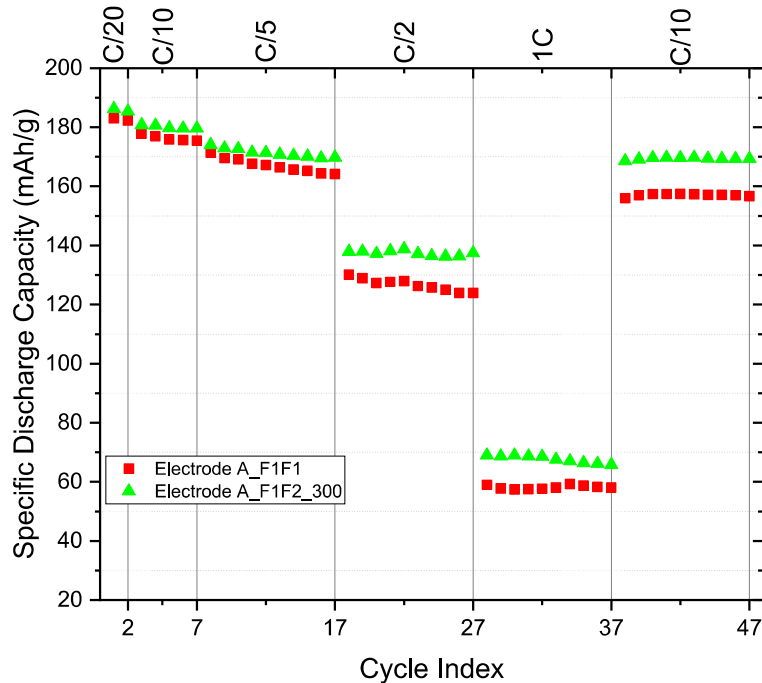


Figure 3.30: Multi-layer Cell A: F1F1 vs. F1F2

Additionally, after the preconditioning phase, Electrode A_{ML}_F1F1 and Electrode A_{ML}_F1F2 experienced a slight reduction in capacity. Electrode A_{ML}_F1F1 lost approximately 1.32%, while Electrode A_{ML}_F1F2 lost approximately 0.63% of its capacity from the start of preconditioning. During the rate capability phase, both electrodes showed a similar increase in specific discharge capacity at low current rates (C/20 to C/5), as indicated in Table 3.14. However, at higher current densities, Electrode A_{ML}_F1F2 had a slightly higher specific discharge capacity, with an average of 7.78% at the C/2 rate and even a more significant difference at the 1C rate. This indicates that while the two electrodes display similar behavior at low current rates, at high current densities, Electrode A_{ML}_F1F2 performs better than Electrode A_{ML}_F1F1 in terms of lithiation. Both cells displayed good recovery during the final C/10 rate cycles following the fast charge at 1C.

Table 3.14: Formation and preconditioning data of ML cells

<i>sample</i>	<i>0.05C start</i>	<i>0.1C start</i>	<i>0.1C end</i>	<i>% difference</i>
<i>Cell/Electrode A_ML_F1F2</i>	186.27	180.81	179.67	0.63
<i>Cell/Electrode A_ML_F1F1</i>	180.15	176.14	173.91	1.32
<i>Improvement [%] of Cell A: ML_F1F2 vs. ML_F1F1</i>	1.73	1.69	2.37	

Table 3.15: Rate capability data of ML cells

<i>sample</i>	<i>0.2C</i>		<i>0.5C</i>		<i>1C</i>		<i>0.1C</i>	
	<i>start</i>	<i>end</i>	<i>S</i>	<i>E</i>	<i>S</i>	<i>E</i>	<i>S</i>	<i>E</i>
<i>Cell/Electrode A_ML_F1F2</i>	174.1	169.9	137.9	137.5	69.0	65.6	168.6	169.4
<i>Cell/Electrode A_ML_F1F1</i>	169.9	165.7	138.8	130.8	62.9	51.6	156.6	160.7
<i>Improvement [%] of Cell A: ML_F1F2 vs. ML_F1F1</i>	1.54	3.39	5.68	9.88	14.64	11.39	7.52	7.49

Table 3.16: Summary of the porosity between two different multilayer samples

<i>Electrode A</i>	<i>Electrode Layers</i>	<i>Porosity [%]</i>	<i>Anode Areal Capacity</i>	<i>Cathode Areal Capacity</i>
			<i>[mA h/cm²]</i>	<i>[mA h/cm²]</i>
<i>F1F1</i>	Multi-layer	55 ± 0.2	9.3 ± 0.1	8.6 ± 0.1
<i>F1F2</i>	Multi-layer	54 ± 0.1	9.5 ± 0.2	8.6 ± 0.1

The difference in performance between Electrode A_ML_F1F1 and Electrode A_ML_F1F2 is particularly noticeable at high current rates, with Electrode A_ML_F1F2 exhibiting a greater energy density. This discrepancy can be attributed to the distinct top-layer composition and resulting microstructure. Despite being made from the same type of graphite (Type A), with an identical BET specific surface area (SSA) and a similar bottom layer formulation and thickness, the F2 formulation's microstructure differed from the F1 formulation due to the change in binder concentration that resulted in a reduction of the active material (graphite) leading to a unique top-layer structure. At high current densities, the difference in cell performance is due to the microstructure of the top layer, which at fast diffusion (at high C-rates) favors lithiation and disregards the effect of the interpenetrating layers since both Electrode A_ML_F1F1 and Electrode A_ML_F1F2 have interpenetrating interfaces and similar loading (Table 3.16). This section implies that the result is inherent and solely reflected by the microstructure of the top layer of the anodes. Therefore, the bilayered anode structure produced from two different formulations is superior in mechanical stability and electrochemical performance compared to the anode produced from the same formulation.

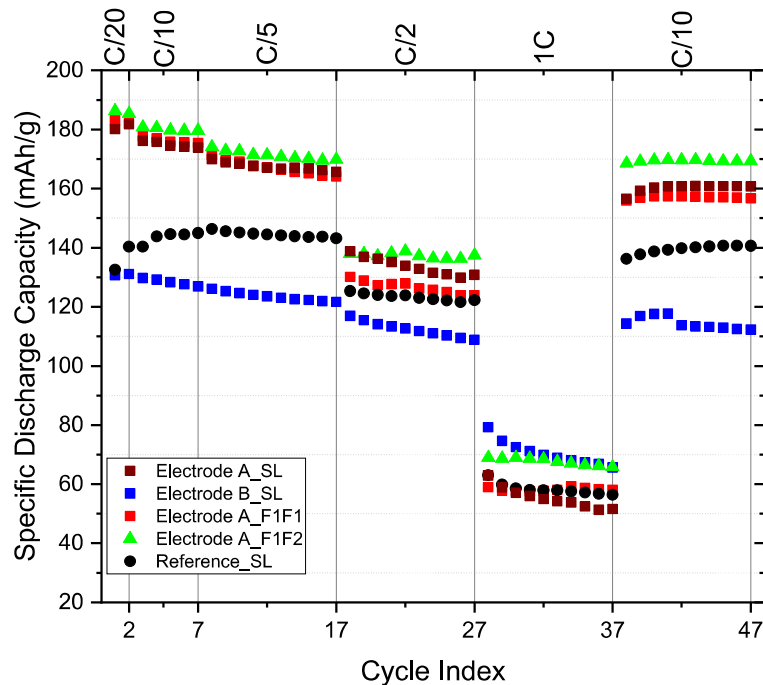


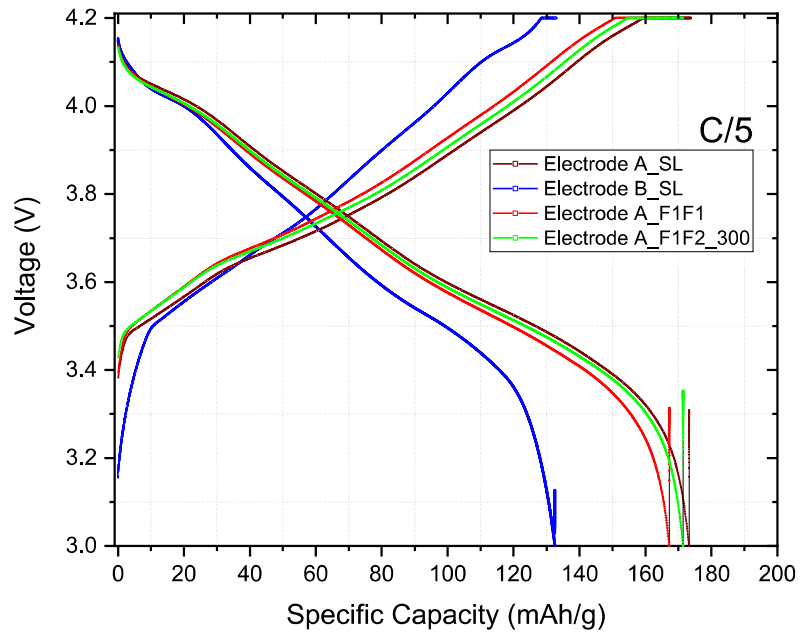
Figure 3.31: Overview of SL and ML cells

To summarize the results of the different anode tests, a general overview is presented in Figure 3.31. Despite initial expectations that Electrode A_{ML}_F1F1 would have a higher loading due to a higher concentration of graphite particles in the F1 formulation, the results showed the opposite. The F2 formulation, with a higher binder content and greater flowability, allowed for greater interpenetration of the slurry into the as-cast rigid layer during top-layer coating, resulting in a similar overall wet gap size. Research studies have shown that having a top layer with a higher porosity than the bottom layer in multilayer electrodes can improve the performance of Lithium-Ion Batteries (LIBs) [1]. Traditionally, this was achieved through different coating techniques or subsequent calendaring-coating steps. However, adjusting the porosity in each layer through the slurry formulation used in this study proves to be a simpler and more efficient solution. It enhances cell performance and saves time and energy by eliminating the need for additional steps. The different porosities are essential in supporting both the wetting of the electrolyte to reach the current collector and the diffusion of lithium ions to regions close to the current collector [3]. This multilayering approach also demonstrates the versatility of optimizing lithium-ion battery electrodes by incorporating different functionalities.

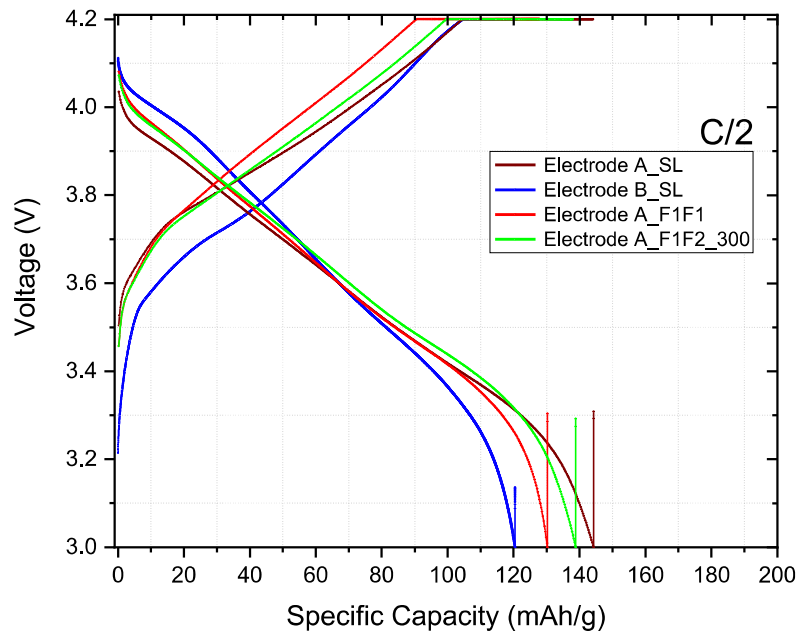
3.4.3.4 VOLTAGE PROFILES OF THE AQUEOUS ANODES

The relationship between voltage and capacity was linear up to a non-linear peak at around 3.54 V (10 mAh/g), followed by a nearly smooth linear relationship until approximately 4.1 V, where a change in specific capacity was observed (in Figure 3.32). During the galvanostatic discharge profile for all samples, lithium-ion intercalation occurred alongside an accompanying side reaction. This occurred at approximately 4.15 V for Electrode A and 4.16 V for Electrode B, with a bumpy relationship between

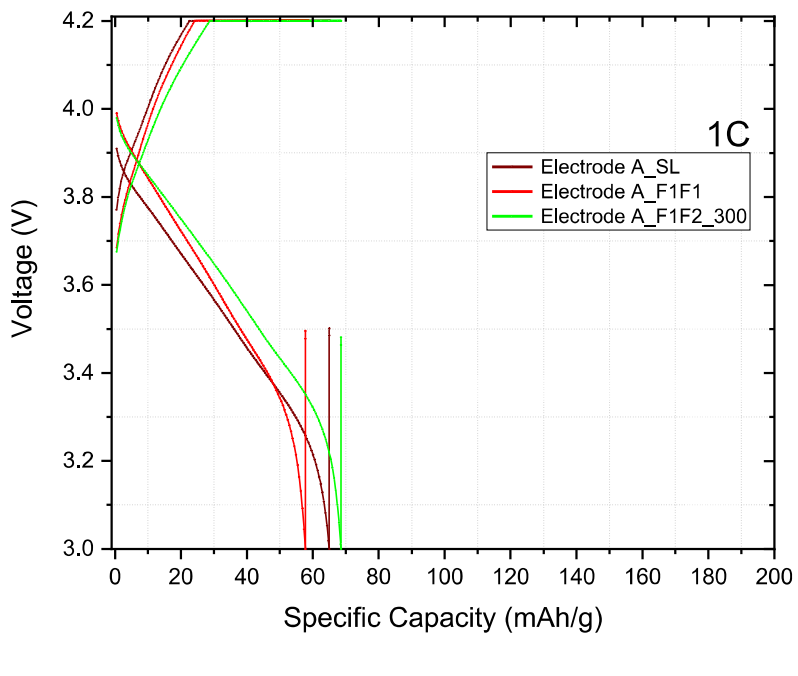
voltage and capacity between 4.15 V and 4.0 V. The relationship became linear and remained so until about 3.54 V (90 mAh/g), where a non-linear relationship was observed until the end voltage of 3 V. As a result, both Electrode A_SL and Electrode B_SL reached 0% state of charge at around 3 volts and 100% state of charge at approximately 4.15 and 4.16 volts, respectively.



a)



b)



c)

Figure 3.32: Voltage profile of aqueous anodes at a) C/5, b) C/2 and c) 1C rates

The higher starting potential values for lithiation in both SL and ML of Electrode A imply that all cells with Electrode A anodes require more energy for removing electrons from its microstructure than Electrode B_SL. This is indicated by the higher discharge and charge profiles of Electrode A_SL in comparison to Electrode B_SL, since a high potential gradient in the porous microstructure could intensify lithium-ion diffusion in the graphite anode [18], [73], [74]. The potential window of both SL and ML of Electrode A_SL is observed to be smaller than that of Electrode B_SL, which suggests that Electrode B can reach lower voltages than Electrode A.

Furthermore, Electrode B has more active sites than Electrode A, suggesting that the electrostatic force holding the lithium-ions in place in Electrode A is stronger than in Electrode B. The electrode material's high BET SSA can significantly boost lithium-ion diffusion kinetics and encourage the intercalation of lithium ions. Meanwhile, the surface's active sites can serve as nucleation sites for lithium-ion intercalation, ultimately leading to improved electrochemical performance. Electrode B's morphology with more active sites allows it to weakly hold the lithium-ions in place after charging. In contrast, lithium-ions can be more easily removed from Electrode B during discharge than Electrode A. Also, in terms of diffusion rates within the anode microstructures, the more active sites in Electrode B facilitate faster diffusion, especially at high current densities; however side reactions can reduce the active sites during longer charge/discharge times and lower the specific discharge capacity.

While the BET SSA is more noticeable when comparing single layers of Electrode A and Electrode B, the presence of the interpenetrating interface is an apparent factor that spawns the need for more energy

for delithiation and a resulting lower specific discharge capacity in multilayers of Electrode A compared to the single layers. Current densities are also an obvious factor influencing the specific discharge capacities of the cells because of the rate of lithium-ion insertion, as shown in Figure 3.32, where the number of lithium-ions that can be reached at a C/5 rate is greater than the number of lithium-ions that can be lithiated/delithiated at the 1C rate. The length of the CV tail at 4.2 V, or potentiostatic step, is another important observation that is influenced by current density. The contribution of the CV step is directly proportional to the resistance inside the electrode during the charge at a constant voltage. The potentiostatic contribution to the specific charge capacity is represented by the plateau at 4.2 V in Figure 3.32. Observing the plots, Electrode A_MLs have less interfacial resistance, explaining their high capacity at low C-rates. The CV shares were smaller in all cells at lower C-rates, such as C/5, compared to C/2 and 1C. However, the hindrance in lithium-ion migration increases with current density, as seen by comparing the CV tails of C/5 and 1C. The hindrances to diffusion within the microstructure of the aqueous electrodes are due solely to C-rates and no side reactions. At C/5 current density, the CV profile is symmetric, and the short CV tail suggests that lithium-ion diffusion is the rate-limiting step for the electrochemical reaction. However, as the current density increases to 1C, the voltage profile becomes more asymmetrical with a pronounced hump, and the longer CV tail indicates that the rate-limiting process for lithium-ion migration is not just diffusion but also includes other processes such as surface reactions or electrolyte depletion, among other possibilities. The observations of the voltage-capacity plots support the performances discussed previously.

CONCLUSION AND OUTLOOK

4. CONCLUSION

Thick anodes for Lithium-ion batteries were developed and characterized, with a focus on the critical role of electrode processing in advancing battery technology. The study found that graphite anodes' structural stability and electrical performance depend on material characteristics, slurry network structure, and fabrication parameters. The study showed that it is possible to manufacture multilayer electrodes with the same active material loading using a tape-casting procedure. The presented manufacturing technique was found to be free from morphological defects. Additionally, all of the electrodes demonstrated enough mechanical integrity to be processed using a standard roll-to-roll system.

The study compared two types of graphite, Type A and B, from different suppliers and found that differences in particle shape affected the rheological behavior of slurries and the electrochemical performance of anodes. Particle shape influenced the flow and viscosity of slurries and the thixotropic and dynamic behavior of the slurries. The slurry containing Type A active material, consisting of uniformly shaped particles and low BET-specific surface area, exhibited characteristics of a viscoelastic liquid with a limited shelf life. On the other hand, the slurry made from Type B active material, composed of irregularly shaped particles and large BET-specific surface area, showed properties of a viscoelastic solid. While single layers were coated by the conventional approach, the multilayer approach enhanced the mechanical integrity of the electrode to the current collector. Electrochemical cycling of both single and multilayers provided insights into cell performance. Graphite structures with lower BET SSA had higher specific discharge capacity at low C-rates than those with larger BET SSA, and significant capacity losses at 1C. Meanwhile, structures with larger BET SSA retained high capacity with minimal losses at a low C-rate but experienced significant losses only at the 1C-rate. Using water as a solvent in aqueous anodes led to better sustainability and higher specific discharge capacity than non-aqueous anodes. The reason for the varying cell performance of the two electrode types produced using water and NMP solvents, respectively, can be attributed to the differences in their resulting microstructure. Furthermore, both single and multilayered anodes of similar formulations showed similar specific discharge capacities. However, multilayered anodes exhibited a more stable discharge capacity due to a more rigid structure that can support repeated cycling. Multilayered aqueous anodes showed enhanced discharge capacity due to a better alignment of channels for lithium-ion diffusion. However, thick electrodes showed limitations on lithium-ion diffusion at high C-rates, leading to losses in discharge capacity that could not be fully compensated by multilayering. This is due to repeated lithiation-delithiation cycles that affect the pore size of the lower layer at the interpenetration interface. F1F2 outperformed in the multilayer category due to the unique microstructure of each layer in the ML structure, highlighting the positive effect of adjusting the coating process on material distribution. This underscores the significant role of the inherent porous

microstructure achieved by formulation optimization in the electrochemical performance of the anodes. Lithium-ion mobility poses the most challenges for thick electrodes to compete at high current densities; however the benefits of multilayering on lithium-ion diffusion can compensate for drawbacks associated with electrode thickness. Long-term cycling tests showed no significant decrease in specific discharge capacity after 47 cycles at C/5 for SL and ML electrodes.

To increase energy density while prioritizing low manufacturing and overall product costs and sustainability, graphite has been identified as a reliable material for producing super-thick anodes with high energy density. By carefully considering the mixing sequence, the challenge of poor dispersion of constituents within the anodes can be resolved, and minimizing the use of binders can prevent binder insulation issues. Additionally, optimization of the process steps and parameters can overcome complexities arising from the interplay between water and increased electrode thickness. In general, good performance at low current densities is advantageous for applications that involve long-term charge and storage, whereas high capacity retention and exceptional performance at high current densities are more useful for short-term charge and storage. Nevertheless, to achieve optimal efficiency of LIBs, it is often necessary to strike a balance among desired properties or requirements.

In summary, this study found that several factors, such as using water as a solvent, ensuring a formulation that meets requirements, optimizing the mixing sequence for homogeneity, pre-analyzing the slurry, and adjusting electrode processing parameters during coating and post-coating processes, as well as taking proper precautions during cell assembly, are crucial for successfully fabricating defect-free thick aqueous anodes.

REFERENCES

- [1] D. Parikh and J. Li, “Bilayer hybrid graphite anodes via freeze tape casting for extreme fast charging applications,” *Carbon N. Y.*, vol. 196, no. May, pp. 525–531, 2022, doi: 10.1016/j.carbon.2022.05.023.
- [2] D. Choi *et al.*, “Li-ion battery technology for grid application,” *J. Power Sources*, vol. 511, no. May, p. 230419, 2021, doi: 10.1016/j.jpowsour.2021.230419.
- [3] D. Müller *et al.*, “Electrochemical characterization of bi-layered graphite anodes combining high and low porosity in lithium-ion cells to improve cell performance,” *Electrochim. Acta*, vol. 391, 2021, doi: 10.1016/j.electacta.2021.138966.
- [4] N. Mahmood, T. Tang, and Y. Hou, “Nanostructured Anode Materials for Lithium Ion Batteries: Progress, Challenge and Perspective,” *Adv. Energy Mater.*, vol. 6, no. 17, pp. 1–22, 2016, doi: 10.1002/aenm.201600374.
- [5] M. Armand *et al.*, “Lithium-ion batteries – Current state of the art and anticipated developments,” *J. Power Sources*, vol. 479, no. June, 2020, doi: 10.1016/j.jpowsour.2020.228708.
- [6] “Custom-Made Battery Pack Design & Battery Contract Manufacturing.” <https://ttekai.com/pages/custom-made-battery-pack-design-and-battery-contract-manufacturing-in-the-usa> (accessed Jan. 24, 2023).
- [7] L. Neidhart, K. Fröhlich, N. Eshraghi, D. Cupid, F. Winter, and M. Jahn, “Aqueous Manufacturing of Defect-Free Thick Multi-Layer NMC811 Electrodes,” *Nanomaterials*, vol. 12, no. 3, pp. 1–15, 2022, doi: 10.3390/nano12030317.
- [8] M. R. Al Hassan, A. Sen, T. Zaman, and M. S. Mostari, “Emergence of graphene as a promising anode material for rechargeable batteries: a review,” *Mater. Today Chem.*, vol. 11, pp. 225–243, 2019, doi: 10.1016/j.mtchem.2018.11.006.
- [9] “Week 1 Understanding Different Battery Chemistry.” <https://skill-lync.com/student-projects/week-1-understanding-different-battery-chemistry-44> (accessed Feb. 01, 2023).
- [10] H. Cheng, J. G. Shapter, Y. Li, and G. Gao, “Recent progress of advanced anode materials of lithium-ion batteries,” *J. Energy Chem.*, vol. 57, pp. 451–468, 2021, doi: 10.1016/j.jec.2020.08.056.
- [11] C. Liu, F. Li, M. Lai-Peng, and H. M. Cheng, “Advanced materials for energy storage,” *Adv. Mater.*, vol. 22, no. 8, pp. 28–62, 2010, doi: 10.1002/adma.200903328.
- [12] W. Sun and Y. Wang, “Graphene-based nanocomposite anodes for lithium-ion batteries,”

Nanoscale, vol. 6, no. 20, pp. 11528–11552, 2014, doi: 10.1039/c4nr02999b.

- [13] K. . Kam and M. . Doeff, “Electrode Materials for Lithium Ion Batteries | Sigma-Aldrich,” *Mater. Matters*, vol. 7, no. 702277, pp. 56–60, 2012, doi: 10.22059/JUFGNSM.2018.01.01.
- [14] H. Zhang, Y. Yang, D. Ren, L. Wang, and X. He, “Graphite as anode materials: Fundamental mechanism, recent progress and advances,” *Energy Storage Mater.*, vol. 36, no. October 2020, pp. 147–170, 2021, doi: 10.1016/j.ensm.2020.12.027.
- [15] J. Li, J. Fleetwood, W. B. Hawley, and W. Kays, “From Materials to Cell: State-of-the-Art and Prospective Technologies for Lithium-Ion Battery Electrode Processing,” *Chem. Rev.*, vol. 122, no. 1, pp. 903–956, 2022, doi: 10.1021/acs.chemrev.1c00565.
- [16] S. H. Sung, D. H. Kim, S. Kim, M. H. Jeong, J. Nam, and K. H. Ahn, “Effect of neutralization of poly(acrylic acid) binder on the dispersion heterogeneity of Li-ion battery electrodes,” *J. Mater. Sci.*, vol. 54, no. 20, pp. 13208–13220, 2019, doi: 10.1007/s10853-019-03846-5.
- [17] B. G. Westphal and A. Kwade, “Critical electrode properties and drying conditions causing component segregation in graphitic anodes for lithium-ion batteries,” *J. Energy Storage*, vol. 18, no. May, pp. 509–517, 2018, doi: 10.1016/j.est.2018.06.009.
- [18] C. Liu and L. Liu, “Optimal Design of Li-Ion Batteries through Multi-Physics Modeling and Multi-Objective Optimization,” *J. Electrochem. Soc.*, vol. 164, no. 11, pp. E3254–E3264, 2017, doi: 10.1149/2.0291711jes.
- [19] M. Schmitt, P. Scharfer, and W. Schabel, “Multilayer slot die coating of Li-ion battery electrodes (Talk)”.
- [20] S. Petrovic, *Battery Technology Crash Course*. 2021. doi: 10.1007/978-3-030-57269-3.
- [21] M. N. Eisler, “Cold War computers, California supercars, and the pursuit of lithium-ion power,” *Phys. Today*, vol. 69, no. 9, pp. 30–36, 2016, doi: 10.1063/PT.3.3296.
- [22] B. Bitsch, J. Dittmann, M. Schmitt, P. Scharfer, W. Schabel, and N. Willenbacher, “A novel slurry concept for the fabrication of lithium-ion battery electrodes with beneficial properties,” *J. Power Sources*, vol. 265, pp. 81–90, 2014, doi: 10.1016/j.jpowsour.2014.04.115.
- [23] C. D. Reynolds, S. D. Hare, P. R. Slater, M. J. H. Simmons, and E. Kendrick, “Rheology and Structure of Lithium-Ion Battery Electrode Slurries,” *Energy Technol.*, vol. 10, no. 10, 2022, doi: 10.1002/ente.202200545.
- [24] T. Kusano, M. Ishii, M. Tani, O. Hiruta, T. Matsunaga, and H. Nakamura, “Rheological behavior of concentrated slurry and wet granules for lithium ion battery electrodes,” *Adv. Powder Technol.*, vol. 31, no. 11, pp. 4491–4499, 2020, doi: 10.1016/j.apt.2020.09.023.

- [25] A. Cushing, T. Zheng, K. Higa, and G. Liu, “Viscosity analysis of battery electrode slurry,” *Polymers (Basel).,*, vol. 13, no. 22, pp. 1–8, 2021, doi: 10.3390/polym13224033.
- [26] K. Kitamura, M. Tanaka, and T. Mori, “Effects of the mixing sequence on the graphite dispersion and resistance of lithium-ion battery anodes,” *J. Colloid Interface Sci.,* vol. 625, pp. 136–144, 2022, doi: 10.1016/j.jcis.2022.06.006.
- [27] H. Hu, B. Tao, Y. He, and S. Zhou, “Effect of conductive carbon black on mechanical properties of aqueous polymer binders for secondary battery electrode,” *Polymers (Basel).,*, vol. 11, no. 9, 2019, doi: 10.3390/polym11091500.
- [28] M. Ishii and H. Nakamura, “Influence of molecular weight and concentration of carboxymethyl cellulose on rheological properties of concentrated anode slurries for lithium-ion batteries,” *JCIS Open,* vol. 6, no. February, p. 100048, 2022, doi: 10.1016/j.jciso.2022.100048.
- [29] J. G. Speight, “Petroleum and Petroleum Products,” *Handb. Pet. Prod. Anal.,* pp. 1–25, 2015, doi: 10.1002/9781118986370.ch1.
- [30] D. Li *et al.*, “Thermal behavior of water base-fluid in the presence of graphene nanosheets and carbon nanotubes: A molecular dynamics simulation,” *Case Stud. Therm. Eng.,* vol. 28, no. November, p. 101669, 2021, doi: 10.1016/j.csite.2021.101669.
- [31] H. O. Pierson, “Handbook of carbon, graphite, diamond, and fullerenes : properties, processing, and applications,” p. 399, 1993.
- [32] V. Berry, “Impermeability of graphene and its applications,” *Carbon N. Y.,* vol. 62, pp. 1–10, 2013, doi: 10.1016/j.carbon.2013.05.052.
- [33] “About Graphite - Graphite Products.” <https://superiorgraphite.com/innovation/about-graphite/> (accessed Feb. 01, 2023).
- [34] Y. Zhang, J. P. Sullivan, and A. Bose, “Rheological and microstructural characterization of aqueous suspensions of carbon black and reduced graphene oxide,” *Colloids Surfaces A Physicochem. Eng. Asp.,* vol. 592, no. November 2019, p. 124591, 2020, doi: 10.1016/j.colsurfa.2020.124591.
- [35] S. Lu and D. D. L. Chung, “Viscoelastic behavior of carbon black and its relationship with the aggregate size,” *Carbon N. Y.,* vol. 60, pp. 346–355, 2013, doi: 10.1016/j.carbon.2013.04.047.
- [36] Y. Hanada, S. Masuda, M. Iijima, and H. Kamiya, “Analysis of dispersion and aggregation behavior of carbon black particles in aqueous suspension by colloid probe AFM method,” *Adv. Powder Technol.,* vol. 24, no. 5, pp. 844–851, 2013, doi: 10.1016/j.apt.2013.02.010.

- [37] “File:Diagram of carbon black structure and texture creation.png - Wikimedia Commons.” https://commons.wikimedia.org/wiki/File:Diagram_of_carbon_black_structure_and_texture_creation.png (accessed Feb. 01, 2023).
- [38] R. Gordon, R. Orias, and N. Willenbacher, “Effect of carboxymethyl cellulose on the flow behavior of lithium-ion battery anode slurries and the electrical as well as mechanical properties of corresponding dry layers,” *J. Mater. Sci.*, vol. 55, no. 33, pp. 15867–15881, 2020, doi: 10.1007/s10853-020-05122-3.
- [39] M. S. Rahman *et al.*, “Recent developments of carboxymethyl cellulose,” *Polymers (Basel)*., vol. 13, no. 8, 2021, doi: 10.3390/polym13081345.
- [40] “Styrene-butadiene - Wikipedia.” <https://en.wikipedia.org/wiki/Styrene-butadiene> (accessed Feb. 01, 2023).
- [41] F. 22). I. W. https://en.wikipedia.org/wiki/Properties_of_water. Properties of water. (2023, “No Title.” https://en.wikipedia.org/wiki/Properties_of_water
- [42] T. Cosgrove, *Colloid Science: Principles, Methods and Applications*. 2009. doi: 10.1002/9781444305395.
- [43] F. Ma, Y. Fu, V. Battaglia, and R. Prasher, “Microrheological modeling of lithium ion battery anode slurry,” *J. Power Sources*, vol. 438, no. July, p. 226994, 2019, doi: 10.1016/j.jpowsour.2019.226994.
- [44] A. Kerimov, G. Mavko, T. Mukerji, J. Dvorkin, and M. A. Al Ibrahim, “The Influence of Convex Particles’ Irregular Shape and Varying Size on Porosity, Permeability, and Elastic Bulk Modulus of Granular Porous Media: Insights From Numerical Simulations,” *J. Geophys. Res. Solid Earth*, vol. 123, no. 12, pp. 10,563-10,582, 2018, doi: 10.1029/2018JB016031.
- [45] D. Liepsch, “A Basic Introduction to Rheology Shear Flow,” *J Biomech*, vol. 35, no. 4, pp. 415–435, 2016, [Online]. Available: <https://cdn.technologynetworks.com/TN/Resources/PDF/WP160620BasicIntroRheology.pdf>
- [46] S. Lowell and J. E. Shields, *Powder Surface Area and Porosity*. Dordrecht: Springer Netherlands, 1991. doi: 10.1007/978-94-015-7955-1.
- [47] M. H. Blees, “Foundations of Colloid Science,” *Colloids Surfaces A Physicochem. Eng. Asp.*, vol. 210, no. 1, p. 125, 2002, doi: 10.1016/s0927-7757(02)00170-x.
- [48] J. S. W. C. Richard Brundle Charles A. Evans and A, *ENCYCLOPEDIA OF MATERIALS CHARACTERIZATION*. 1992.
- [49] Surface Area, “Accelerated Surface Area and Porosimetry System | Aerogels....”

<https://muse.union.edu/aerogels/aerogel-lab-at-union/accelerated-surface-area-and-porosimetry-system/> (accessed Mar. 20, 2023).

- [50] Anton Paar, “BET Theory :: Anton Paar Wiki.” <https://wiki.anton-paar.com/en/bet-theory/> (accessed Mar. 13, 2023).
- [51] D. J. Shaw, *Introduction to Colloid and Surface Chemistry*, Fourth. Butterworth-Heinemann An imprint of Elsevier Science Linacre House, Jordan Hill, Oxford OX2 8DP 200 Wheeler Road, Burlington, MA 01803, 1992.
- [52] A. M. Gaikwad and A. C. Arias, “Understanding the Effects of Electrode Formulation on the Mechanical Strength of Composite Electrodes for Flexible Batteries,” *ACS Appl. Mater. Interfaces*, vol. 9, no. 7, pp. 6390–6400, 2017, doi: 10.1021/acsami.6b14719.
- [53] E-Motec, “An Optimised Method Of Battery Manufacturing | E-Motec.” <https://www.e-motec.net/mixing-of-electrode-slurries> (accessed Mar. 13, 2023).
- [54] J. Zhang and H. Zeng, “Intermolecular and Surface Interactions in Engineering Processes,” *Engineering*, vol. 7, no. 1, pp. 63–83, 2021, doi: 10.1016/j.eng.2020.08.017.
- [55] T. Zemb and P. A. Kralchevsky, “Depletion forces in single phase and multi-phase complex fluids,” *Curr. Opin. Colloid Interface Sci.*, vol. 20, no. 1, pp. 1–2, 2015, doi: 10.1016/j.cocis.2015.02.001.
- [56] W. D. Callister, *Materials science and engineering: an introduction*, EIGHTH EDI. John Wiley & Sons, Inc., 2010.
- [57] S. Lim, S. Kim, K. H. Ahn, and S. J. Lee, “The effect of binders on the rheological properties and the microstructure formation of lithium-ion battery anode slurries,” *J. Power Sources*, vol. 299, pp. 221–230, 2015, doi: 10.1016/j.jpowsour.2015.09.009.
- [58] M. Wang, D. Dang, A. Meyer, R. Arsenault, and Y.-T. Cheng, “Effects of the Mixing Sequence on Making Lithium Ion Battery Electrodes,” *J. Electrochem. Soc.*, vol. 167, no. 10, p. 100518, 2020, doi: 10.1149/1945-7111/ab95c6.
- [59] T. Mezger, *The Rheology Handbook*. 2020. doi: 10.1515/9783748603702.
- [60] M. Jabbari, R. Bulatova, A. I. Y. Tok, C. R. H. Bahl, E. Mitsoulis, and J. H. Hattel, “Ceramic tape casting: A review of current methods and trends with emphasis on rheological behaviour and flow analysis,” *Mater. Sci. Eng. B Solid-State Mater. Adv. Technol.*, vol. 212, pp. 39–61, 2016, doi: 10.1016/j.mseb.2016.07.011.
- [61] “Multilayer Versus Homogenous Baseline Cells – EnPower, Inc.” <https://www.enpowerinc.com/multilayer-versus-homogeneous-baseline-cells/> (accessed Feb.

01, 2023).

- [62] M. Winter, “The solid electrolyte interphase - The most important and the least understood solid electrolyte in rechargeable Li batteries,” *Zeitschrift fur Phys. Chemie*, vol. 223, no. 10–11, pp. 1395–1406, 2009, doi: 10.1524/zpch.2009.6086.
- [63] H. Heimes *et al.*, “Lithium-ion battery cell production process,” no. February, p. ISBN: 978-3-947920-03-7, 2018, [Online]. Available: www.pem.rwth-aachen.de
- [64] D. E. Packham, “Surface energy, surface topography and adhesion,” *Int. J. Adhes. Adhes.*, vol. 23, no. 6, pp. 437–448, 2003, doi: 10.1016/S0143-7496(03)00068-X.
- [65] Allen J. Bard and Larry R. Faulkner, *Electrochemical methods: Fundamentals and applications*, Third edit. Wiley, 2022. doi: 10.1023/A:1021637209564.
- [66] P. S. Analyzers, “Particle size analyzers,” *Met. Powder Rep.*, vol. 51, no. 11, p. 42, 1996, doi: 10.1016/s0026-0657(96)93964-8.
- [67] T. L. for S. P. A. (LabSPA), “Characterization of particle size distribution by laser diffraction according the recommendations of the norm ISO 13320,” no. April, pp. 1–24, 2009.
- [68] P. Properties *et al.*, “WHITEPAPER A basic guide to particle characterization,” 2014.
- [69] J. Gallová, “A . Density determination of liquids by pycnometer B . Density determination of solid matter by pycnometer,” *English*, vol. V, 1999.
- [70] B. Zhao, D. Yin, Y. Gao, and J. Ren, “Concentration dependence of yield stress, thixotropy, and viscoelasticity rheological behavior of lithium-ion battery slurry,” *Ceram. Int.*, vol. 48, no. 13, pp. 19073–19080, 2022, doi: 10.1016/j.ceramint.2022.03.197.
- [71] X. Ma *et al.*, “Exfoliated multi-layered graphene anode with the broadened delithiation voltage plateau below 0.5 V,” *J. Energy Chem.*, vol. 49, pp. 233–242, 2020, doi: 10.1016/j.jecchem.2020.02.044.
- [72] F. Joho, B. Rykart, A. Blome, P. Novák, H. Wilhelm, and M. E. Spahr, “Relation between surface properties, pore structure and first-cycle charge loss of graphite as negative electrode in lithium-ion batteries,” *J. Power Sources*, vol. 97–98, pp. 78–82, 2001, doi: 10.1016/S0378-7753(01)00595-X.
- [73] D. Manka and E. Ivers-Tiffée, “Electro-optical measurements of lithium intercalation/de-intercalation at graphite anode surfaces,” *Electrochim. Acta*, vol. 186, pp. 642–653, 2015, doi: 10.1016/j.electacta.2015.10.072.
- [74] C. Liu, Z. G. Neale, and G. Cao, “Understanding electrochemical potentials of cathode

materials in rechargeable batteries," *Mater. Today*, vol. 19, no. 2, pp. 109–123, 2016, doi: 10.1016/j.mattod.2015.10.009.